3-24-2016

Performance Testing of Various Nozzle Design for Water Electrolysis Thruster

Yuen Liu

Performance Testing of Various Nozzle Designs for Water Electrolysis Thruster

THESIS

Yuen Jing Monica Liu, Second Lieutenant, USAF

AFIT-ENY-MS-16-M-225

DEPARTMENT OF THE AIR FORCE
AIR UNIVERSITY

AIR FORCE INSTITUTE OF TECHNOLOGY

Wright-Patterson Air Force Base, Ohio

AFIT-ENY-MS-16-M-225

PERFORMANCE TESTING OF VARIOUS NOZZLE DESIGNS FOR WATER ELECTROLYSIS THRUSTER

THESIS

Presented to the Faculty

Department of Astronautical Engineering

Graduate School of Engineering and Management

Air Force Institute of Technology

Air University

Air Education and Training Command

in Partial Fulfillment of the Requirements for the

Degree of Master of Science in Astronautical Engineering

Yuen Jing Monica Liu, B.S.A.E.

Second Lieutenant, USAF

March 3, 2016

AFIT-ENY-MS-16-M-225

PERFORMANCE TESTING OF VARIOUS NOZZLE DESIGNS FOR WATER ELECTROLYSIS THRUSTER

THESIS

Yuen Jing Monica Liu, B.S.A.E.
Second Lieutenant, USAF

Committee Membership:

Dr. Carl Hartsfield, PhD
Chair

Dr. David Liu, PhD
Member

Dr. Bill Hargus, PhD
Member

AFIT-ENY-MS-16-M-225

Abstract

The purpose of this research is to develop new nozzles for the HYDROS^{TM} thruster, a pulsed chemical thruster, to improve the current flight performance. This research consists of a base line test of the factory nozzle, as well as testing of three 15-degree conical nozzles with different expansion ratios. Experiments were conducted at plenum pressures 30, 40, and 45 psia to ensure the thruster is throttleable. Impulse bit data was collected through measuring the impulse response of each firing using a torsional balance thrust stand. Analysis of the thruster performance included calculations of impulse bit, specific impulse, thrust coefficient, and exhaust plume attachment. High speed images were taken to evaluate improvements in exhaust plume attachment relative to nozzle contour. Experimental data showed that the smaller expansion ratio nozzles have a higher performance than the larger expansion ratio nozzles. This agrees with previous research from NASA that the benefit from the increase in area ratio does not overcome the increased viscous losses due to the increase in surface area for small throat areas. High speed images showed that the 15-degree conical nozzle design helped improve the original nozzle's flow separation problem. Experimental results were also compared to ideal calculations from chemical equilibrium codes, and previous low Reynolds number nozzle research to evaluate loss in thrust coefficient.

Acknowledgements

I would like to thank my sponsor, Space Vehicles Directorate at Air Force Research Lab, Kirkland AFB, for sponsoring this research. I would like to thank Tethers Unlimited, Inc. for their troubleshooting assistance and for lending me their thrust stand. Without this thrust stand, this research would not have been possible. I also want to thank the technicians at AFIT machine shop for manufacturing the three beautiful nozzles in a timely manner. In addition, I would like to express my gratitude toward my research advisors, Major David Liu and Dr. Carl Hartsfield, for their guidance, energy, and efforts in advising me throughout my research. I would also like to thank my committee member, Dr. Bill Hargus, for his support as well. Most importantly, I would like to thank my mother for working 12 hrs a day everyday, for moving the family across the world, and for given up everything to allow me to follow my dream. She taught me the importance in education and with that, this research and masters degree is for her.

Yuen Jing Monica Liu

Table of Contents

Page

Abstract iv

Acknowledgements v

List of Figures viii

List of Tables xi

Symbol xii

List of Abbreviations xiv

I. Introduction 1

1.1 Background 1
1.2 Motivation 3
1.3 Research Scope 5
1.4 Research Objectives 6
1.5 Assumptions and Limitations 7

II. Literature Review 8

2.1 Chemical Propulsion Systems Size Scaling 8
2.2 Nozzle Design 14
2.3 Low Reynolds Number Nozzle Performance 24
2.4 Water electrolysis systems and process 28
2.5 Hydrogen-Oxygen Combustion 32

III. Test Methodology and Procedures 39

3.1 Introduction 39
3.2 Equipment and Connections 39
3.2.1 Vacuum Chamber 39
3.2.2 Torsional Balance Thrust Stand 41
3.2.3 Thruster 44
3.2.4 Equipment set-up 46
3.3 Calibration of Torsional Balance Thrust Stand 50
3.4 Theoretical Calculations 56
3.5 Nozzle Designs 62
3.6 Error analysis 66

Page

IV. Results and Analysis 68

4.1 Thrust Stand Calibration Results 68
4.2 Performance Analysis 72
4.2.1 Impulse Bit 73
4.2.2 Specific Impulse 77
4.2.3 Thrust Coefficient 88
4.3 Exhaust Plume Attachments 93

V. Conclusions and Future Work 97

5.1 Research Objectives Review 97
5.2 Recommendation and Future work 100
5.2.1 Torsional Balance Thrust Stand 100
5.2.2 The water electrolysis thruster 101

Appendix A. Impulse Bit Data 103

Appendix B. Specific Impulse and Thrust Coefficient Data 108

Appendix C. Mass Per Fire Data 109

Bibliography 111

List of Figures

Figure		Page
1	High speed images of exhaust plume [14].	5
2	Thrust coefficient as a function of pressure ratio, nozzle area ratio, and specific heat ratio [28].	17
3	Exhaust plume pattern for different conditions [20].	18
4	Contour of a conical nozzle [6].	19
5	Nozzle contour of an ideal nozzle [20].	21
6	Nozzle contour of a bell nozzle [6].	22
7	Nozzle contour of a parabolic bell nozzle [6].	23
8	The relationship between nozzle area ratio and thrust coefficient with a divergence angle of 20 degrees [26].	27
9	Schematic Diagram of Electrolysis Cell [27].	29
10	The electrolysis process [27].	30
11	Explosion limits of a stoichiometric hydrogen-oxygen mixture [13]	35
12	Space simulator vacuum system.	40
13	Vacuum to lab connections.	40
14	The window and passthrough location.	41
15	Rotational balance thrust stand with thruster.	42
16	Calibration hammer and motor.	43
17	LDS and micro-adjuster.	44
18	Thruster stand and thruster inside the vacuum chamber.	44
19	The HYDROS^{TM} thruster used for this research.	45
20	The HYDROS^{TM} thruster interface GUI used for this research.	46

Figure Page

21 The lab side set-up. 47

22 The complete experiment set-up. 48

23 Swinging arm with LDS. 49

24 The camera set-up. 50

25 The top view of the thrust stand. 51

26 Hammer impulse response. 52

27 Impulse repsonse with key points. 53

28 The measured response and the new response with the original amplitude. 54

29 An impulse input from the hammer. 55

30 An example of a hammer unit response. 56

31 Loss in thrust coefficient due to viscous effects [26]. 61

32 Thrust coefficient vs. expansion ratio for different Reynolds numbers [26]. 61

33 CAD model of the factory nozzle 62

34 Nozzle contour of the conical nozzle [6]. 63

35 CAD and manufactured model for nozzle 1. 64

36 CAD and manufactured model for nozzle 2. 65

37 CAD and manufactured model for nozzle 3. 65

38 Nozzles comparison of the 4 nozzles [15]. 66

39 The damping ratios of the thrust stand. 69

40 The natural frequencies of the thrust stand. 70

41 Unit impulse responses magnitude of the thrust stand. 70

42 Impulse bit data of the four nozzles. 73

Figure Page

43 Specific impulse data for all four nozzles in various plenum pressures. . . . 78

44 The comparison between the experimental average mass values and the ideal gas law mass values. . . . 81

45 New Isp data with updated mass values. . . . 81

46 Characteristics velocity values in CEA. . . . 84

47 Loss percentage in specific impulse and thrust coefficient based on Spisz *et al.* . . . 85

48 Loss percentage in performance between the expected values and the measured values. . . . 86

49 Overall loss percentage in performance between the ideal values and the measured values. . . . 87

50 The thrust coefficient data of the four nozzles at various plenum pressure. . . . 88

51 The updated thrust coefficient data with mass adjustment. . . . 89

52 Thrust coefficient trend comparison with Spisz *et al.* research data. . . . 92

53 High speed images of factory nozzle: Exposure time of 264 ms (30 fps) [14]. . . . 94

54 High speed images of Nozzle 1: Exposure time of 32 ms (125 fps). . . . 95

55 High speed images of Nozzle 2: Exposure time of 32 ms (125 fps). . . . 96

56 High speed images of Nozzle 3: Exposure time of 4 ms (500 fps). . . . 96

List of Tables

Table		Page
1	Optimal Nozzle Conditions	60
2	Optimal conditions for the three nozzle designs.	66
3	A summary of expansion ratios.	66
4	Test conditions for the HYDROS^{TM} thruster.	72
5	The estimated throat conditions.	75
6	The average mass per fire for various plenum pressures.	79
7	I_{sp} (sec) data comparison between the measured values and the expected values.	83
8	Thrust coefficent comparison between measured and expected thrust coefficient.	90
9	Original Nozzle Raw Data (V)	104
10	Nozzle 1 Raw Data (V)	105
11	Nozzle 2 Raw Data (V)	106
12	Nozzle 3 Raw Data (V)	107
13	I_{sp} data for the four nozzles.	108
14	Mass data for each test set.	110

List of Symbols

C_F	Thrust coefficient
P_c	Chamber pressure
A_t	Throat area
P_o	Stagnation pressure
d_t	Throat diameter
Re	Reynolds number
T	Thrust
ρ	Density
μ	Dynamic viscosity
T_o	Stagnation temperature
Da	Damkoehler number
C_p	Specific heat
P_2	Exit pressure
v_e	Exit velocity
L_n	Nozzle length
r_t	Throat radius
α	Cone half angle
λ	Correction factor
ϵ	Expansion ratio
R_n	Circular contour arc radius
$\dot{m}$	Mass flow rate (kg/s)
I_{sp}	Specific impulse (s)
I_{bit}	Impulse bit (N-s)
A	Amplitude

ξ	Damping ratio
ω_n	Natural frequency (rad)
μ	Dynamic viscosity
M_2	Exit mach number
T_1	Chamber temperature (k)
k	Specific heat ratio
R	Specific gas constant
V_2	Exit velocity (m/s)
SE	Standard error
σ	Error
$\bar{m}$	Average mass per fire
δm	Change of mass per test set
c^*	Characteristics velocity

List of Abbreviations

TUI Tethers Unlimited, Inc.

CDH Command and Data Handling

NASA National Aeronautics and Space Administration

EPS Electrical power subsystem

AFIT Air Force Institute of Technology

MEMS Micro-Electro-Mechanical Systems

MOC Method of characteristics

TIC Truncated ideal contoured nozzle

SPE Solid Polymer Electrolyte

WFB Water feed barrier

LDS Linear displacement sensor

DAQ Data acquisition device

CEA Chemical Equilibrium with Applications

EMI Electromagnetic interference

PERFORMANCE TESTING OF VARIOUS NOZZLE DESIGNS FOR WATER ELECTROLYSIS THRUSTER

I. Introduction

1.1 Background

Space missions are usually driven toward increased capability by more ambitious and diverse objectives. These objectives drive spacecraft design and increase the demand on subsystems, spacecraft size, mass, and complexity of ground control, which ultimately increases the total cost. Funding has become a limitation on some major scientific missions and opportunities for space exploration [2]. For these reasons, over the past several decades, the demand for micro-satellites, such as CubeSats, has increased due to growing interests for high-performance and low-cost satellites. Advances in microelectronics make packaging the minimum functions in a smaller box practical. These growing interests are expressed in the NASA slogan "better, faster, and cheaper". Reduction in life-cycle costs and incorporation of innovative technology have become two of the primary goals for NASA missions [19]. Some advanced space missions require microspacecraft to have a total wet mass as low as a few kilograms [2]. Such missions include precise positioning and spacecraft constellations control for interferometry missions, which aim to detect gravity waves and cosmic-rays, as well as search for planets around distant solar systems [19].

CubeSats are sized in terms of blocks; one block is 1U, nominally a 10 cm x 10 cm x 10 cm cube. CubeSats currently in orbit range from 3U to 12U. The design and volumetric constraints make it difficult to integrate propulsion systems on-board.

Propulsion systems need to work with other subsystems in the CubeSat, such as thermal, electrical power subsystem (EPS), command and data handling (C&DH), and payload. Depending on the propulsion power requirement, solar panel deployment is sometimes needed to accommodation the thruster. Also, depending on the mission and CubeSat systems requirements on-board, sometimes trade-offs between subsystems are necessary to allow CubeSats to function. For example, in order to meet the peak power limit, the payload might need to switch to "off", while the propulsion system is firing. The electromagnetic interference (EMI) from the thruster might also mandate shutting the payload off, regardless of power considerations. Due to these difficulties in design, as well as the severe mass, volume, and power constraints, only a few CubeSats have been launched with a propulsion system [17]. In addition, the selection of suitable propulsion hardware with the right size and mass for small spacecraft is limited.

The HYDROS^{TM} thruster is an electrolysis propulsion system developed by Tethers Unlimited, Inc (TUI). It is specifically designed to fit in a 1U configuration, making it a viable propulsion system for CubeSats. The idea of using liquid water as fuel for spacecraft is not new. It was first developed through Stechman and Campbell in 1973 [27]. However, using the water electrolysis process for micropropulsion is a recent concept. The HYDROS^{TM} thruster, developed by TUI, uses deionized water as a propellant. Through the electrolysis process, the deionized water is electrolyzed to produce hydrogen and oxygen gas. The gaseous hydrogen and oxygen are directed into a gas storage tank before going through the injector and combustion chamber; the mixtures create water vapor through combustion. This propulsion system is throttleable through adjustable tank pressures up to 45 psi. The system requires up to 15 watts of power from the CubeSat EPS. The thruster operates similarly to a payload, receiving data from a ground station to control the C&DH board. The C&DH board

runs the thruster interface board, which sends and receives signals from the thruster. Based on the testing data provided by TUI, hydrogen gas is produced at a rate up to 4 sccm/W from a prototype fuel cell operating up to 88% efficiency. [34]

1.2 Motivation

Successful CubeSat programs can expand opportunities for space exploration. Reduced mass leads to reduced mission costs, allowing more missions to occur. Launch cost, often constituting about 30% of the total mission cost, is largely driven by spacecraft mass. Therefore, reducing mass can help reduce mission cost significantly and a significant part of the remaining costs are driven by the high launch costs [17]. By employing CubeSats to replace big satellites, it could better use the Department of Defense's budget. However, missions for propulsionless CubeSats are limited and are thus far confined to low Earth orbit. Most CubeSats lack a propulsion system—limiting the capability, such as lifetime and maneuvers, and mission profile. By conducting research on CubeSat propulsion, more advanced CubeSat missions are enabled.

Microspacecraft can enable a class of scientific and exploration missions which require many simultaneous measurements displaced in position; as on a planet, a small body, or in a region of space [8]. Micro propulsion systems have been developed to improve CubeSat mission lifetime and increase their controllability over the orbit once deployed. With propulsion systems on board, CubeSats can take on higher level missions and integrate into future constellations. In addition, off-loading scientific instruments from a large, single spacecraft onto a fleet of microspacecraft can reduce mission risk. Losing a few microspacecraft may not jeopardize the entire mission and they are cheap to replace compared to big satellites.

Propulsion systems for CubeSats must be efficient, simple, and scalable, based

on mission requirements. Research on the HYDROS^{TM} thruster is beneficial for CubeSat propulsion development because, unlike many other propulsion systems, this thruster uses a storable, safe, odorless, and non-toxic propellant—water. Fuels such as hydrazine require operators to wear protective suits during handling and use portable propellant service carts to load and unload, which is far from ideal [29]. CubeSats are commonly launched as secondary payloads on carrier rockets and, therefore, the space industry regulates CubeSats to store chemical energy during launch on the order of 100 Watt-Hours and pressure vessels to 1.2 atm to protect the primary payloads from system malfunctions [12]. Protection of the primary payload is one of the limiting factors for propulsion systems in CubeSats. In addition, the HYDROS^{TM} thrusters fuel tank is scalable depending on the mission needs. Conducting research on the HYDROS^{TM} propulsion system can determine the capabilities and Information such as firing rate, specific impulse, and thrust can help determine the amount of delta V this thruster can generate for a given CubeSat mass.

In the Summer of 2014, atmospheric and vacuum testing of the thruster was conducted at the Air Force Institute of Technology (AFIT) to verify system performance. Images, shown in Figure 1, captured from a high-speed camera show the exhaust plume was not attached to the nozzle in the vacuum chamber, thus decreasing efficiency. This research will investigate and attempt to provide a solution to this problem by integrating new nozzle designs. New nozzle development and testing can help provide a better understanding of improvements in thrust and efficiency for the various designs. In addition, most research on nozzle designs have been for fully-developed, steady state flow. Unfortunately, depending on the chamber pressure, size, and pulsed operation, flow in some micro-propulsion systems is not fully developed. This research can bring an understanding to nozzle design and flow attachment for a short (less than 0.5 sec) duration flow. With the completion of this research, future

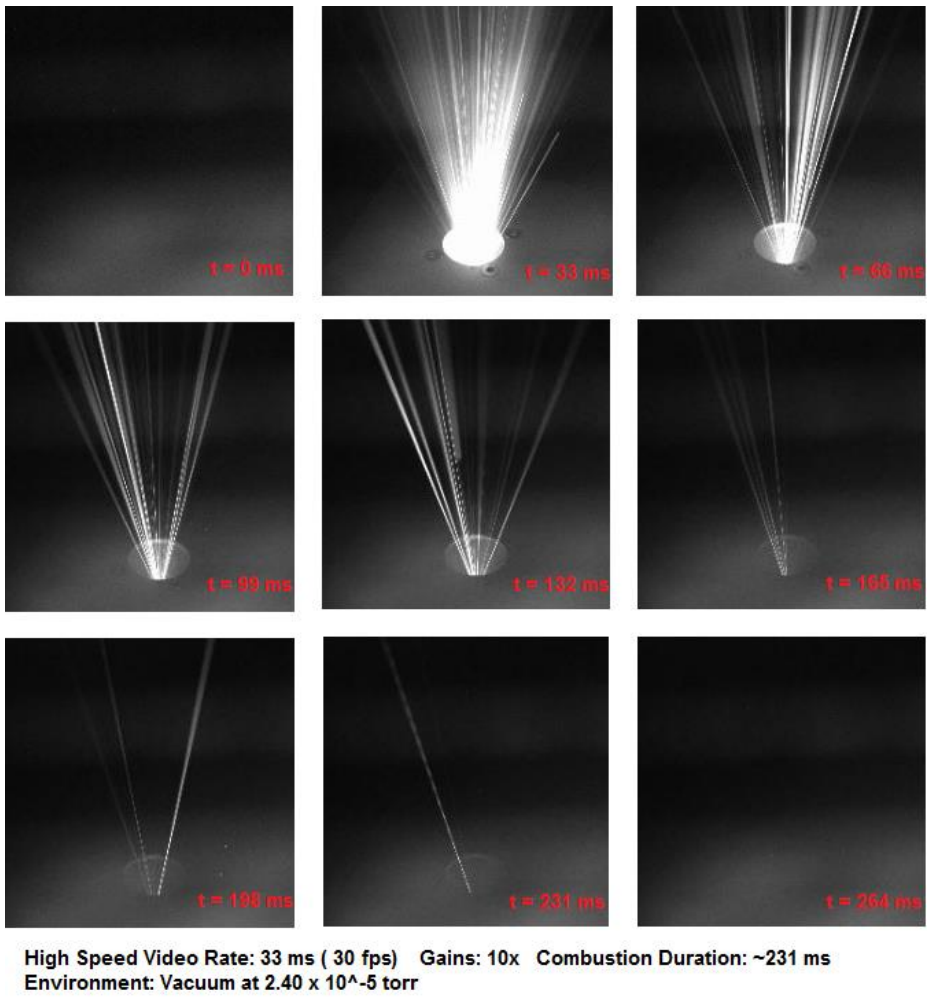

Figure 1. High speed images of exhaust plume [14].

space operators can assess the advantages and disadvantages of various nozzle designs for chemical micro-propulsion and their use on micro-satellites.

1.3 Research Scope

The purpose of this research is to develop new nozzles for the HYDROS^{TM} thruster in order to improve the current performance. This research consists of a baseline test of the factory nozzle, as well as testing three additional nozzles with different characteristics. Experiments are conducted with different plenum pressures to ensure the thruster is throttleable. Thrust data are collected through the impulse bit measure-

ment of each firing using a torsional balance thrust stand. Analysis of the thruster performance includes calculations of impulse bit, specific impulse, and thrust coefficient. A high-speed camera is used to compare the flow attachment for each nozzle. Experimental results of all four nozzles will show how the nozzle length and expansion ratio affect thrust performance for a short-duration flow.

1.4 Research Objectives

CubeSat missions are limited without a propulsion system. By integrating a propulsion system, orbital maneuvers, orbit controls, station keeping, and formation flying are feasible. CubeSats with propulsion systems can help reduce mission costs, which can help the Air Force operate efficiently in a budget-constrained environment. Investigating new nozzle designs can potentially increase the efficiency, the performance of the HYDROS^{TM} thruster, and increase mission capabilities. The goal for this research is to understand how different nozzle contours affect performance and efficiency in small pulsed chemical thrusters.

1. Design nozzles using a nominal two-dimensional conical nozzle geometry to improve the specific impulse of the thruster and verify results by using the experimental impulse bit data to calculate specific impulse.

2. For each nozzle design, experimentally measure performance criteria such as impulse bits, thrust coefficient as a function of the plenum pressure envelope at 30, 40, and 45 psia, in vacuum using a torsional balance thrust stand.

3. Determine nozzle performance in various plenum pressure and expansion ratio by comparing thrust coefficient.

4. Examine viscous effects on nozzles by comparing experimental data with ideal CEA data and previous research data.

5. Determine nozzle efficiency improvement by comparing the exhaust flow attachment points relative to the nozzle using images from a high-speed camera.

1.5 Assumptions and Limitations

This research is set up only to measure the impulse bits of the thruster. Therefore, it is not possible to fully understand the state of the thruster and the combustion process without knowing other properties. This experiment assumes the gaseous hydrogen and oxygen are going through a stoichimetric reaction. The combustion process is best estimated through Chemical Equilibrium with Applications (CEA). It is assumed, based on that simulation, the combustion temperature is approximately 3208 K, and the computer code is a fair presentation of a real-life scenario. Due to the small scale of the thruster, it is also reasonable to assume the flow is operating in a low Reynolds number range, around 1800, which is calculated based on the CEA ideal data. The system probably does not have complete combustion or a fully developed flow due to the small combustion chamber and pulsed operation. Due to time, schedule, and resource constraints, some limitations include the number of nozzles available for testing and experimental measurements. Experimental measurements are limited to impulse bits only with no pressure or temperature data in the combustion chamber because the thruster was designed as an operational thruster and the additional instrumentation was not required.

II. Literature Review

Even though the water electrolysis propulsion system for CubeSats is a fairly new application, numerous research studies related to the different aspects of the system were conducted in the past. Water electrolysis thrusters for rockets were developed and tested as early as 1973. Other institutions have also developed their own version of water electrolysis thrusters. Smaller-scale thrusters are required for CubeSat usage. In order to scale properly, it is important to understand the tradeoff required between size and performance, as well as the effects scaling has on combustion. Several nozzle design methods have been developed for different applications. Nozzle-testing research was conducted to compare the performance between different nozzle shapes and sizes. Smaller-scale thrusters are used and operated in a low Reynolds number range. By looking at different low Reynolds number studies, these studies help understand the properties of the flow, and how low Reynolds numbers may affect performance and efficiency of the system. Lastly, the combustion effectiveness has a direct effect on the thruster performance. An understanding of hydrogen-oxygen combustion may assist with understanding the limitations on the thruster.

2.1 Chemical Propulsion Systems Size Scaling

The goal for scaling is to allow the microthrusters to have the same or similar performance of the full-size model. It is important for the micropropulsion systems to be as efficient as, or even more efficient than, their larger counterparts in order to maximize the limited resources. Scaling the systems down could be accomplished using Micro-Electro-Mechanical Systems (MEMS) technology. For chemical propulsion systems, scaling is based on certain mathematical models. Using Eq. (1), the thrust

equation,

$$T = C_F P_c A_t \tag{1}$$

thrust scales with area, while weight scales with volume. In addition, the scaling laws also hold true for the range of physical effects, such as the impact of viscosity and flow expansion. As size gets smaller, viscosity impacts become larger. A sensible strategy for scaling propulsion systems should not involve simply selecting a thruster and scaling down the geometry before evaluating the loss of performance. Rather, before any modeling begins, the procedures should start by selecting which physical effects, such as viscous effects, momentum, heat transfer, and combustion, are important to keep and which is less important to disregard under the new scale conditions [1].

As propulsion systems shrink, the Reynolds number decreases, leading to less turbulent flow and relatively larger impacts of viscous boundary layers. Nozzle operating characteristics and physical dimensions require scaling in order to obtain the reduced thrust levels and size requirements needed. Thrust is proportional to throat diameter and stagnation pressure shown below [9].

$$T \propto P_o A_t \propto P_o d_t^2 \tag{2}$$

The power of the throat diameter is 2; this finding implies a drastic thrust reduction as the nozzle shrinks. The Reynolds number provides a way to measure nozzle efficiency in term of viscous flow losses. The Reynolds number equation for the throat is given in Eq. (3),

$$Re = \frac{\rho V d_t}{\mu} \propto \frac{P_o d_t}{T_o^x} \tag{3}$$

where x is a positive value ranging between 1.2 and 1.5 depending on the gas[6].

If the thrust level is reduced by a factor of 100 by reducing only the stagnation pressure, then it would also reduce the throat Reynolds number by 100, which would

result in higher viscous losses. In order for viscous losses to remain at a constant level, Reynolds number needs to stay constant as well. This means that if thrust is reduced by a factor of 100, then the throat diameter needs to reduce by a factor of 100 and, at the same time, increase stagnation pressure by the same factor. Thrust is proportional to thrust coefficient, so for a constant thrust coefficient, a factor of 100 in throat radius leads to a factor of 10,000 in throat area and a factor of a 100 increase in chamber pressure, which is impractical.

The operational Reynolds numbers for micronozzles may range from 10^2 to 10^4, which indicate a potential for high viscous and rarefaction losses [9]. Studies have found that for Reynolds numbers below 1,000, relatively thick viscous boundary layers develop, leading to poor nozzle efficiencies. These inefficiencies arise because the flow is not fully expanded in the diverging nozzle section, due to the adverse interaction of the subsonic boundary layer with the core of supersonic flow [25]. As the throat Reynolds number decreases, nozzle efficiencies continue to decrease until they reach a limiting case of free molecule flow. In this case, molecule-surface interactions dominate the flow, and the interactions give a lower bound to the flow through small characteristics dimensions, where the local Knudsen number is near 1 [9]. Apart from looking at low Reynolds numbers, as sizes shrink, fabrication also becomes more difficult. In some cases, surface roughness can reduce efficiencies. There is a lower limit on throat diameter in the neighborhood of 1/16 -1/32 inches driven by manufacturing technique. The throat diameter for this research is approximately 0.05 inches, which is just slightly above this lower limit.

Another issue that needs taken into consideration for scaling is combustion. The mixing length requirement for diffusion flames is critical in combustion for chemical propulsion systems. Mixing length provides a distance required for the fuel and oxidizer to be fully mixed and produce nearly complete combustion. Nearly complete

combustion is important to achieve maximum energy release and has direct effects on system performance. As the thruster chamber becomes smaller, fully mixing the flame becomes more difficult. Thus, efficiency will decrease. Due to scaling, injectors need to operate at low mass flow rates. As the injectors operate with small Reynolds numbers, small Reynolds numbers can cause the discharge coefficient to be too low [17]. Characteristic length of the chamber might need to increase to accommodate the reduced injector efficiencies and the impact of some fluid effects that may not scale well. The characteristic length, L^*, is defined as the length that a chamber of the same volume would have if it were a straight tube and had no converging nozzle section [28].

Injector design requires careful attention. Flow rate control, mixture rate control, and misalignment of impinging propellant jets are all factors that could contribute to poor engine performance and reliability [17]. Unlike-doublet injector types can improve mixing results and help reduce heat load to the injector head by displacing the flame front away from the injector wall surfaces. This displacement distance is unlikely to scale well, and it might require an increase in chamber length. An increased number of injector elements will lead to better mixing results; however, reducing injector size in scaling puts a limitation on the number of injector elements [33]. Depending on the propellant and oxidizer, there are different injector types for gas-gas, gas-liquid, or liquid-liquid. Like-impinging elements are frequently used for liquid-liquid mixing systems, because it avoids most of the reactive-stream demixing of unlike-impinging designs and better maintains combustion stability than unlike patterns [6]. On the other hand, a low Reynolds number also implies less turbulent flow. Turbulent flow is generally more desirable for mixing than laminar flow. Using a premixed flame instead could alleviate some of the problems, however, the premixed propellants could be unstable and require careful handling. Monopropellants or solid

propellants that do not require mixing could also be used to improve the mixing problem [9].

In regard to the chamber, additional combustion issues can arise, when the effects of unburned fuel droplets or soot begin to dominate at small scales. Soot is a hydrocarbon phenomenon, so hydrogen/oxygen reactions are unlikely to have that issue. These effects are caused by inefficiencies in the overall combustion process. According to Bruno, quenching could also occur in a small-scale thruster [1]. As the chamber size shrinks, flame stretch subtracts energy faster and faster, which makes flame quenching possible at small scales. Reforming may help in this regime, as it raises fuel temperatures and accelerates kinetics. Eventually, combustion could become impossible, when the ratio between flamelet thickness and chamber diameter, D, becomes 1. In addition, as chamber size decreases, the ratio of chamber surface area to chamber volume increases, which increases heat loss effects.

The Damkoehler number, Da, provides information on turbulent premixed flames. The equation is shown in Eq. (4),

$$Da = \left(\frac{\ell_o}{\delta_L}\right)\left(\frac{S_L}{\nu'_{rms}}\right) \tag{4}$$

where ℓ_o/δ_L is the length scale ratio and S_L/ν'_{rms} is the reciprocal of a relative turbulence intensity. When Da >>1, the chemical reaction rates are fast in comparison with fluid mixing rates. On the other hand, when Da <<1, the reaction rates are slow in comparsion with mixing rates. Combustion is predicted to occur with either wrinkled laminar flames or flamlets in eddies, depending on the specific operating conditions. These two flames occur when ℓ_o/δ_L is greater than 1 and S_L/ν'_{rms} is less than 1 [30].

However, this is to be taken as the absolute minimum size criterion. At this point, the existence of a flame will be impossible. In addition, as D shrinks, the

flow will eventually become laminar. The flow could be quenched by the wall, if the chamber radius is roughly of the same order as the quenching distance [1]. Quenching distance is the critical diameter of the chamber where a flame extinguishes, rather than propagates [30]. The equation of quenching distance is shown in Eq. (5),

$$d = \frac{2\sqrt{b}\alpha}{S_L} \tag{5}$$

where b is an arbitrary constant greater than 2, α is thermal diffusivity, and S_L is flame speed.

Rocket combustion devices that are regeneratively cooled and or radiation cooled can reach a thermal equilibrium and steady state heat transfer relationship. Scaling can affect the thermal aspect of the system. The heat transfer theory is given in terms of dimensionless parameters, which include Nusselt number, Nu, Reynolds number, Re, and Prandel number, Pr. This equation is shown in Eq. (6) [28],

$$\begin{aligned} \frac{h_g D}{\kappa} &= 0.026 \left(\frac{D\nu\rho}{\mu}\right)^{0.8} \left(\frac{\mu C_p}{\kappa}\right)^{0.4} \\ Nu &= 0.026 Re^{0.8} Pr^{0.4} \end{aligned} \tag{6}$$

where h_g is the film coefficient, D is the diameter of the chamber, ν is the average local gas velocity, κ is the conductivity of the gas, μ is the absolute gas viscosity, C_p is the specific heat of the gas at constant pressure, and ρ is the density of the gas [28]. Eq. (6) indicates that the smaller the flow dimension, the larger the heat transfer coefficient. The amount of heat transfer between the gas and the nozzle walls depends on D and also the operating pressure. Reducing the operating pressure is beneficial, because it reduces the heat transfer to the nozzle walls. However, decreasing pressure leads to a decrease in Reynolds number. A decrease in Reynolds number can adversely affect the nozzle efficiency, due to a relative increase in viscous losses. Attempting to

maintain performance for nozzle expansions could have a significant affect on the heat transfer, because the heat transfer coefficient varies with 1/D at a constant operating temperature [9].

Thermal control is important to a liquid propellant engine to ensure the chamber wall temperature stays within its thermal and structural design limits. Film cooling, or boundary layer cooling, is commonly used for thermal control. Rosenburg demonstrated that, while for more conventionally-sized engines, about 15-30% of the fuel is commonly used for film cooling, these values may reach up to 30-40% for smaller engines in the 22N class, leading to performance losses [24]. This excess fuel is not combusted, results in no energy release, and may decompose endothermically, absorbing energy. It also increases mass flow without increasing thrust significantly.

2.2 Nozzle Design

Nozzle design is a critical component in chemical rocket propulsion systems, because it affects the exit flow profile and thrust. The stagnation pressure, P_o, and temperature, T_o, are generated in the combustion chamber. Nozzles are usually convergent to divergent, or De Laval type. A nozzle uses the pressure and temperature to induce thrust by accelerating the combustion gas from subsonic to supersonic through the exit plane. The main function of a rocket nozzle is to convert the enthalpy of the combustion gases into kinetic energy efficiently and thus create high exhaust velocity gas. The conversion of stored potential energy into available kinetic energy is required in propulsion systems in which a reaction thrust can be obtained. The kinetic energy of ejected matter is the form of energy useful for propulsion. The equations

for enthalpy are shown in Eq. (7),

$$\begin{aligned} h_o &= c_p T + \frac{1}{2} v^2 \\ c_p T_o &= c_p T + \frac{1}{2} v^2 \end{aligned} \tag{7}$$

where $c_p T$ is the potential energy from the perfect gas law, $v^2/2$ is the kinetic energy and T_o is the stagnation temperature. The conversation of energy for isentropic flow between two sections shows that the decrease in enthalpy, or thermal content of the flow, appears as an increase of kinetic energy, since any changes in potential energy may be neglected. [28] As kinetic energy increases, potential energy decreases. This trade in energy is limited by the ratio of P_2/P_o given in Eq. (8)

$$\frac{P_2}{P_o} = \left(\frac{T_2}{T_o} \right)^{\frac{k}{k-1}} \tag{8}$$

The total thrust is equal to the sum of momentum thrust and pressure thrust shown in Eq. (9),

$$T = \dot{m} \nu_e + (P_e - P_a) A_2 \tag{9}$$

where $\dot{m}$ is the mass flow rate in kg/s, ν_e is the exit velocity in m/s, P_e is the exit pressure in Pascal, P_a is the ambient pressure, and A_2 is the cross sectional area of the exit [28]. In space, $P_a = 0$. The equation for ν_e is shown in Eq. (10), where

$$\nu_e = \sqrt{2 \frac{k}{k-1} R T_c \left(1 - \left(\frac{P_e}{P_c} \right)^{\frac{k-1}{k}} \right)} \tag{10}$$

k is the specific heat ratio of the fluid, T_c is chamber temperature in Kelvin, P_c chamber pressure in Pa, and R is the specific gas constant, which is the universal gas constant divided by the mean molecular weight of the product mixture. Eq. (10) does not provide any information on the thrust, based on the specific design of the

thruster, but it is related to I_{sp}.

To further expand Eq. (9), the thrust equation may be described as a function of chamber pressure and expansion ratio, ϵ, which is the ratio between exit area and throat area. The derivations are the following and Eq. (11) is the final ideal rocket thrust equation, where the thrust is proportional to the chamber pressure, throat area, and expansion ratio.

$$\begin{aligned} F &= \dot{m}\nu_e + \frac{P_c A_t}{P_c A_t}\left(P_e - P_a\right) A_2 \\ &= \dot{m}\nu_e + P_c A_t \left(\frac{P_e}{P_c} - \frac{P_a}{P_c}\right)\frac{A_2}{A_t} \\ &= \frac{A_t \nu_t \nu_e}{V_t} + P_c A_t \left(\frac{P_e}{P_c} - \frac{P_a}{P_c}\right)\frac{A_2}{A_t} \end{aligned}$$

$$= A_t P_c \sqrt{\frac{2k^2}{k-1}\left(\frac{2}{k+1}\right)^{\frac{k+1}{k-1}}\left[1 - \frac{P_e}{P_c}^{\frac{k-1}{k}}\right]} + P_c A_t \left(\frac{P_e}{P_c} - \frac{P_a}{P_c}\right)\frac{A_2}{A_t} \qquad (11)$$

This equation applies for an ideal rocket with a constant specific heat ratio throughout the expansion process. Using this equation, one can obtain the thrust coefficient, C_F. Thrust coefficient showed in Eq. (12) is a key parameter to analyze, and it is independent of chamber pressure.

$$C_F = \frac{F}{P_c A_t}$$

$$C_F = \sqrt{\frac{2k^2}{k-1}\left(\frac{2}{k+1}\right)^{\frac{k+1}{k-1}}\left[1 - \frac{P_e}{P_c}^{\frac{k-1}{k}}\right]} + \left(\frac{P_e}{P_c} - \frac{P_a}{P_c}\right)\frac{A_2}{A_t} \qquad (12)$$

For a fixed pressure ratio, P_c/P_a, an ideally expanded nozzle, with P_e=P_a, yields the peak values for thrust coefficient and thrust for a fixed ambient pressure condition. Reducing the ambient pressure will increase thrust coefficient and thrust. As the ambient pressure drops, the thrust will further improve, but P_e will be fixed by the expansion ratio of the nozzle. In addition, maximizing the momentum thrust

component gives the most performance that can be extracted for a fixed ambient pressure. A bigger nozzle could help lower P_e and T_e, turning more potential energy into kinetic energy for the momentum thrust. This peak value is known as the ideally expanded thrust coefficient, and it is an important criterion in nozzle design considerations [33] [30]. Figure 2 shows the coefficient of thrust as a function of pressure ratio, expansion ratio, and specific heat ratio for the optimum expansion conditions, $P_e = P_a$. This optimum coefficient is changeable with designs by changing different pressure ratios P_2/P_1, values of specific heat ratio, and expansion ratio.

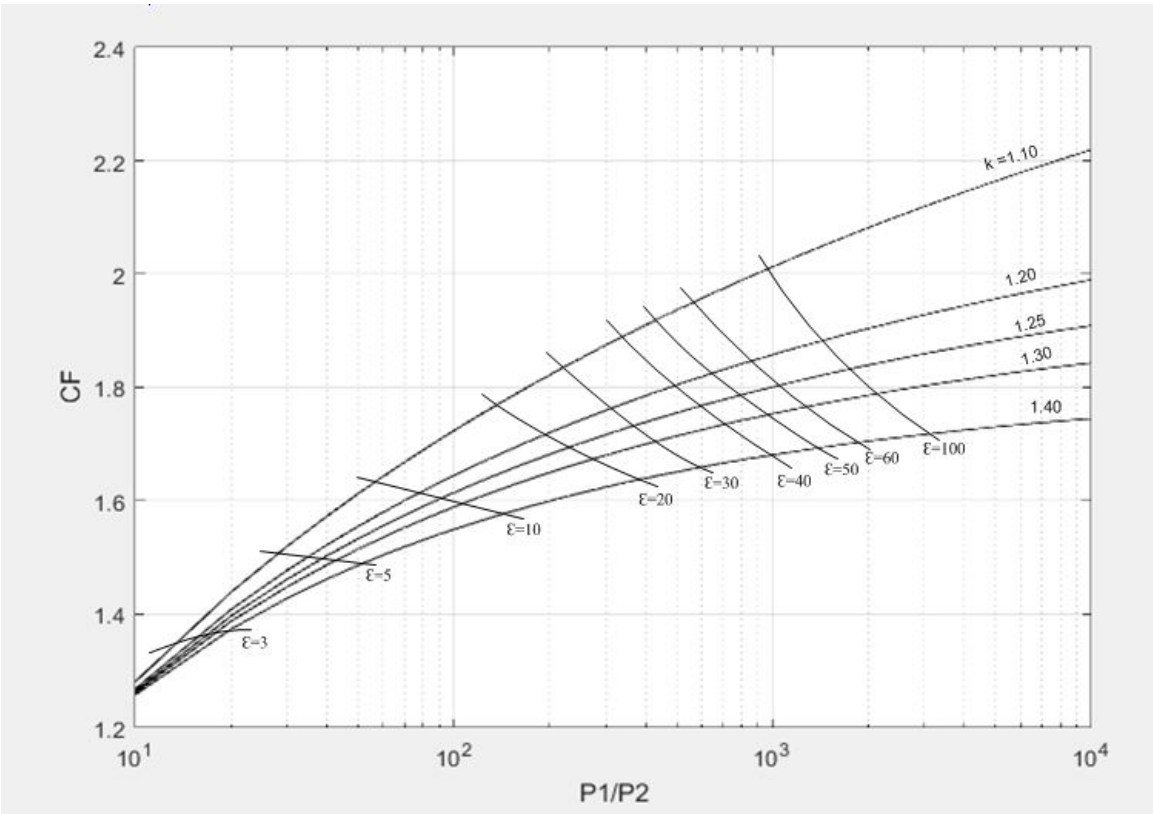

Figure 2. Thrust coefficient as a function of pressure ratio, nozzle area ratio, and specific heat ratio [28].

Exit flow condition is categorized into underexpanded, fully-expanded, and overexpanded based on the nozzle design. Designing a nozzle that is close to fully-expanded is possible, but a fully expanded nozzle is an ideal case that does not account for losses

due to friction, divergence, shocks, and internal expansion waves. The three conditions are shown below in Figure 3. Underexpanded flow occurs when the atmosphere

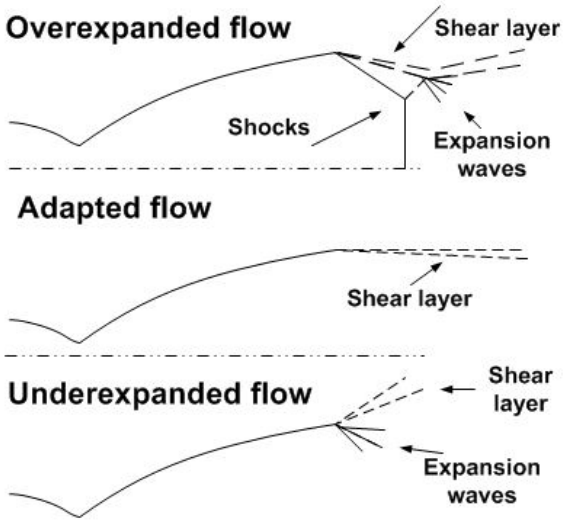

Figure 3. Exhaust plume pattern for different conditions [20].

pressure is less than the exit pressure, due to a smaller exit area. Gas expansion is incomplete inside the nozzle; therefore, expansion takes place outside the nozzle exit and causes external expansion waves to form at the exit. The thrust coefficient value would be less than the optimum expansion value for the fixed ambient pressure condition. On the other hand, overexpanded flow occurs when the atmospheric pressure is greater than the exit pressure, due to a larger-than-optimal exit area. For an overexpanded flow, jet separation and internal oblique shocks inside the nozzle may occur [28].

Different nozzle contour design methods are available to target the fully-developed flow condition. One of the most basic demands for nozzle design is to minimize the weight. As nozzle weight increases, it becomes more difficult to fabricate and handle. The main goal in nozzle design is to minimize the nozzle length and surface area, while optimally contouring the nozzle to achieve maximum efficiency. For a given expansion ratio, the design considerations and goals for an optimum nozzle-

shape selection are the following: Uniform, parallel, axial gas flow at the nozzle exit for maximum axial momentum; minimum separation and turbulence losses within nozzle; shortest possible nozzle length for minimum space envelope, weight, wall friction losses, and cooling requirements; ease of manufacturing [6].

Historically, a conical nozzle is one of the most commonly-used nozzles, due to its simple and easy-to-fabricate design. The conical nozzle allows the flexibility to increase or decrease the expansion ratio without major re-design. The conical nozzle contour is shown in Figure 34. The nozzle throat section has a circular arc contour, R,

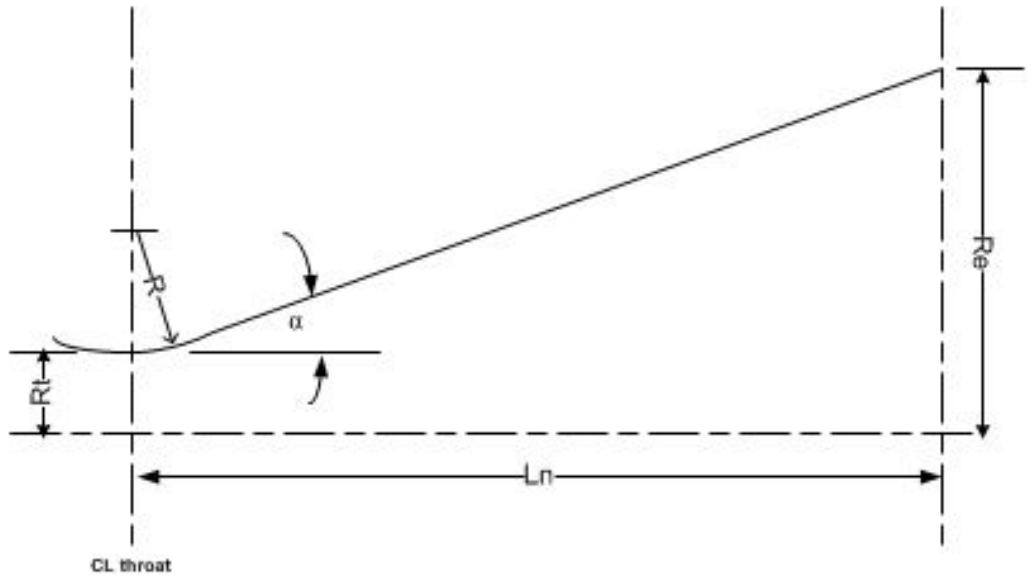

Figure 4. Contour of a conical nozzle [6].

which is typically 0.5 to 1.5 times the throat radius, R_t. The nozzle cone half angle, α, varies from 12 to 18 degree. A 15-degrees half angle is the norm, and it is often used as a reference in comparing performance, weight, and length with other types of nozzles. Spisz *et al.* research indicated that the thrust coefficient is not greatly affected by changes in the divergence angle for 15 to 25 degree [26].

The length of the nozzle is calculated using Eq. (13).

$$L_n = \frac{r_t(\sqrt{\varepsilon} - 1 + R_n(sec(\alpha - 1)}{tan(\alpha)} \tag{13}$$

Due to the nonaxial component of the exhaust gas velocity, performance losses occur in the conical nozzle design. A correction factor, λ, is used to calculate the exit flow momentum, shown in Eq. (14).

$$\lambda = \frac{1 + cos(\alpha)}{2} \tag{14}$$

This factor, also known as the geometrical efficiency, is the exit flow momentum ratio between the conical nozzle and the ideal nozzle with uniform, parallel, and axial flow. Theoretically, using Eq. (12), the vacuum thrust coefficient of a conical nozzle with a 15-degree half angle will be 98.3 % of the ideal thrust coefficient [6].

Apart from the conical nozzle, another nozzle design is an ideal or isentopic bell nozzle. This nozzle produces isentropic flow without internal shocks, and it provides a uniform exit velocity. This nozzle is designed by using the method of characteristics (MOC). The basic flow structure is shown in Figure 5. For this design, point T to N is the initial expansion, and the contour NE turns the flow in the axial direction. TN also defines the Mach number at K, which is equal to the Mach number at the exit E. An ideal nozzle is not suitable for rocket applications, because it is too long, and it is difficult to construct the NE streamline for a perfect uniform flow. An ideal nozzle requires a large length to produce a one-dimensional exhaust profile [20].

Truncated ideal contoured nozzle (TIC) is an improved version of the ideal nozzle, because it neglects the last part of the ideal nozzle contour due to the small wall slope. As long as only the contour is truncated, and not the kernel, then the TIC nozzle will have a central part, where the velocity profile is parallel and uniform. Only the

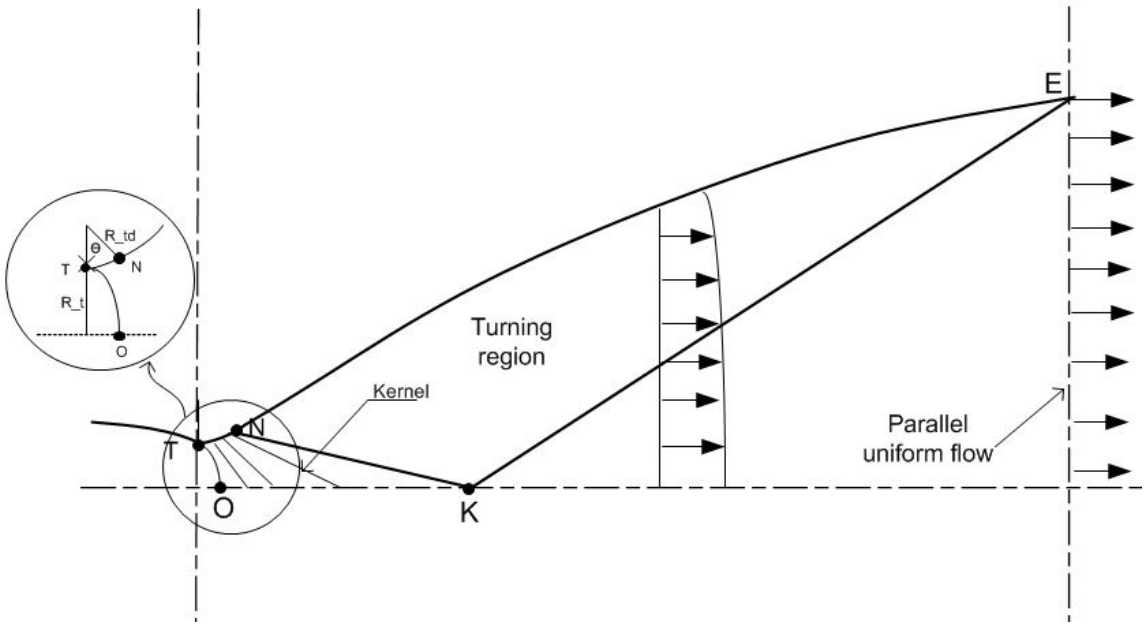

Figure 5. Nozzle contour of an ideal nozzle [20].

region closest to the wall is divergent.

Another method to optimize the nozzle contour is known as the bell nozzle, also referred to as the Rao-Shmyglevsky nozzle. Rao created the method for optimizing the nozzle to a specified length in order to maximize the thrust. The method of constructing an optimum nozzle contour is to first choose a suitable curve for the nozzle wall contour in the throat section. The circular arc r_{td} should be 1.5 times the throat radius. The nozzle wall contour of the throat region is calculated using the calculus of variations. According to Rao, the ambient pressure, length of the nozzle, and wall contour in the throat region appear as governing conditions in the formulation and solution of the optimum thrust problem [23]. The contour of a bell nozzle is shown in Figure 6.

The wall contour is gradually changed to eliminate oblique shocks. The contour of NE is controlled by the expansion ratio and nozzle length. The characteristics line, NK, is constructed by satisfying the following conditions concurrently:

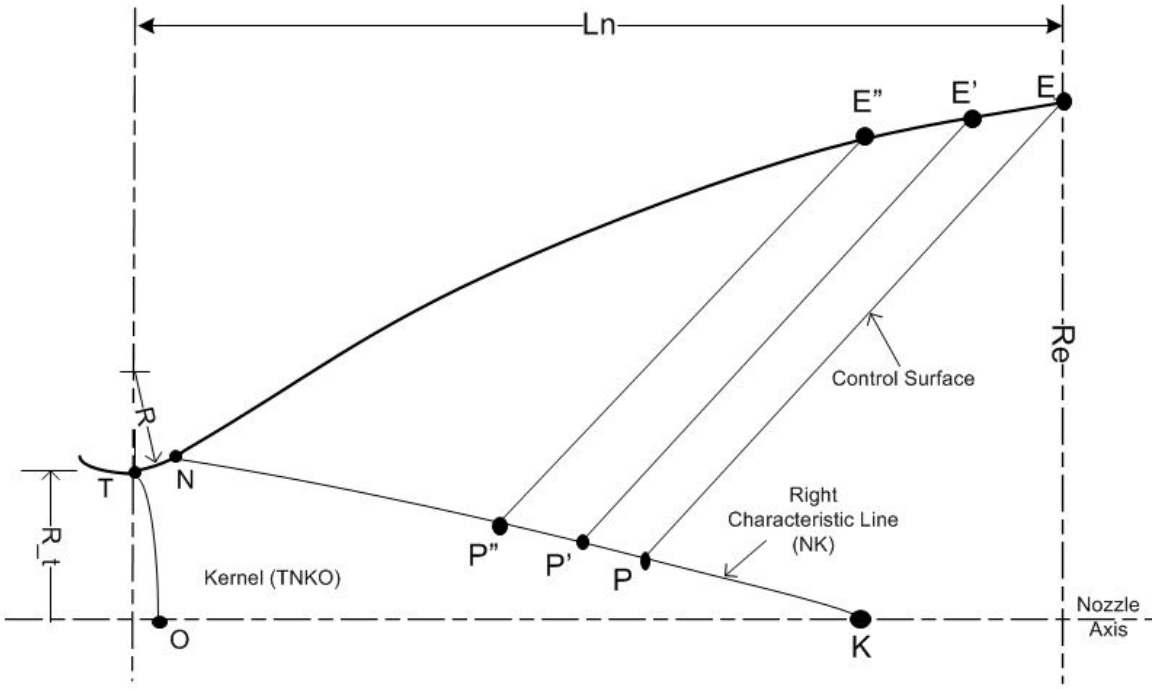

Figure 6. Nozzle contour of a bell nozzle [6].

1. A control surface PE can be generated between the point E and a selected point P along the line NK.

2. Mass flow across PE equals the mass flow across NP.

3. Maximum thrust by the nozzle is attained. [6]

It is necessary to select the point P', P", and P, because the control surfaces P'E', P"E", PE can be generated to define E', E", and E. A 15-degree half-angle conical nozzle is the standard practice used to define bell nozzle. Typically, an 80% bell nozzle is the standard design, which is defined as 80% of the conical nozzle distance between the throat and the exit plane with the same expansion ratio. Based on Huzel and Huang, bell nozzle C_F has approximately a 2% increase compared to conical nozzles. Different expansion ratios for a bell nozzle yield similar C_F for nozzle lengths between 85%-100 %. Overall, length beyond 80% does not have a significant contribution

toward performance, but it adds additional weight [6] [20].

The calculation used for the bell nozzle is complicated. However, using the parabolic geometry approximation of the bell nozzle, created by Rao shown in Eq. 15, provides a more convenient way to design the near-optimum thrust nozzle contour.

$$\left(\frac{r}{r_t} + b\frac{x}{r_t}\right)^2 + c\frac{x}{r_t} + d\frac{x}{r_t} + e = 0 \tag{15}$$

Using this approximation, the geometry of the nozzle shown in Figure 7 is completely defined by the five variables r_t, θ_N, L, r_E, and θ_E. θ_N is the initial wall angle of the parabola and θ_E is the nozzle exit wall angle. Both angles are functions of the expansion ratio.

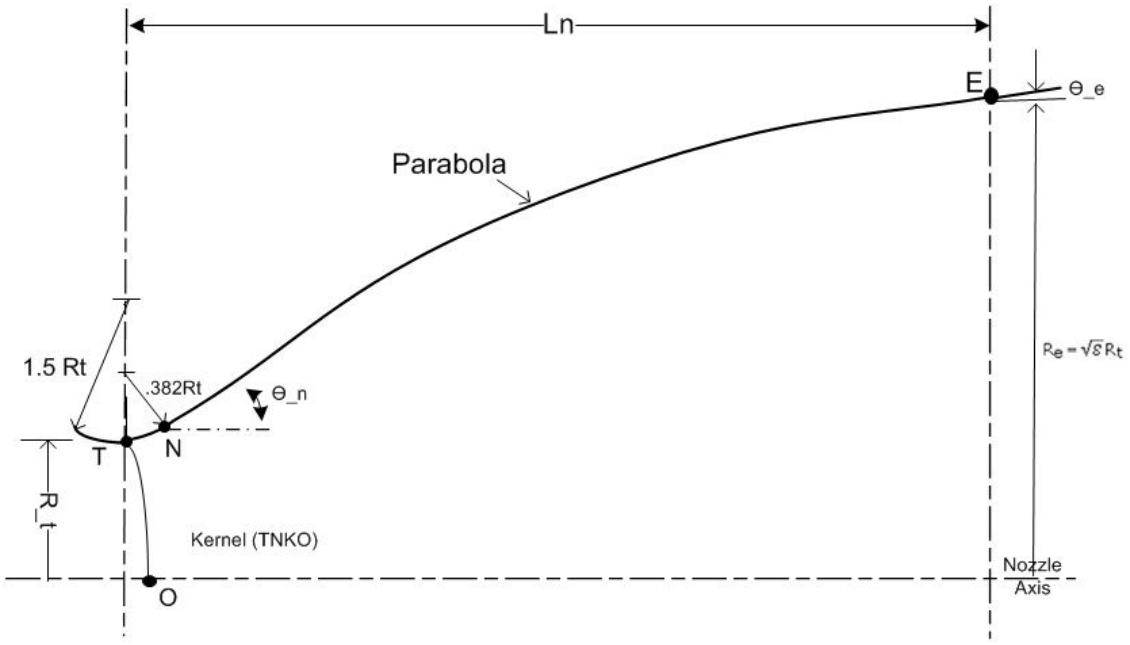

Figure 7. Nozzle contour of a parabolic bell nozzle [6].

Ostlund conducted a study of both bell and parabolic bell nozzles. One main difference is the location of the internal shock generated by the discontinuity in contour curvature. In a bell nozzle, this shock was formed downstream of the last running characteristic line and, therefore, has no wall pressure influence. However, in

a parabolic bell nozzle, this shock formed upstream of the characteristic line, and it affects the flow properties at the wall. This caused a slightly-higher exit wall pressure. For this reason, the parabolic nozzle has proven useful for sea-level nozzles, where the flow separation margin improvement is important [6] [20].

2.3 Low Reynolds Number Nozzle Performance

In the low Reynolds number region, a large portion of the flow area is occupied by the flow boundary layer. The relative increase of viscous losses can reduce thruster performance. Rothe performed electron-beam studies of low Reynolds number flows between 100 and 1500 in 1970. The studies were conducted using a conical nozzle with a 20-degree wall angle. The results of his studies indicated that for Reynolds number greater than 500, a small inviscid core existed in the flow. As the Reynolds number increased close to 1,000, the core extended to the nozzle exit. With lower Reynolds numbers, axial density and pressure gradients became less steep. Also, for Reynolds number ranges from 500-1000, the centerline temperatures decrease monotonically from the throat to the exit. In addition, his studies determined for Reynolds numbers below 300, the flow is fully viscous with no indication of any inviscid core. Overall, Rothe found significant negative radial pressure gradients exit throughout the nozzle for Reynolds numbers ranging from 100-1500 [25].

Murch and Broadwell also conducted performance studies with heated nitrogen and hydrogen on low thrust and low Reynolds number nozzles to determine the dependence of thruster performance on nozzle geometry. These studies were conducted using 10- , 20- , and 30- degree conical nozzles, bell nozzles, and horn nozzles. The results of the studies indicated nozzle efficiencies for different area ratios dropped from 94% to 90% as Reynolds numbers decreased from 2900 to 600. The nozzle efficiency in this case defined as the ratio of the actual specific impulse to the specific impulse

of a frictionless nozzle with the same area ratio. The efficiencies also decreased with an increase in area ratio. Studies also indicated for lower Reynolds numbers, an increase in area ratio may not produce an increase in specific impulse. In performance comparison between different half angles, the 20 degree nozzle produced the highest efficiency, while the 35-degree nozzles were the poorest due to divergence losses [18].

Grisnik and Smith performed experimental studies on high-performance electrothermal thrusters operating in a low Reynolds number region [4]. These studies were conducted using a conical, bell, trumpet, and modified trumpet nozzle. Similar to previous low Reynolds number studies, the nozzles indicated significant decreases in specific impulse efficiency with decreasing Reynolds numbers. These studies of the four nozzles also concluded that changes in the divergent contour do not affect the viscous and divergent losses to any appreciable extent. All four nozzles were filled with a large boundary layer. [4] Shorter expansion lengths were advantageous at very low Reynolds numbers for improving performance and reducing thruster size and weight. The flow through a shorter nozzle exhibits a thinner boundary layer near the nozzle exit [9].

Regarding nozzle geometry, Hopkins and Hill developed a method to numerically predict the flow field in the transonic region of nozzles [5]. Their studies indicated the most significant geometric factor influencing the transonic flow pattern is the wall radius of curvature in the throat region. The curvature of the throat significantly altered the shape of the sonic line. When the radius of curvature was less than the throat radius, an inflection point occurred in the sonic line. The effect of convergent angle had on the throat flow was insignificant unless the wall radius of curvature was less than the throat radius [5]. Moreover, other low Reynolds number flow studies included considering the discharge coefficient. Kuluva and Hosack examined the discharge coefficient of micro-thruster propulsion nozzles at low Reynolds numbers. The

results showed that the effect of velocity slip on the discharge coefficient is significant at throat Reynolds numbers less than about 10^3. The effect of curvature becomes important at Reynolds numbers on the order of 2 x 10^2 [11].

In 1987, Whalen conducted an experimental performance study on low Reynolds number flows of 15- , 20- , and 25- degree conical nozzles, bell nozzles, and trumpet nozzles with unheated nitrogen and hydrogen. The main goal of this study was to evaluate and compare the performance of different nozzle contours. Specific impulse efficiency and discharge coefficients for each nozzle as a function of Reynolds numbers were evaluated for different area ratios and nozzle contours [32].

The results indicated at Reynolds numbers below approximately 2000, bell contour nozzles tended to have a lower efficiency than the other contours. The trumpet and 25- degree conical nozzles performed slightly better than the other nozzles. For high-area ratios, the trumpet and 25- degree conical nozzles performed significantly better than the bell nozzles. Therefore, the bell nozzles, as designed, were not recommended for low Reynolds number nozzles. For small nozzles, performance differences between different contours were small. If this small difference was the not the major driver for the thrusters application, then it is better to design nozzles based on the ease of fabrication [32].

Spisz *et al.* conducted studies regarding the performance losses associated with low Reynolds numbers, low flow rates, and low thrust nozzles [26]. The results indicated at low Reynolds numbers, the thrust coefficients were lower than the thrust coefficient calculated for isentropic flow through a choked orifice. In addition, even though large-area ratio usually helped increase performance, in the case of low Reynolds numbers, large area ratios were not required for achieving maximum thrust [26]. Figure (32) is a recreated figure of Spisz's studies data and the figure illustrates effects area ratio had on thrust coefficient for different Reynolds numbers. For Reynolds number equal

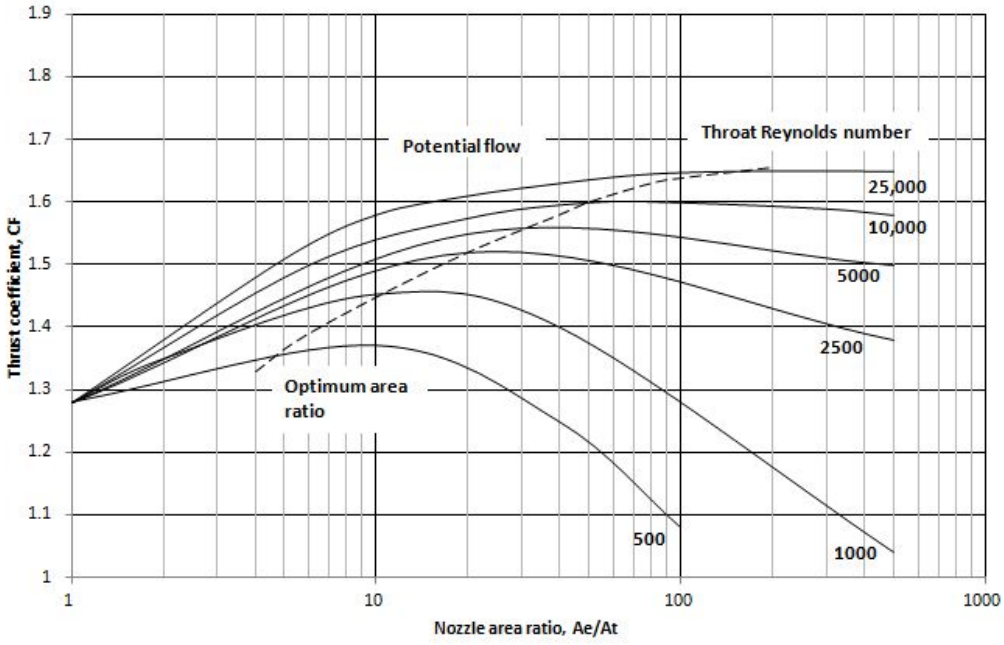

Figure 8. The relationship between nozzle area ratio and thrust coefficient with a divergence angle of 20 degrees [26].

to 500, the optimum-area ratio for the maximum thrust coefficient is approximately 10. This figure shows that for Reynolds numbers lower than 1,000, a large increase in area ratio can produce up to a 28% reduction in thrust coefficient. As Reynolds number decreases, viscous effects become stronger, the increase in area ratio might not overcome the increase in viscous effects caused by the added surface area.

For such small, low-thrust nozzles, the boundary layer could cover a substantial portion of the available nozzle area. The boundary layer introduces viscous losses and alters the free-stream conditions so that the conventional assumption of a one-dimensional isentropic expansion process becomes questionable. For low mass flow rates, heat-transfer losses to the nozzle walls can be a significant portion of the total thermal energy available for kinetic energy conversion [26]. Therefore, the process is not isentropic, because it is not adiabatic due to heat transfer and it is not reversible due to friction.

2.4 Water electrolysis systems and process

The water electrolysis system uses deionized water as fuel in a low-pressure tank. A membrane feeds the water to an electrolyzer. Through the electrolysis process, the water absorbs the electrical energy and decomposes into gaseous hydrogen and oxygen by ion exchange. Hydrogen and oxygen gases will go into separate tanks before entering the injector for combustion [27].

Currently, no water electrolysis system in a CubeSat has flown in space yet, but the concept and design of a water electrolyzer is not a new development. In 1973, the initial water electrolysis system test and studies were first introduced by Stechman, *et al.* They conducted the study by using two different engines: one produced 22 N of thrust and the second one, which was a scaled-down version of the first one, produced 0.445 N of thrust. Electrical current passed through a plastic membrane that was saturated with water to create ion exchange. The ion exchange membrane performed as a Solid Polymer Electrolyte (SPE) without requiring another electrolytic agent such as acid or alkaline fluids. A SPE was in charge of the conduction of protons, electrical insulation, and product gases separation. The electrolysis system consisted of a cathode, an anode, a water feed barrier, and a SPE. A drawing of this system is shown in Figure 9, and the electrolysis process is shown in Figure 10 [27].

The deionized water first entered through a water feed barrier (WFB). This WFB acted like the SPE with the exception that it was without electric current. The reactant water first passed through the WFB to enter the cathode side of the wall. The water diffused across the SPE to the anode side for the electrolysis process. The cathode and anode created a gradient across the SPE. This gradient increased the electrical resistance in SPE and lowered the water activity at the anode. At the anode, the first electrolysis process occurred with a chemical reaction shown in Eq.

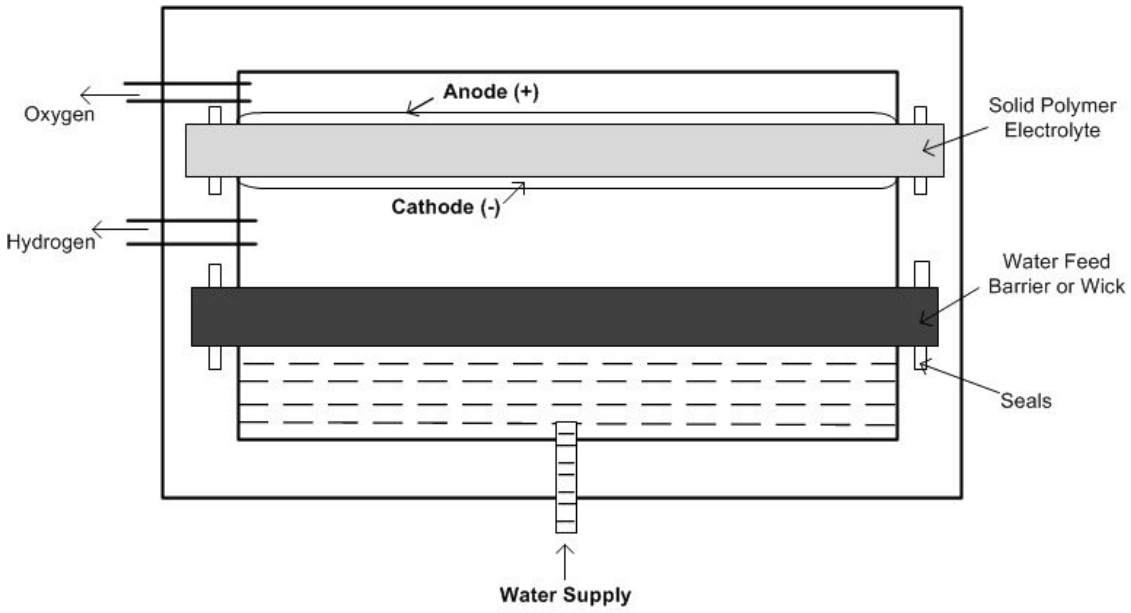

Figure 9. Schematic Diagram of Electrolysis Cell [27].

(16), and released gaseous oxygen.

$$2H_2O \rightarrow 4H^+ + 4e^+ + O_2(g) \tag{16}$$

A manifold adjoining the anode side was connected to an oxygen plenum tank, where the released oxygen gas would transfer. The SPE was created such that only the passage of protons is allowed to go through, but the passage of hydrogen or oxygen gas was prohibited. The SPE allowed the separation of gases to occur. After the gaseous oxygen was released, $4H^+$, hydrogen traveled back to the cathode side, where the second electrolysis process occured with the chemical reaction described by Eq. (17), which releases hydrogen gas.

$$4H^+ + 4e \rightarrow H_2(g) \tag{17}$$

A manifold adjoining the cathode side was connected to a hydrogen plenum tank,

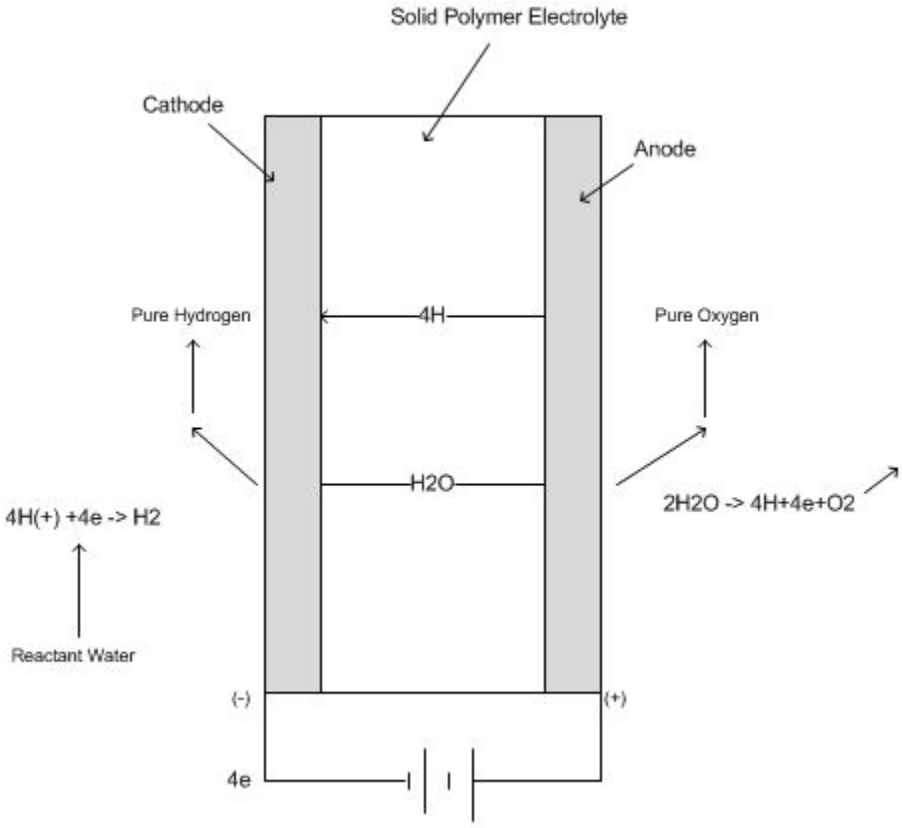

Figure 10. The electrolysis process [27].

where the released hydrogen gas would transfer. The hydrogen and oxygen were stored in different tanks before going through the injector for combustion [27].

Different organizations have also developed their own water electrolysis thrusters. Cornell University has developed a 2U prototype thruster with three main components: water tank with electrolysis, combustion chamber, and nozzle [35]. This 2U system was tested in a 3U CubeSat to determine the amount of ΔV it can produce. This electrolysis system used a proton exchange membrane, which is different from the Stechman *et al.* electrolyzer system. Distilled water can be used as propellant to replace deionized water because the PEM electrolyzer does not require dissolved electrolytes in the water. In this design, the products of gaseous hydrogen and oxygen from the electrolysis process would both remain in the storage tank instead of a separate hydrogen and oxygen tank. Electrolysis increases the pressure of the water tank as the amount of gas increases. Once the oxygen and hydrogen mixture reaches the required pressure, 10 bar or higher, a solenoid value would allow the mixture into the combustion chamber. A small spark plug is used to combust the gas mixture in the combustion chamber. According to prototype testing reported by Zeledon and Peck, the thruster was able to provide an average ΔV of 1.9 m/s per burst for the 3U CubeSat and an estimated 350 sec of specific impulse [35][36].

NASA LeRC Group, Hamilton Standard, and Lawrence Livermore National Laboratory also developed and tested an electrolysis propulsion system. This system used the sulfonic acid PEM as the sole electrolyte. This electrolysis cell consisted of a water feed chamber, a water permeable membrane, a hydrogen chamber, a SPE membrane, an oxygen chamber, an electrochemical hydrogen pump, and electrical insulators on both end plates. This system was very similar to Stechman's model described earlier. For this study, two flight-type thrusters with different mass and a 23.3 expansion ratio were built. A 22N thruster demonstrated over 69,000 firings with a total burn

time of four hours, and it produced a specific impulse of 355 sec at 50 psia chamber pressure. The second one for the same program, a 0.5 N thruster, demonstrated over 150,000 firings with a total burn time of 10 hours, and it produced a specific impulse of 331 sec at 80 psia chamber pressure. Their studies showed an increase in storage pressure also increased the required power and generation rates. However, the electrolysis conversion efficiency decreased gradually with increasing electrolysis pressure, due to the energy required for gas compression and the internal hardware configuration. Therefore, a tradeoff was required for the propulsion system between better efficiency and higher electrolysis pressure. The average electrolyzer efficiency is defined as the minimum power theoretically required for water electrolysis divided by the actual power used. This remaining power is rejected as heat. According to McElroy, typical efficiency values for electrolysis was between 85 and 90% [16].

2.5 Hydrogen-Oxygen Combustion

The water electrolysis thruster uses the gaseous hydrogen and oxygen for combustion to produce water vapor. This stoichiometric reaction is shown below.

$$2H_2(g) + O_2(g) \rightarrow 2H_2O(g) \tag{18}$$

This reaction is a global reaction, and it does not happen directly. In order to make this global conversion of hydrogen and oxygen to water occur, elementary reactions need to happen first. The four reactions listed below are the main elementary reactions.

$$H_2 + O_2 \rightarrow HO_2 + H \tag{19}$$

$$H + O_2 \rightarrow OH + O \tag{20}$$

$$OH + H_2 \rightarrow H_2O + H \tag{21}$$

$$H + O_2 + M \rightarrow HO_2 + M \tag{22}$$

When hydrogen and oxygen molecules first collide and react, they do not produce water. In fact, it was shown in reaction (19) that hydrogen and oxygen molecules collide and produce HO_2 and H. HO_2 is the intermediate species. During this reaction process, only one bond is broken, and one bond is formed. H_2 and O_2 forming two OHs is unlikely because it requires breaking and creating two bonds [30].

A collection of elementary reactions necessary to describe an overall reaction is called a reaction mechanism. In the case of hydrogen-oxygen combustion, this reaction mechanism has as much as 40 reactions and involves eight species: H_2, O_2, H_2O, OH, O, H, HO_2, and H_2 O_2. The H_2-O_2 system not only plays an important role in rocket propulsion, but it is also an important subsystem in the oxidation of hydrocarbons and moist carbon monoxide [30]. H_2-O_2 mechanism consists of initiation, branching, recombination, and diffusion. The initiation reactions are:

$$H_2 + M \rightarrow H + H + M \tag{23}$$

$$H_2 + O_2 \rightarrow HO_2 + H \tag{24}$$

Initiations are related to hydrogen dissociation, because the dissociation energy of hydrogen is lower than that of oxygen. Only a few radicals are required to initiate the explosion in the 675 K temperature region. Reaction (23) is for higher temperatures, and it requires about 435 kJ/mol. Reaction (24) is for other temperatures, and it has a lower energy requirement of only 210 kJ/mol. The main feature of the initiation step is to provide a radical for the chain system [3].

Next is the chain branching state. The chain reactions are shown below, and they

involve O, H, and OH radicals.

$$H + O_2 \rightarrow O + OH \tag{25}$$

$$O + H_2 \rightarrow H + OH \tag{26}$$

$$H_2 + OH \rightarrow H_2O + H \tag{27}$$

$$O + H_2O \rightarrow OH + OH \tag{28}$$

For reaction (26), the H radical is generated, and there is no chemical mechanism barrier to prevent the system from being explosive. The reverse reactions for (25), (26), and (28) are negligible because their concentration levels in many systems are very low. Apart from chain branching, reactions (25)- (28) also provide the essential propagating steps and the radical pool for fast reactions. [3]

The explosion limit for hydrogen-oxygen mixture is shaped like a reverse S-curve. Figure 11 shows the explosion limit curve for a stoichiometric hydrogen-oxygen mixture. This is a branched-chain explosion. The explosion limits must be specified in terms of the chemical-kinetic and diffusion parameters that determine the rates of chain branching and chain breaking notably temperature, pressure, mixture composition, and environmental conditions. In the explosive region, the rate of chain branching is greater than the rate of chain breaking. In the no explosion region, the relationship is reversed. At the limit line, the two rates are equal [13].

H and OH wall destructions are important chain termination steps.

$$H \rightarrow wall \quad destruction$$

$$OH \rightarrow wall \quad destruction$$

These two steps explain the lower limit of hydrogen-oxygen mixture explosion. Wall

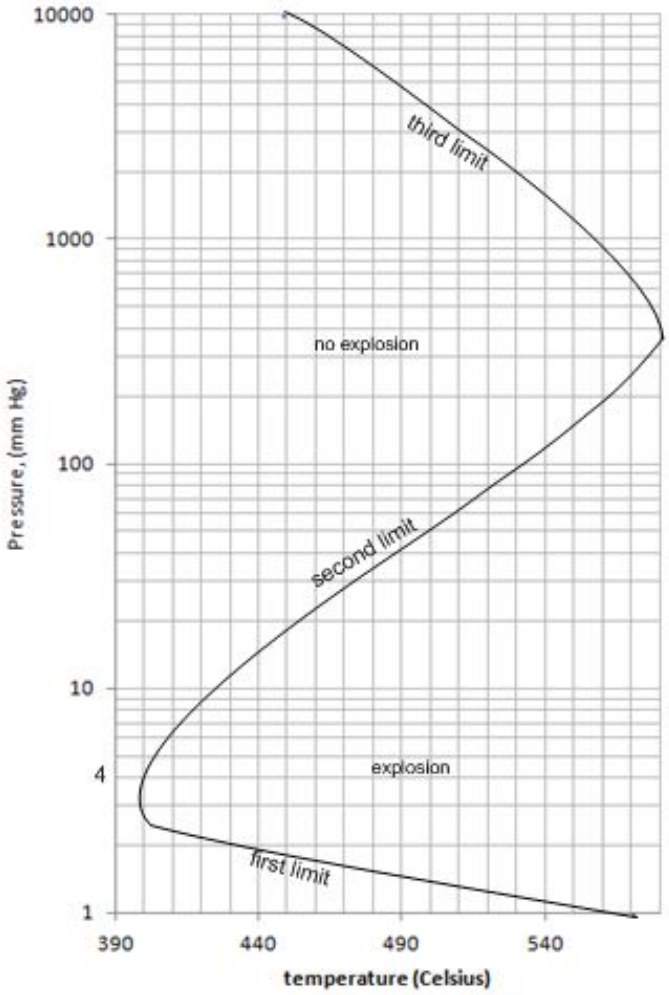

Figure 11. Explosion limits of a stoichiometric hydrogen-oxygen mixture [13]

collisions are more predominant at a lower pressure compared to molecular collisions. The second explosive limit is caused by gas phase production and destruction of radicals. For this to occur, the most effective chain-branching reaction, which is reaction (25), must be overridden by another reaction step. When a system with a fixed temperature is moving from a lower pressure to a higher pressure, the system transitions from an explosive state to a steady reaction condition, which is the other side of the second limit. The reaction step that overrides the chain-branching reaction must be more pressure sensitive [3].

The existence of the second explosion limit is readily explained if the three-body

reaction is added to the scheme. This reaction is:

$$H + O_2 + M \rightarrow HO_2 + M \tag{29}$$

where M denotes any third molecule that stabilizes the combination of H and O_2. The free radical HO_2 is considered to be relatively unreactive, so that it is able to diffuse to the wall and become a means for effectively destroying H radicals. Reaction (29) does not require activation energy. Therefore, a range of temperatures and pressures exists at which the two reactions proceed at equal rates. According to the Arrhenius function of the chain-branching reaction, the limit pressure increases with increasing temperature, because the chain-branching rate increases with increasing temperature. [13]

The upper third explosion limit is caused by a reaction that overtakes the stability of the HO_2.

$$HO_2 + H_2 \rightarrow H_2O_2 + H \tag{30}$$

Higher temperatures are required for reaction (30) to become effective, because the reactivity of HO_2 is much lower than OH, H, or O. Due to some resonance energy exchange with the HO_2 formed, water vapor tends to inhibit explosion due to the effect of reaction (29), in that H_2O has a high third-body efficiency [3]. Reaction (29) is a recombination step requiring a third body, M, so its rate decreases with increasing temperature. Conversely, reaction 16 increases with temperature. Thus, it can be concluded that reaction (29) is more effective at higher pressures and lower temperatures, while reaction (25) dominates at higher temperatures and lower pressures. Therefore, at temperatures above 875 K, where the third explosion limit starts, reaction 16 always prevails, and the mixture is explosive for the complete pressure range covered.

In this third-limit explosion regime, the chain-terminating steps involving O, H, and OH radicals are the three-body recombination reactions. The main gas-phase termination steps are the following [3]:

$$H + H + M \rightarrow H_2 + M \tag{31}$$

$$O + O + M \rightarrow O_2 + M \tag{32}$$

$$H + O + M \rightarrow OH + M \tag{33}$$

$$H + OH + M \rightarrow H_2O + M \tag{34}$$

In order to complete the mechanism, reaction (29) needs to occur again to produce more HO_2 [30]. After reaction (29), HO_2 may be consumed in the H_2-O_2 system by various radicals. The reactions are as follows:

$$HO_2 + H \rightarrow H_2 + O_2 \tag{35}$$

$$HO_2 + H \rightarrow OH + OH \tag{36}$$

$$HO_2 + H \rightarrow H_2O + O \tag{37}$$

$$HO_2 + H \rightarrow O_2 + OH \tag{38}$$

$$HO_2 + OH \rightarrow H_2O + O_2 \tag{39}$$

Then, the HO_2 radicals will recombine with each other to yield H_2O_2.

$$HO_2 + HO_2 \rightarrow H_2O_2 + O_2 \tag{40}$$

Afterward, H_2O_2 will consumed by reactions with radicals and go through thermal

decomposition [30][3].

$$H_2O_2 + OH \rightarrow H_2O + HO_2 \tag{41}$$

$$H_2O_2 + H \rightarrow H_2O + OH \tag{42}$$

$$H_2O_2 + H \rightarrow HO_2 + H_2 \tag{43}$$

$$H_2O_2 + M \rightarrow 2OH + M \tag{44}$$

Finally, although reaction (29) was acting as a chain-terminating step under some conditions, especially at high temperature, under other conditions it is part of a chain propagating path to obtain the final H_2O product.

III. Test Methodology and Procedures

3.1 Introduction

This chapter reviews the equipment and connections set-up necessary to perform vacuum testing of the HYDROS^{TM} thruster. This research was performed in the environmental testing facility located at the Air Force Institute of Technology (AFIT). A torsional balance thrust stand was used to capture impulse bit data. In order to record the proper measurements, calibration of the thrust stand prior to testing was required. The nozzle designs for this research were modeled using a nominal two-dimensional conical geometry. The theoretical data calculation method was presented in Chapter 2. The theoretical data was calculated in this chapter. Lastly, the comparison between the theoretical data and experimental data are presented in Chapter 4.

3.2 Equipment and Connections

3.2.1 Vacuum Chamber.

The main equipment for this experiment included a vacuum chamber, thruster, and thrust stand. The vacuum chamber for this research, shown in Figure 12, is a horizontally-mounted chamber by PHPK Technologies. This chamber is capable of pumping down to 10^{-4} Torr. This chamber opens by the door located in the front side of the chamber. There is a sliding table located inside the chamber, which allows easy assess to equipment. This vacuum chamber has a 60" diameter and is approximately 60" long. It is constructed of 3/8" thick 304 series stainless steel mounted to a painted steel base. Vacuum feedthroughs are located around the chamber, as well as the back side of the chamber. A five-inch feedthrough with two DB15 sub-connections was used for this research. Connections for both sides are shown in Figure 13. A window

Figure 12. Space simulator vacuum system.

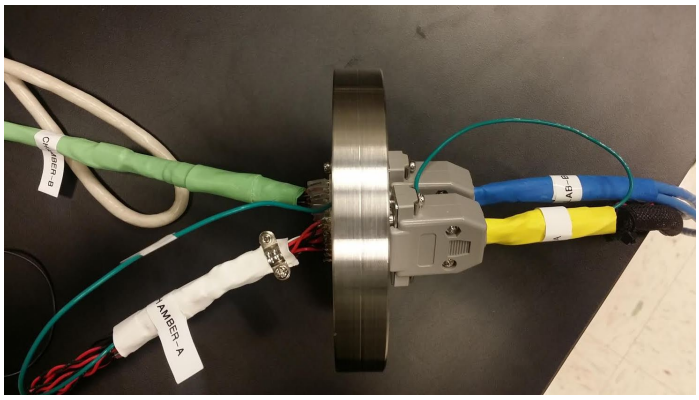

Figure 13. Vacuum to lab connections.

is also located on the back side of the chamber, which allows for visibility inside the chamber for camera set-up. This is shown in Figure 14.

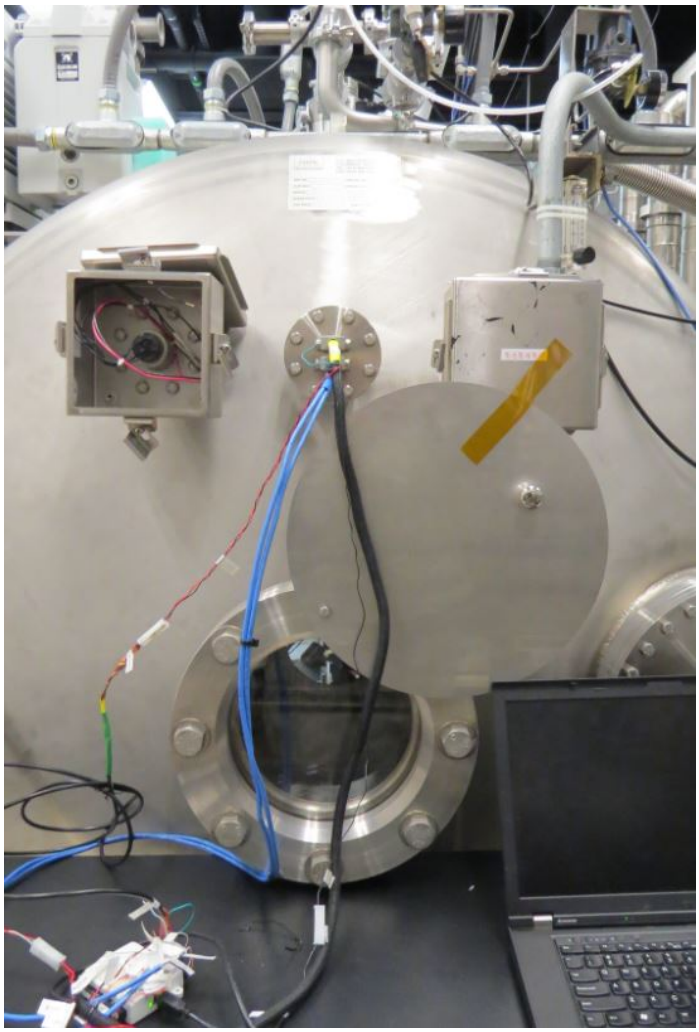

Figure 14. The window and passthrough location.

3.2.2 Torsional Balance Thrust Stand.

Thrust stand selection is critical for this research in order to obtain repeatable and accurate results. This thruster does not produce a steady state force; rather, it produces an impulse force. The selected thrust stand must have a high-frequency sensor capable of capturing an approximately 0.3-second impulse. In addition, the thrust stand is required to measure a thrust event between 0.1-0.5 N. A torsional balance thrust stand by Tethers Unlimited Inc. was selected for this research. Unlike the inverted pendulum thrust stand, a torsional balance thrust stand's rotational axis

is parallel to the gravity vector, making its response less dependent on thruster mass. This makes it ideal for measuring the HYDROS^{TM}, because the thruster mass is not constant throughout testing. Research studies had shown that torsional thrust stands were inherently more stable than inverted-pendulum thrust stands and offer a balance of high-thrust measurement sensitivity and low-environmental noise sensitivity [22]. Research from Koizumi, Komurasaki, and Arakawa measured that the overall thrust stand impulse accuracies are typically 2.1μN-s for an impulse range of 20-80 μN-s and 0.7μN-s for an impulse range of 1-10N-s [10].

This torsional balance thrust stand consists of a swinging arm used to mount the thruster. The swinging arm is divided by a centerline, where the counterweights are located on both ends of the arm. The counterweights are placed on the arm for balance and to ensure the arm is parallel to the sensor. The center axis is mounted to a frame via two torsional springs. An image of the complete set-up is shown in Figure 15.

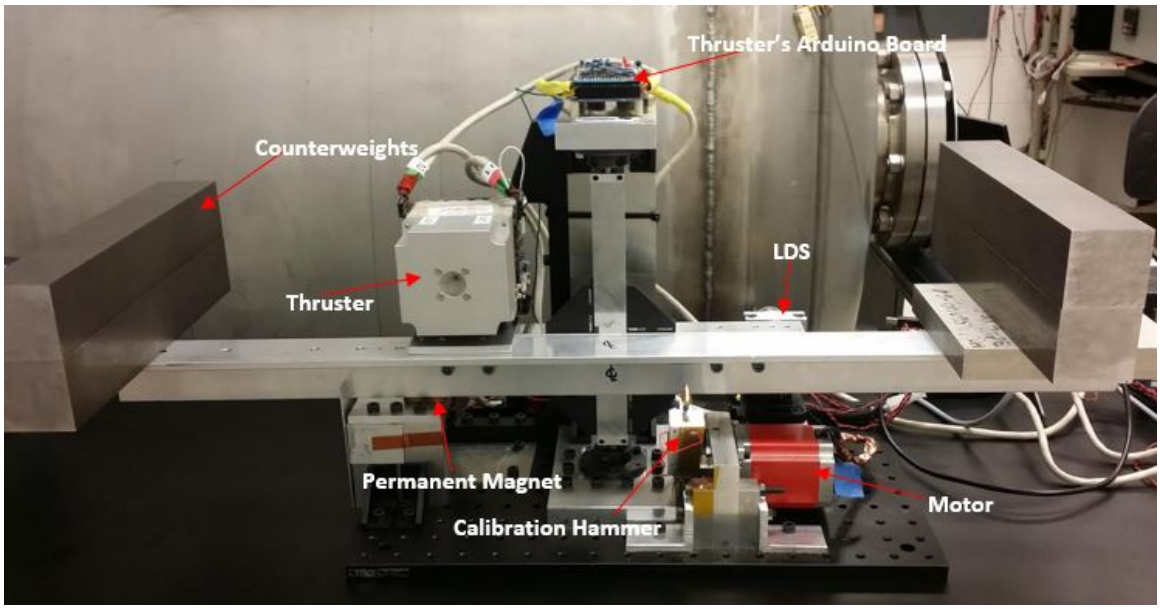

Figure 15. Rotational balance thrust stand with thruster.

The thruster is mounted horizontally to the left of the center line. While the

calibration hammer and linear displacement sensor (LDS) are not directly mounted on the swinging arm, they are located on the right side of the centerline. The hammer has an integrated piezoelectric force transducer and is used for calibration purposes prior to each set of tests. Research from Pancotti and Hilario showed piezoelectric hammers have linearity within 0.99% for a range of of 10 mN-s to 750 mN-s [21]. A motor is used to control the hammer. A detailed image of the hammer and its motor are shown in Figure 16. The hammer provided an impulse force to the thrust stand

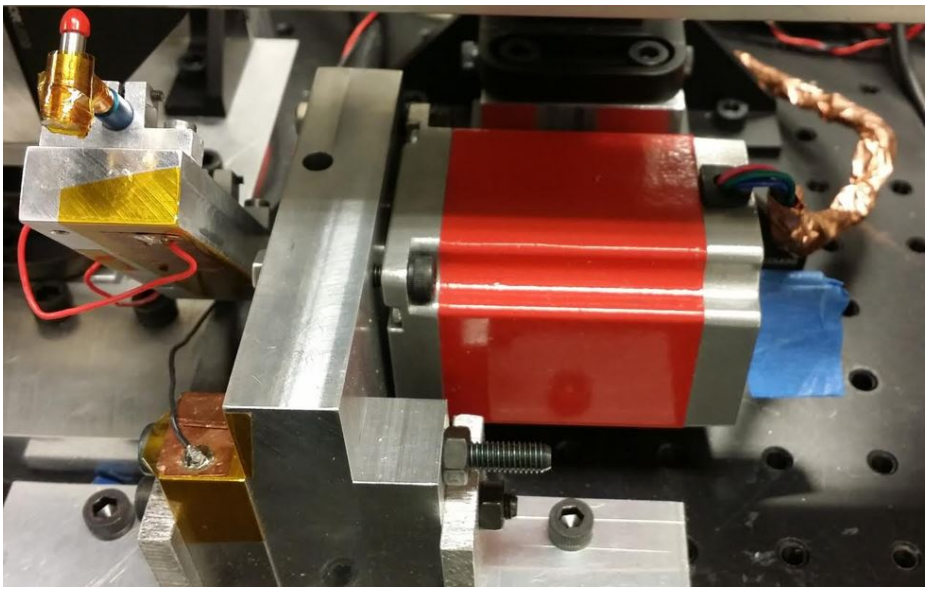

Figure 16. Calibration hammer and motor.

and the LDS is used to measure the response to a known impulse input from the hammer. When the thruster is fired on the thrust stand, the LDS will measure the displacement response in voltage through Labview. The calibration data can measure the impulse bit of the thruster. A micro-adjuster is located below the LDS. The set-up of the LDS and its adjuster are shown in Figure 17. The total set-up of the whole system inside the vacuum chamber is shown in Figure 18.

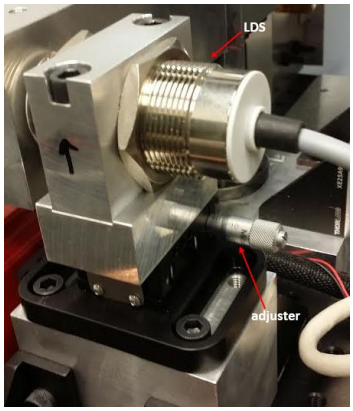

Figure 17. LDS and micro-adjuster.

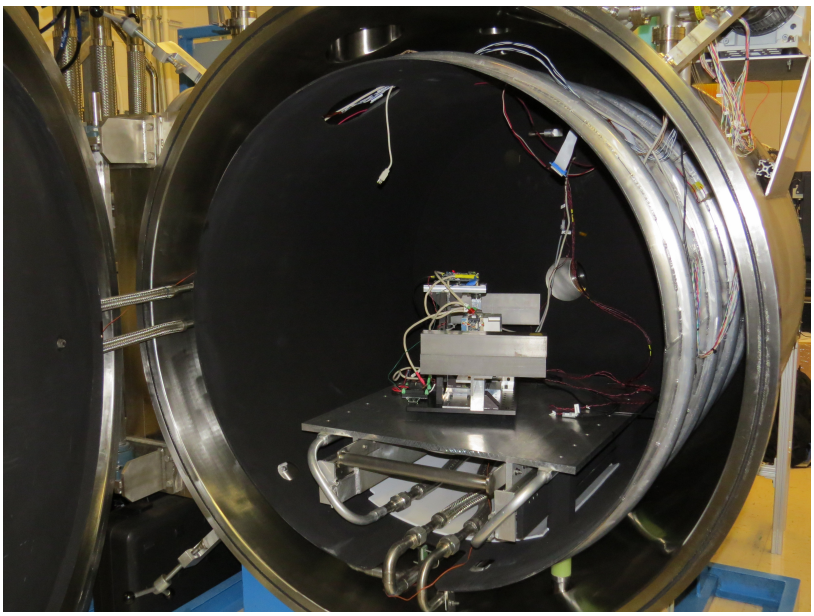

Figure 18. Thruster stand and thruster inside the vacuum chamber.

3.2.3 Thruster.

The thruster used for this experiment is the HYDROS^{TM} thruster, shown in Figure 19. This 1U configuration thruster has an empty mass of 0.875 kg and is capable of storing approximately 0.075 kg of water. This thruster is comprised of six main components: a water tank, a H_2 gas tank, an O_2 gas tank, an injector, a combustion chamber, and a nozzle. Water breaks down through the electrolysis process to create gaseous hydrogen and oxygen. The hydrogen gas and oxygen gas store separately

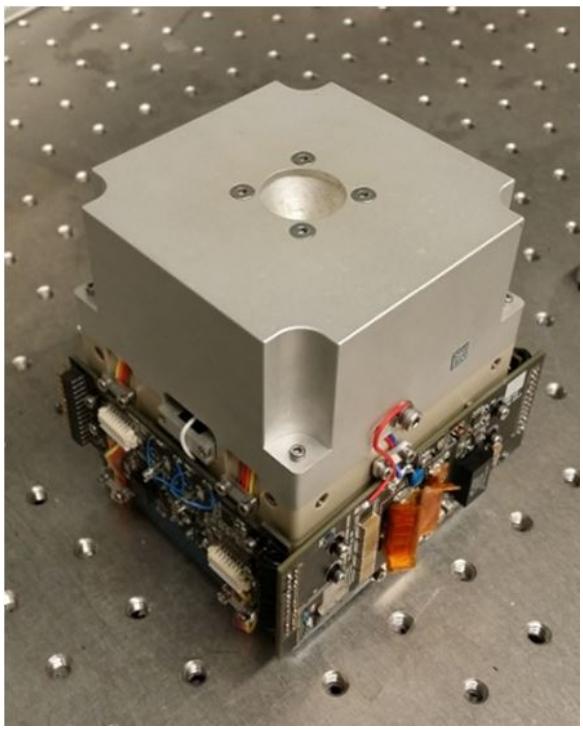

Figure 19. The HYDROS^{TM} thruster used for this research.

before entering the injector for combustion. The hydrogen gas tank has a volume of 12.9 cm^3, and the oxygen gas tank has a volume of 6.6 cm^3.

In order to fire the thruster, a computer running Labview sends commands and receives data from the thruster. The computer is connected to a data acquisition device (DAQ), used to convert the wire signals from digital to analog and also from analog to digital. The DAQ is connected to an Arduino board. The Arduino board communicates and runs the thruster. The Labview screen is shown in Figure 20.

There are four controls to the thruster: pressurize, vent, emergency hydrate, and fire. The thruster is only fired after it reaches a commanded pressure. During the normal pressurizing process, the electrolyzer voltage runs at approximately 2.3 V and the electrolyzer current draws between 0.3 and 1 A. Under these conditions, the pressurization time is about two to three minutes per fire. The electrolyzer current drops after each firing. After approximately eight firings, the electrolyzer current

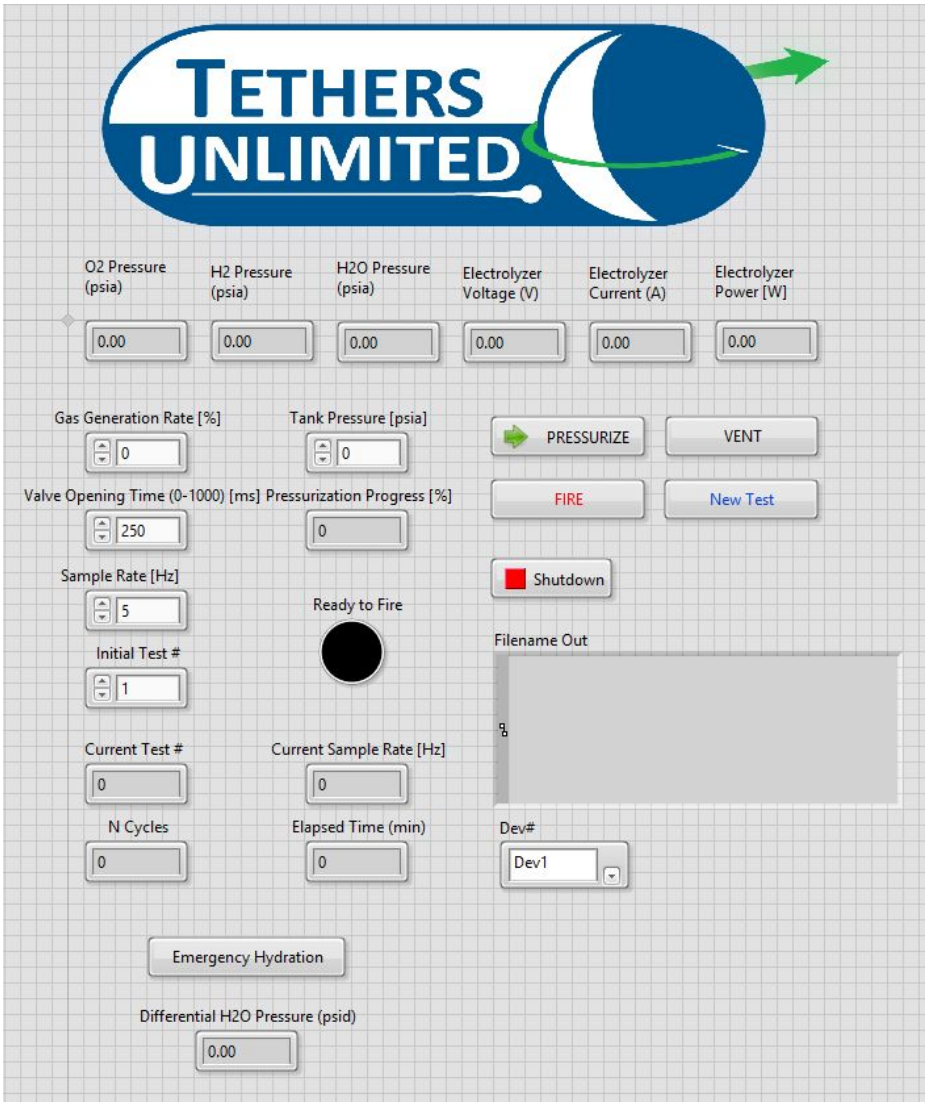

Figure 20. The HYDROS^{TM} thruster interface GUI used for this research.

drops below 0.2 A. In order to continue, an emergency hydrate is required to wet the membrane.

3.2.4 Equipment set-up.

The connections set-up were divided between the lab side and the vacuum side. The vacuum side consists of the complete set-up of the thrust stand and the thruster, as shown in Figure 15. There are two DB15 cables connected to the feedthrough

on the vacuum side labeled Chamber-A and Chamber-B. The Chamber-A connector connected to the thruster's Arduino board and the LDS. The chamber-B connector is connected to the hammer and motor.

On the lab side, there is a PCB signal conditioner, two power supplies, a calibration Arduino board, a Data Acquisition (DAQ) system, and a laptop. The set-up is shown in Figure 21. All of this equipment was connected through two 15 pin bundle cables

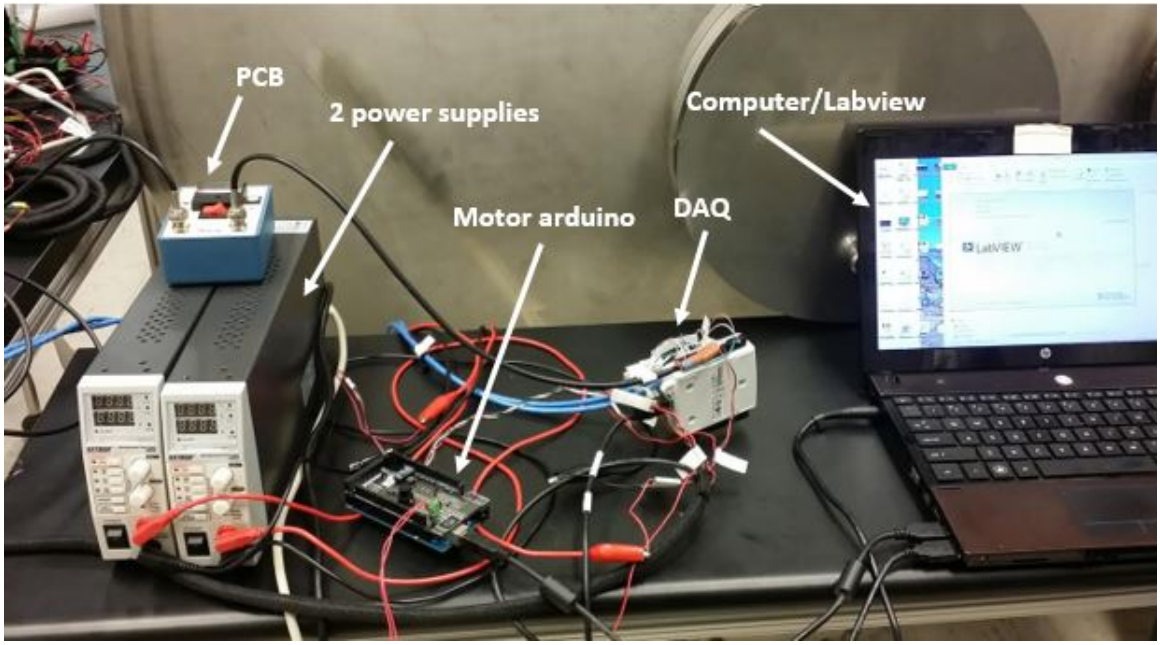

Figure 21. The lab side set-up.

similar to the vacuum side. They were labeled Lab-A and Lab-B, and connected to Chamber-A and Chamber-B respectively. Lab-A was connected to the DAQ system, and it sent and received signals to the thruster's Arduino board. The DAQ system was connected to the labtop to run Labview. A power supply up to 10-volt and 1.5-amp was required for the thruster.

Lab-B was used to communicate with the hammer and motor on the vacuum side. The signals from the hammer went through the PCB signal conditioner. The output of these signals was connected to the DAQ system. Another Arduino board was used to control the hammer's motor, and required a 24V power supply. A diagram of the

complete set-up is shown in Figure 22.

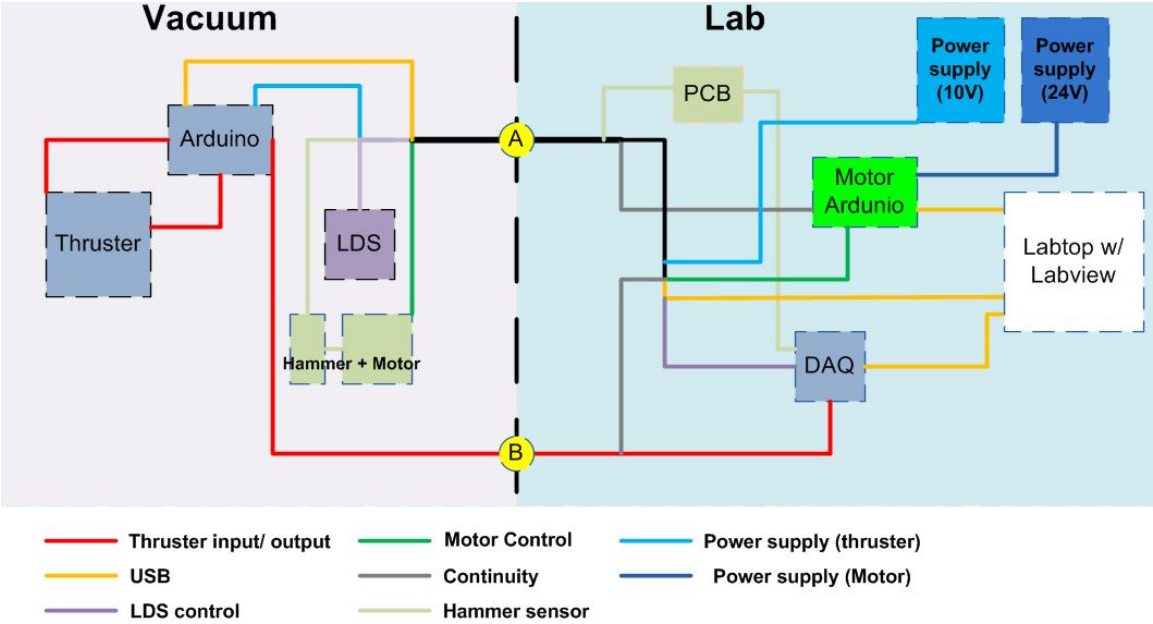

Figure 22. The complete experiment set-up.

After all the cables were connected properly, testing was performed in vacuum. Prior to each vacuum pump down, the measurement of the thruster's mass was important. It was critical to keep track of how much fuel was used during a firing set for later calculations. In addition, before the vacuum was pumped down, the adjustment of the counterweights' position to ensure the swinging arm was parallel to the LDS was also critical. This is shown in Figure 23. Furthermore, it was important to ensure the LDS was in the correct position relative to the swinging arm. The displacement voltage on the Labview screen should read 5V (+/- 0.5V). If the voltage was not 5V, then the LDS required adjustment through the micro-adjuster attached below the LDS. This could only be adjusted in atmosphere manually. Finally, the vacuum chamber was ready to pump down for experiments.

A HPV2 high-speed camera was used to capture the thruster's exhaust plume. This camera was used to capture high-speed images up to a million frames per second at intensity gains up to 50x. The camera can records 102 frames at a time. The set-up

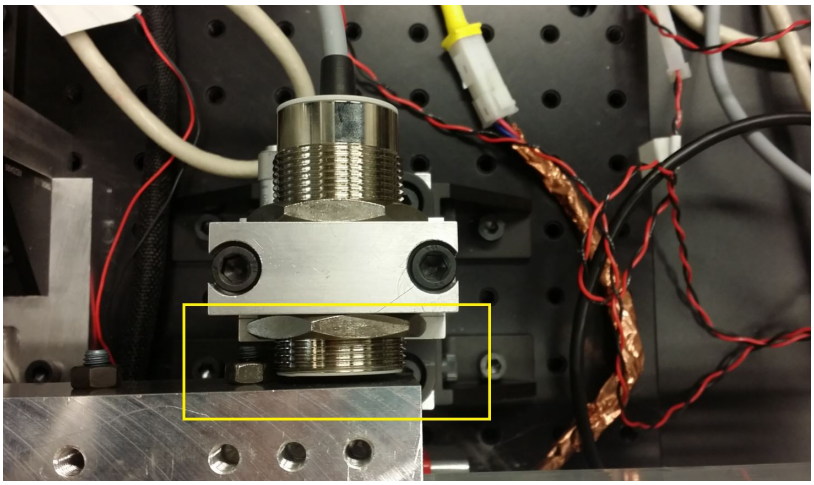

Figure 23. Swinging arm with LDS.

of the camera is shown in Figure 24. The camera is triggered by the fire signal from the Labview VI. For this experiment, all images were captured at 250 or 500 frames per second. The time delay between sending the pressurization command and the moment ignition occured apparently changed each time, thus, it was very difficult to capture the firing faster than 500 frames per second.

Figure 24. The camera set-up.

3.3 Calibration of Torsional Balance Thrust Stand

After the vacuum chamber was pumped down, before each testing set, thruster calibration was required to determine how the thrust stand responded to a known force. The purpose of this calibration was to properly measure the impulse bit of the thruster. The calibration determined the response to an impulse force. Thus, this response can be used to calculate the impulse force of the thruster. A set-up diagram, shown in Figure 25, displays a more simplified diagram of the thrust stand for reference.

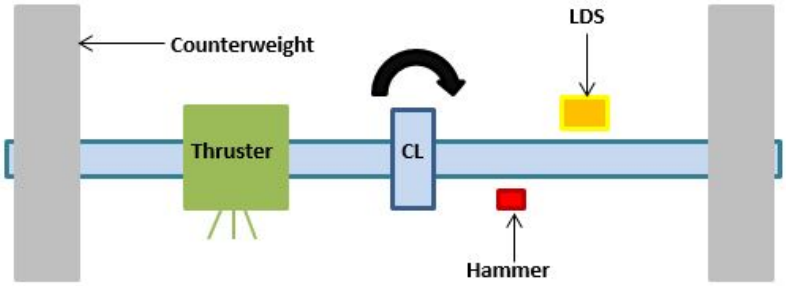

Figure 25. The top view of the thrust stand.

The calibration required a known force. For this particular thrust stand, a small hammer was used. This hammer is used to tap the arm of the thrust stand and measure the applied impulse force with an integrated piezoelectric force transducer. The location of the hammer from the center axis and the location of the thruster from the center axis are different, therefore, a relationship between the two forces is required. This equation is shown in Eq. (45),

$$F_{hammer} l_{hammer} = F_{thruster} l_{thruster} \tag{45}$$

where l_{hammer} and $l_{thruster}$ are fixed distance. Rearranging Eq. (45),

$$F_{thruster} = F_{hammer} \left(\frac{l_{hammer}}{l_{thruster}} \right) \tag{46}$$

$l_{hammer}/l_{thruster}$ is the scaling factor for the thruster impulse force.

The calibration process began by applying an impulse force with the hammer. First, an Arduino board, and its associated software, were used to send commands to the motor to apply a fixed impulse to the thrust stand. The hammer's impact would cause the swinging arm to oscillate. Second, Labview was used to record and output the signal from the force transducer on the hammer, as well as the arm deflection data from the LDS. After all the data were recorded, Matlab was used to analyze the

relationship between arm deflections and impulse bits.

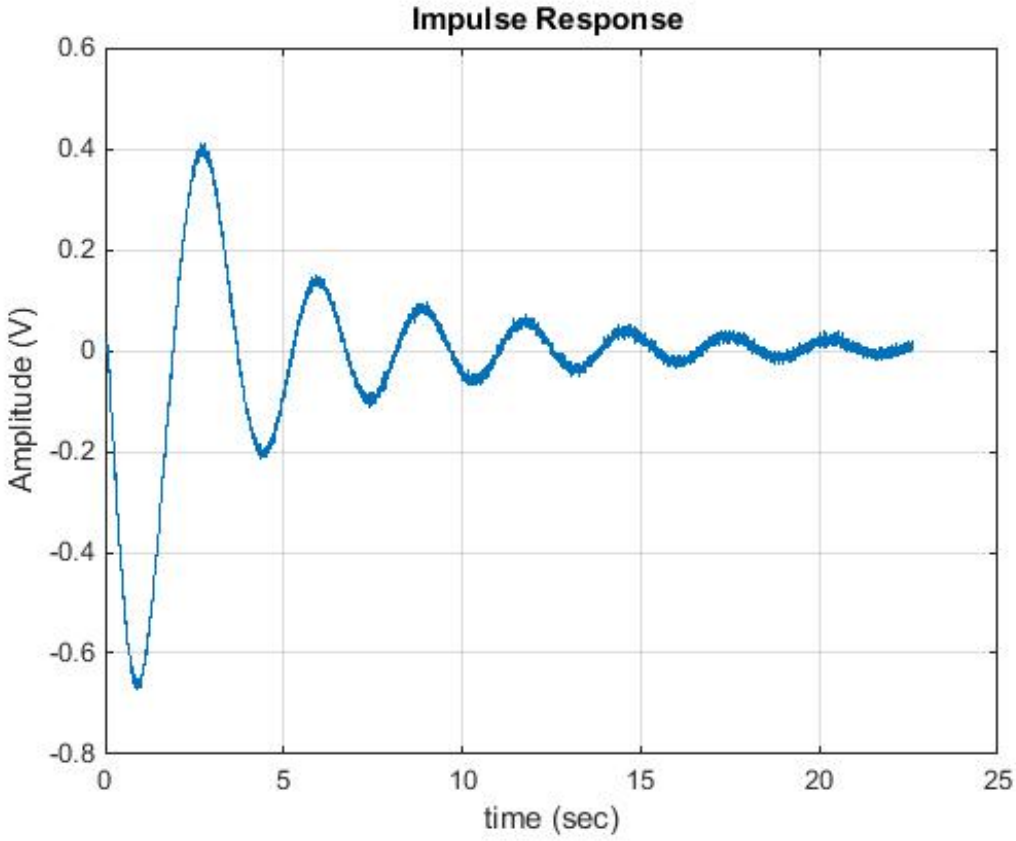

Figure 26. Hammer impulse response.

Figure 26 shows an impulse response from the LDS. This response is a sinusoid impulse response with an exponential decay from dampening. The estimated equation of this response is shown in Eq. (47),

$$y(t) = Asin(\omega_n t)e^{-\xi\omega_n t} \tag{47}$$

where A is the amplitude in Volts, t is the time in seconds, ξ is the damping ratio, and ω_n is the natural frequency of the system. A, ξ, and ω_n are the three unknown in the equation. The amplitude at approximately one second in Figure 26 is lower than the overall response amplitude due to the effects of damping.

To find an accurate relationship between deflections and impulse bits, the original amplitude without damping is needed. Figure 27 shown the main data points required to find the original amplitude. The amplitude at point B and D are used in Eq. (48),

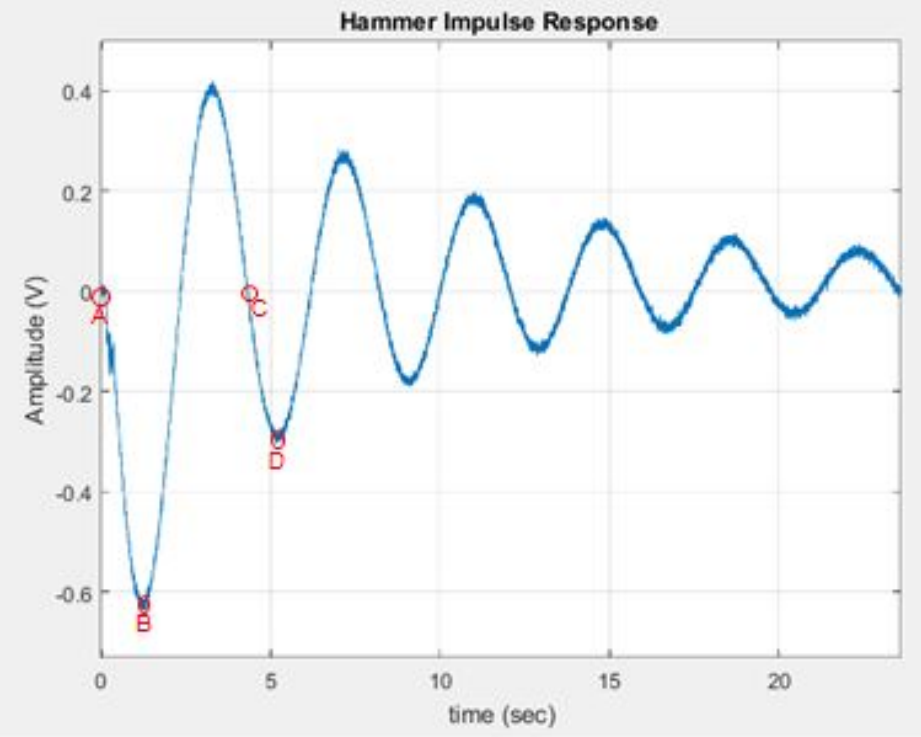

Figure 27. Impulse repsonse with key points.

itself derived from Eq. (47).

$$\Delta A = \frac{D}{B} = e^{-\xi\omega_n \Delta t} = e^{-\xi\omega_n (t_D - t_B)} \tag{48}$$

Through Eq. (48), the term $\xi\omega_n$ was obtained. ω_n can be found using Eq. (49):

$$\omega_n = \frac{2\pi}{t_c - t_A} \tag{49}$$

Using Eq. (50), the original amplitude without damping was obtained by dividing the

measured amplitude by $e^{-\xi\omega_n\Delta t}$.

$$A_{original} = \frac{A_{meausured}}{e^{-\xi\omega_n(t_B - t_A)}} \tag{50}$$

A new curve is plotted using the original amplitude with the estimated equation. Eq. (51) is the equation for this new curve.

$$y_{original}(t) = \frac{A_{measured}}{e^{-\xi\omega_n(t_D - t_B)}} sin(\omega_n t) e^{-\xi\omega_n t} \tag{51}$$

A comparison between the measured response and the new response is shown in Figure 28.

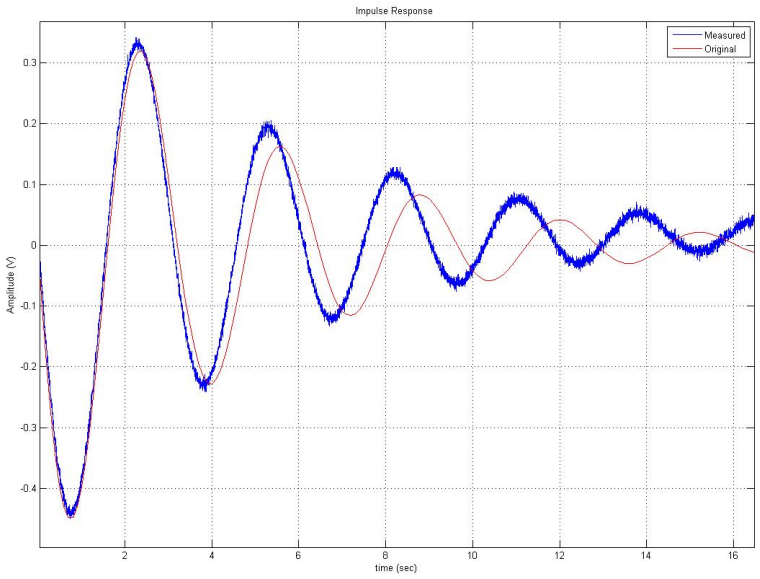

Figure 28. The measured response and the new response with the original amplitude.

Before finding a unit response, both amplitude and time need to off-set back to zero. After finding the new response with the undamped amplitude, this response is used to obtain a unit response. First, the impulse bit of the hammer input needed to be found. An example of the hammer input is shown in Figure 29.

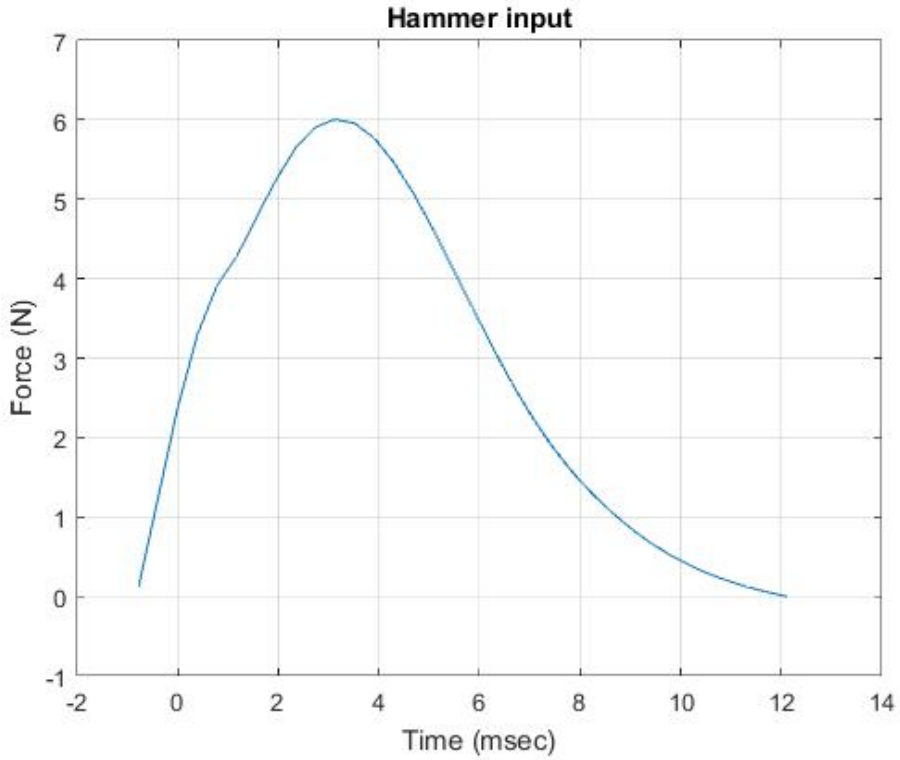

Figure 29. An impulse input from the hammer.

The trapezoidal numerical integration method was used to determine the impulse bit of the hammer impulse. The equation for calculating the unit-response is shown in Eq. (52).

$$Unit - response = \frac{y_{original}(t)}{i_{bit}} \tag{52}$$

The unit response represents the impulse response for one N-s of impulse. This unit response is used to compare the impulse response of the thruster in order to determine the impulse bit of the thruster. Figure 30 shows an example of the hammer unit response.

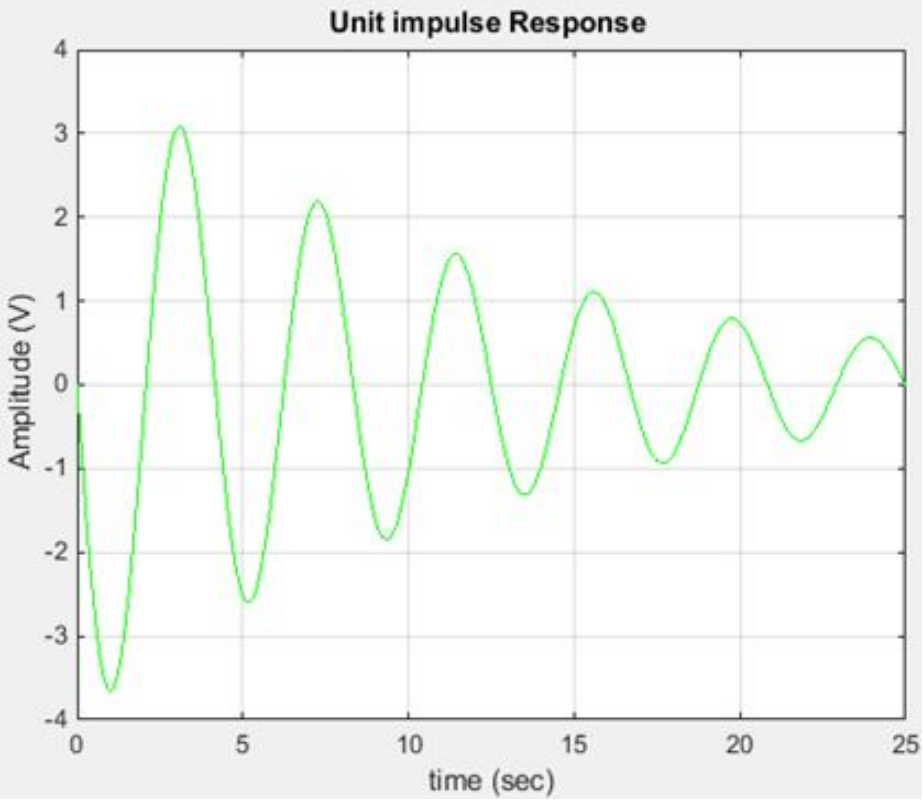

Figure 30. An example of a hammer unit response.

3.4 Theoretical Calculations

The purpose of redesigning the nozzle for this research is to improve the efficiency and I_{sp} of the system. Different nozzle design approaches apply to different systems, because different systems have different effects based on their Reynolds number, fuel properties, and flow conditions. For example, a higher-expansion ratio may be good for a high Reynolds number system but not necessarily for a system with a lower Reynolds number. The Reynolds number for this system was best estimated to provide an idea of the possible range this system is in. The Reynolds number can help understand the kind of nozzle design the HYDROS$^{\text{TM}}$ thruster needs. The Reynolds number of the throat is calculated using Eq. (53) [7],

$$Re = \frac{\rho V D}{\mu} = \frac{\dot{m} D}{A \mu} = \frac{4\dot{m}}{\pi D \mu} \tag{53}$$

where $\dot{m}$ is the mass flow rate in kilogram-per-second calculated, D is the diameter of the throat in meters, and μ is the dynamic viscosity of the gas in Pascal-second.

The Reynolds number calculation, dynamic viscosity, and all other combustion conditions are approximated using Chemical Equilibrium with Applications (CEA). The CEA calculations were based on a 20% drop of a 49-psi plenum pressure, which is about 40-psi chamber pressure. The oxidizer-to-fuel ratio for hydrogen-oxygen combustion is 8, due to a stoichiometric combustion assumption. The dynamic viscosity from CEA is 1 x 10^{-4} Pa-sec. Using Eq. (53), the Re number becomes 2238. The CEA data represents the ideal case for hydrogen-oxygen combustion. The ideal mass flow rate was also calculated to compare to the mass flow rate based on the vacuum data. Using Eq. (54),

$$\dot{m} = \rho A V \tag{54}$$

with density of the throat, $\rho = 9.57$ x 10^{-2}, the throat velocity, $V = 1362.6$ kg/s, and the ideal mass flow rate, $\dot{m} = 1.6$ x 10^{-4} kg/s.

Another criterion to investigate is the optimal expansion ratio. This is the theoretical maximum. An increase in expansion ratio can increase the thrust of a system up to a limit. This maximum point is the optimal expansion ratio, where the exit pressure is approximately equal to the ambient atmospheric pressure. The optimal expansion ratio can help determine the maximum thrust, I_{sp}, and the optimal thrust coefficient of which this thruster is capable. However, these calculations are not as accurate for this small-scale thruster, because these calculations do not include conditions, such as incomplete combustion, and most importantly, viscous effects. The optimal expansion ratio is calculated through the exit Mach number. Exit velocity is

required to obtain mach number. Eq. (55) is the equation for exit velocity.

$$V_2 = \sqrt{\left(\frac{2k}{k-1}\right) RT_1 \left[1 - \left(\frac{P_2}{P_1}\right)^{\frac{k-1}{k}}\right]} \tag{55}$$

where the specific heat ratio, k, is 1.11 from CEA, P_2 is assumed to be zero, the specific gas constant, R, for water vapor is 461.4 $\mathrm{J}kg^{-1}k^{-1}$, and the chamber pressure, T_1, is 3208 K from CEA. Using Eq. (55), the exit velocity is 5465.6 m/s. Using Eq. (56)),

$$M_2 = \frac{V_2}{\sqrt{kRT_2}} \tag{56}$$

the exit Mach number is infinite because T_2 is close to zero. Finally, the optimal expansion ratio is calculated using Eq. (57):

$$\frac{A_2}{A_t} = \left(\frac{k+1}{2}\right)^{-\frac{k+1}{2(k-1)}} [\frac{\left(1 + \frac{k-1}{2}M^2\right)^{\frac{k+1}{2(k-1)}}}{M}] \tag{57}$$

Since the temperature must drop to zero to provide an exit pressure of zero, the Mach number must be infinite and, therefore, the area ratio must be infinite.

P_2 equal to zero is the absolute best case. In order to obtain a more realistic expansion ratio, a slightly different approach was used.

$$\frac{T_2}{T_1} = \left(\frac{P_2}{P_1}\right)^{\frac{k-1}{k}} \tag{58}$$

Substitute Eq. (58) into Eq. (59) [28],

$$V_2 = \sqrt{\left(\frac{2k}{k-1}\right) RT_1 \left[1 - \frac{T_2}{T_1}\right]} \tag{59}$$

where T_2 is assumed to be the condensation point temperature of water vapor at 1

atm, 373 K. In addition, the specific heat ratio from CEA was on the low end. For the second approach, specific heat ratio for water vapor of 1.3 is used instead. P_2 is also not equal to zero, because this would require all potential energy be converted into kinetic energy. With this new approach, exit velocity becomes 3,367 m/s, the Mach number becomes 7.12, and the optimal expansion ratio becomes 314. The 15-degree conical nozzle length required to obtain an area ratio of 314 is 1.6 inches using Eq. (60).

$$L = \frac{r_t(\sqrt{\varepsilon} - 1) + R_n(sec(\theta) - 1)}{tan(\theta)} \tag{60}$$

Maximum C_F, T, and I_{sp} are now calculated using the expansion ratio. Eq. (61) is used to calculate C_F.

$$C_F = \sqrt{\frac{2k^2}{k-1}\left(\frac{2}{k+1}\right)^{\frac{k+1}{k-1}}\left[1 - \left(\frac{P_2}{P_1}\right)^{\frac{k-1}{k}}\right]} + \frac{P_2 - P_3}{P_1}\frac{A_2}{A_t} \tag{61}$$

Before solving for C_F, Eq. (62) and Eq. (63) are used to find P_2 in order to solve for C_F.

$$\frac{P_t}{P_1} = \left[\frac{2}{k+1}\right]^{\frac{k}{k-1}} \tag{62}$$

$$\frac{P_2}{P_t} = \left(1 + \frac{k-1}{2}M^2\right)^{-\frac{k}{k-1}} \tag{63}$$

P_2 is 0.0019 and C_F is 1.88. After calculating C_F, C^* is required to obtain I_{sp}. Using Eq. (64),

$$C^* = \frac{\sqrt{kRT_1}}{k\sqrt{\frac{2}{k+1}^{\frac{k+1}{k-1}}}} \tag{64}$$

C^* is 1,823.3 m/s. Using Eq. (65),

$$Isp = \frac{C^* C_F}{g_0} \tag{65}$$

the optimal I_{sp} is 349 sec. Equation (66) is used to calculate the optimal thrust.

$$T = C_F P_1 A_t \tag{66}$$

The optimal thrust for this system is 0.6355 N. A summary of the result is shown in Table 1. However, these optimal values in Table 1 do not represent the entire picture,

Table 1. Optimal Nozzle Conditions

k	P_2(Pa)	C_F	Isp(sec)	T(N)	L(m)	$\frac{A_2}{A_t}$	M_2
1.3	13.1	1.88	349	0.6355	0.04	314	7.12

because the calculations ignore viscous boundary layer effects in low Reynolds number flow.

Futhermore, Spisz *et al.* have conducted thrust coefficient studies on low-thrust nozzles for steady flow operations [26], The results from the studies indicated large area ratios were not required for achieving maximum thrust for nozzles with low throat Reynolds number (<10,000). Therefore, the HYDROS^{TM} thruster might not require a large expansion ratio to achieve maximum efficiency and performance. Figure 31, a figure regenerated from Spisz *et al.* data, indicated for Reynolds number of 2500, there was a loss of thrust coefficient due to viscous forces from 0.035 to 0.35, as expansion ratio increased from 2 to 400. Losses also increase as the Reynolds number decreased.

Spisz *et al.* also found the optimum thrust coefficient with area ratio for different throat Reynolds numbers. These are the net thrust coefficients, which included viscous losses. The optimal area ratio line is represented by the dash-line in Figure 32, which was generated with similar data. The data indicated that the gains due to the increased area ratio were less than the additional viscous losses imposed by the increased surface area [26]. For the HYDROS^{TM} thruster's Reynolds number range, based on this study, the optimum area ratio is approximately 22.

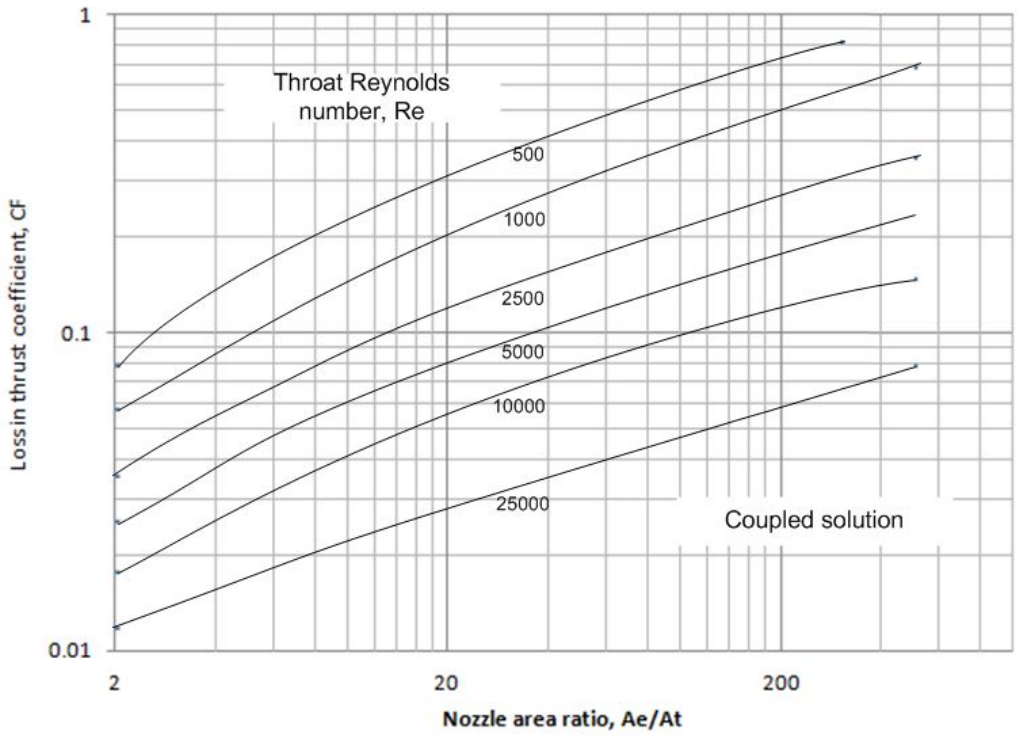

Figure 31. Loss in thrust coefficient due to viscous effects [26].

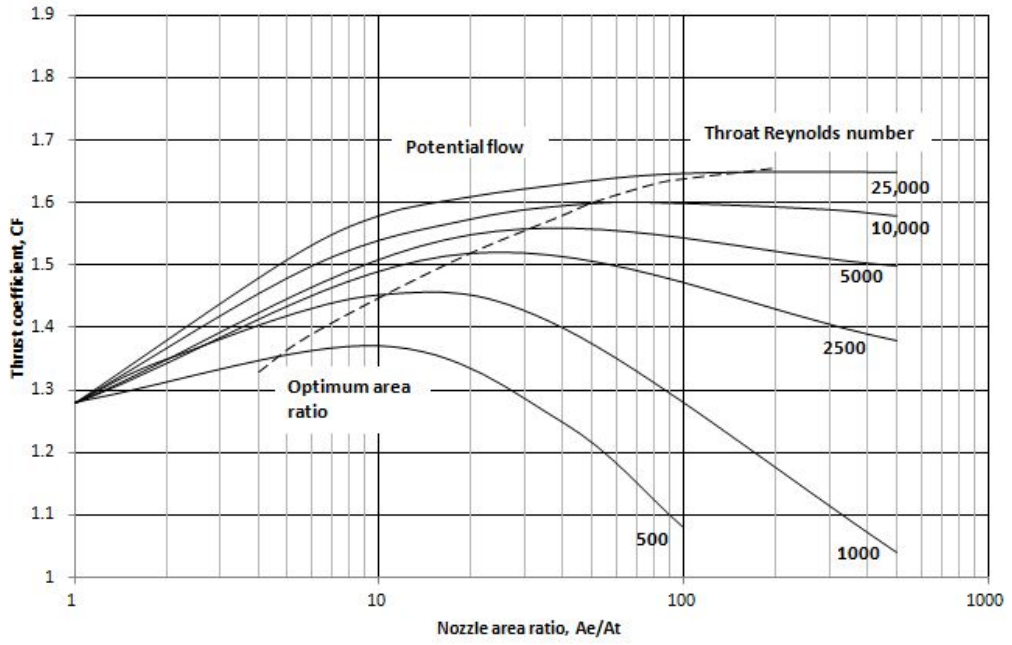

Figure 32. Thrust coefficient vs. expansion ratio for different Reynolds numbers [26].

3.5 Nozzle Designs

In order to improve the current HYDROS^{TM} thruster nozzle design, it is important to first observe the design of the factory nozzle. This nozzle is shown in Figure (33). The original design is a bell nozzle with an expansion ratio, $\epsilon = 266$. The expansion

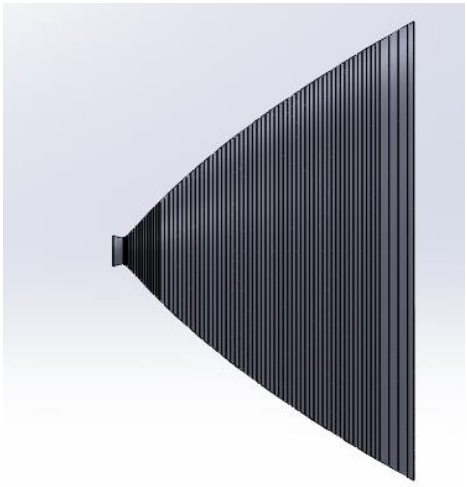

Figure 33. CAD model of the factory nozzle

angle, α, is approximately 37 degrees. This nozzle is over-expanded at sea level and has a high expansion ratio with a short length of 0.59 in. Based on the nozzle length and expansion ratio, this design did not follow the nominal method of characteristics (MOC) design for a bell nozzle, and has an excessive required turning angle just downstream of the throat, resulting in separated flow.

The idea for the first nozzle design is to keep the original factory nozzle length. Keeping the original length allows the nozzle not to extend beyond the 1U configuration. This 15-degree conical nozzle was chosen because of its simplicity in design and ease of fabrication. Using the two-dimensional conical nozzle geometry from Huzel and Huang, a new expansion ratio was calculated using the existing length [6].

Eq. (60) needs rearrangement to obtain an equation in terms of ϵ shown in Eq. (67)

$$\epsilon = \left(\frac{Ltan(\theta) + R_n(sec(\theta) - 1)}{r_t} + 1 \right)^2 \tag{67}$$

where L is the nozzle length in inches, r_t is the throat radius in inches, R_n is the circular contour arc radius of the throat in inches, and θ is the expansion angle, which is 15-degrees. To find R_n, Eq. (68) is used [6].

$$R_n = 0.382 r_t \tag{68}$$

The throat radius is 0.0246 in. and R_n is 0.0094 in. The expansion ratio becomes 55 per Eq. (67). The geometry of the conical nozzle is shown in Figure 34. The

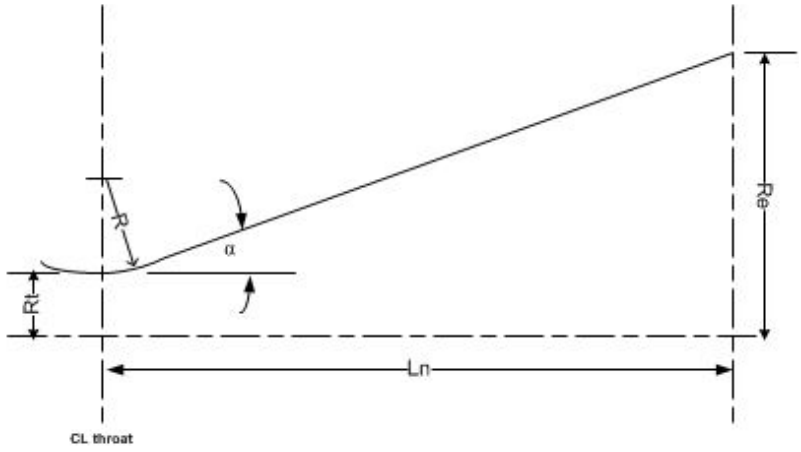

Figure 34. Nozzle contour of the conical nozzle [6].

nozzle was designed using commercial CAD software and manufactured at the AFIT machine shop. Both the CAD and manufactured models are shown in Figure 35. The material of the nozzle is aluminum 6061.

Using Eq. (57)-Eq. (66), the maximum thrust, coefficient of thrust, and I_{sp} are obtainable. These values will be used to compare with the experimental values to observe the performance loss and efficiency of the nozzle. These values disregard

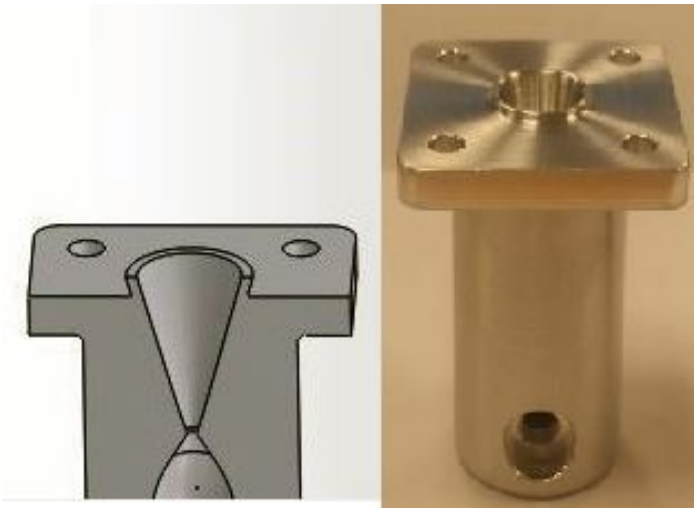

Figure 35. CAD and manufactured model for nozzle 1.

viscous losses in the nozzle area. Using an area ratio of 55 and k of 1.3, with Eq. (57), the Mach number at the exit was calculated. Using this Mach number with Eq. (63)-Eq. (62), P_2 was determined. Then, the coefficient of thrust was calculated using Eq. (61). After finding C_F, I_{sp} and T were calculated using Eq. (65) and Eq. (66). The results of the calculations are shown in Table 2.

The second design is also a conical nozzle. This design kept the original factory expansion ratio and evaluated the length required with a 15-degree expansion angle. Using Eq. (60), the second nozzle length was determined. With a 266 expansion ratio, the new length was 1.407 in. Using the contour shown in Figure 34 with the new nozzle length, the design was created using CAD. Due to the length, nozzle 2 is extended outside of the 1U configuration. Figure 36 shows the CAD and manufactured model of nozzle 2. In order to calculate the ideal coefficient of thrust, I_{sp} and thrust, the same procedures from nozzle 1 calculations were repeated with nozzle 2 expansion ratio. The results are shown in Table 2.

The purpose of the third nozzle is to evaluate a more optimal expansion ratio for this system. Based on Spisz *et al.*'s research discussed previously [26], an expansion ratio of 22 was chosen to match the optimum area ratio for the calculated Reynolds

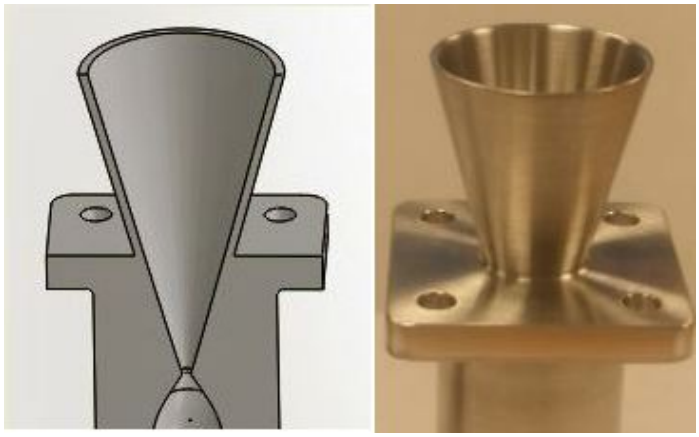

Figure 36. CAD and manufactured model for nozzle 2.

number. This nozzle is expected to show a small improvement in I_{sp} when compared to nozzle 1 ($\epsilon = 55$). The CAD model and manufactured model are displayed in Figure (37). The outcome of this data can help determine if Spisz *et al*'s. research for low Reynolds number systems can also be applied to systems with short firing duration.

Figure 37. CAD and manufactured model for nozzle 3.

The ideal coefficient of thrust,thrust, and I_{sp} for this nozzle were calculated using Eq. (57)- Eq. (66) and shown in Table 2. A summmary of the expansion ratio for the

Table 2. Optimal conditions for the three nozzle designs.

Nozzle	k	P_2(Pa)	C_F	$T(N)$	I_{sp}(sec)
1	1.3	2 x 10^{-7}	1.814	0.614	337
2	1.3	2.4 x 10^{-8}	1.873	0.634	348
3	1.3	9.6 x 10^{-7}	1.761	0.596	327

four nozzles is indicated in Table 14 and a comparison of all four nozzle contours is shown in Figure 52.

Table 3. A summary of expansion ratios.

	Original	1	2	3
ϵ	266	55	266	22

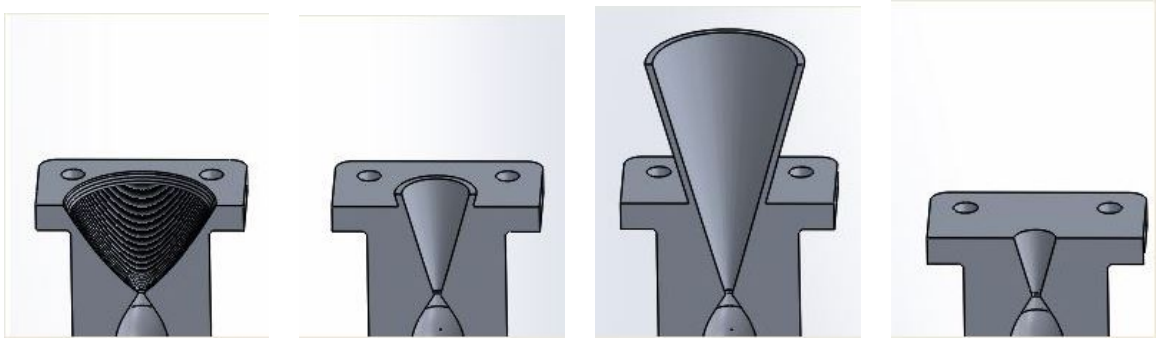

(a) Original Nozzle. (b) Design 1. (c) Design 2. (d) Design 3.

Figure 38. Nozzles comparison of the 4 nozzles [15].

3.6 Error analysis

The performance criterion discussed in Chapter 4 include impulse bit, specific impulse, and thrust coefficient. Impulse bit measurement variations were calculated using standard error. The standard error was calculated using the Eq. (69),

$$SE_{\bar{x}} = \frac{S}{\sqrt{n}} \tag{69}$$

where S is the standard deviation and n is the sample size. Using this standard error, the impulse bit error was calculated using Eq. (70),

$$\frac{\sigma_{I_{bit}}}{I_{bit}} = \sqrt{\left(\frac{SE_{\bar{x}}}{displacement}\right)^2} \tag{70}$$

where *displacement* is the displacement of the swinging arm in voltage. The equation for I_{bit} is shown in Eq. (74),

$$I_{bit} = \frac{displacement}{6.26} \tag{71}$$

where 6.26 is the calibration conversion number in V/N-s. For specific impulse, the total error propagation is shown in Eq. (72),

$$\frac{\sigma_{I_{sp}}}{I_{sp}} = \sqrt{\left(\frac{\sigma_{i_{bit}}}{i_{bit}}\right)^2 + \left(\frac{\sigma_{\Delta m}}{\Delta m}\right)^2} \tag{72}$$

where σ represents the error. Lastly, error propagation for C_F was calculated using Eq. (73). All error results are indicated in the data plots' error bars in Chapter 4.

$$\frac{\sigma_{C_F}}{C_F} = \sqrt{\left(\frac{\sigma_{I_{sp}}}{I_{sp}}\right)^2} \tag{73}$$

IV. Results and Analysis

The experimental set-up discussed in Chapter 3 was used to determine the performance of the HYDROS^{TM} thruster. Experimental results and data analysis are presented in this chapter. The performance criteria for this research are impulse bit, specific impulse, thrust coefficient, and exhaust plume attachment. Further performance analyses are investigated through comparing the results between the experimental data, the theoretical data from CEA, and the research data from Spisz *et al.* Spisz *et al.* conducted research on the thrust coefficient for a low thrust, steady state, and low Reynolds number thruster. Their research analyzed the influence viscous effects have at different Reynolds numbers and expansion ratios. The experimental data from this research were used to compare with Spisz *et al.*'s data to investigate whether pulsed thrusters might display the same behavior identified in their research.

4.1 Thrust Stand Calibration Results

The thrust stand was originally calibrated by using a small calibration hammer located on the thrust stand. This calibration hammer was used for the original nozzle and nozzle 1. However, a different hammer was used to calibrate nozzle 2 and nozzle 3, due to a malfunction of the small hammer. The new hammer was not attached to the electrical connections of the thrust stand; therefore, calibrations were performed at atmospheric conditions instead of at vacuum. This research assumed calibration behavior in atmosphere is similar to that in vacuum. This assumption was possible because the main difference between calibrating at atmosphere and at vacuum is aerodynamic drag. Since the thrust stand experiences very little displacement, and has a very low natural frequency, due to the high moment of inertia of the system, the velocity of the thrust stand is approximately zero. Thus, there is minimal

aerodynamic drag.

Initially, calibrations for the thrust stand were performed before and after each test set and utilize this number for each individual test result. However, due to inconsistencies in calibration and the use of different hammers, an average calibration number was used for all test set results. Calibrating the thrust stand was difficult, because each calibration was slightly different from another. Chapter 3 described the calibration method. Figure 39 and Figure 40 show the damping ratio and the natural frequency for each calibration set using the new calibration hammer.

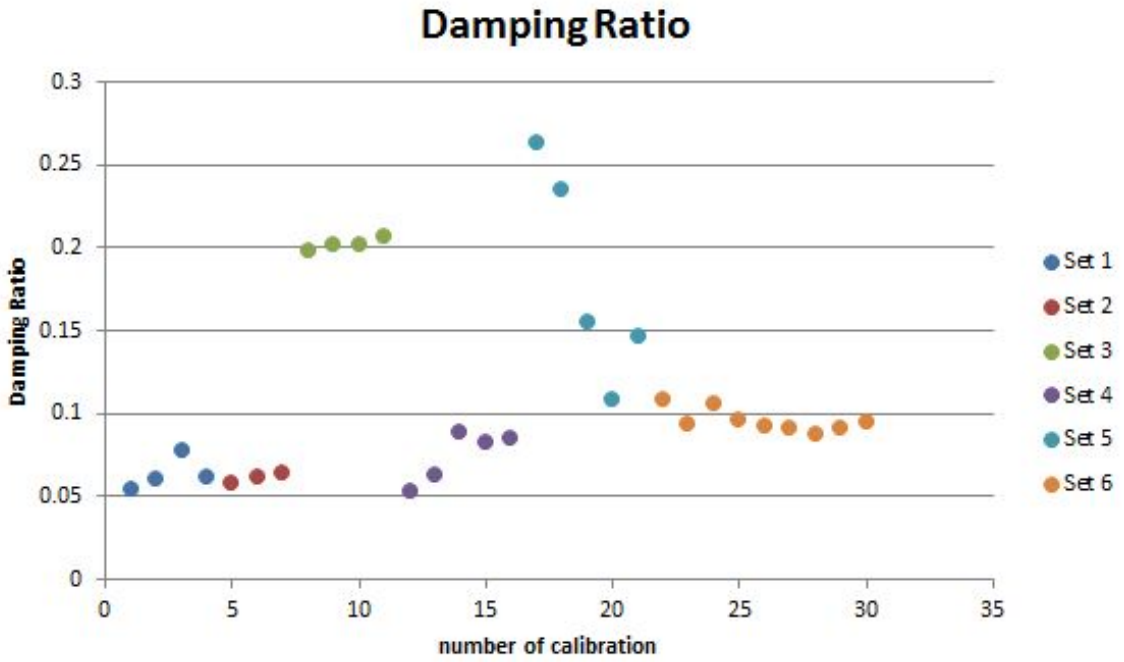

Figure 39. The damping ratios of the thrust stand.

For both plots, each color represents each test set. Both the natural frequency and the damping ratio were close in range within each test set. However, they changed slightly between each calibration set. As previously described in Chapter 3, the purpose for calibration is to find a voltage-to-impulse bit conversion for the thruster. This conversion number was obtained through dividing the original amplitude of the impulse response by the impulse bit of the hammer. Unfortunately, this unit

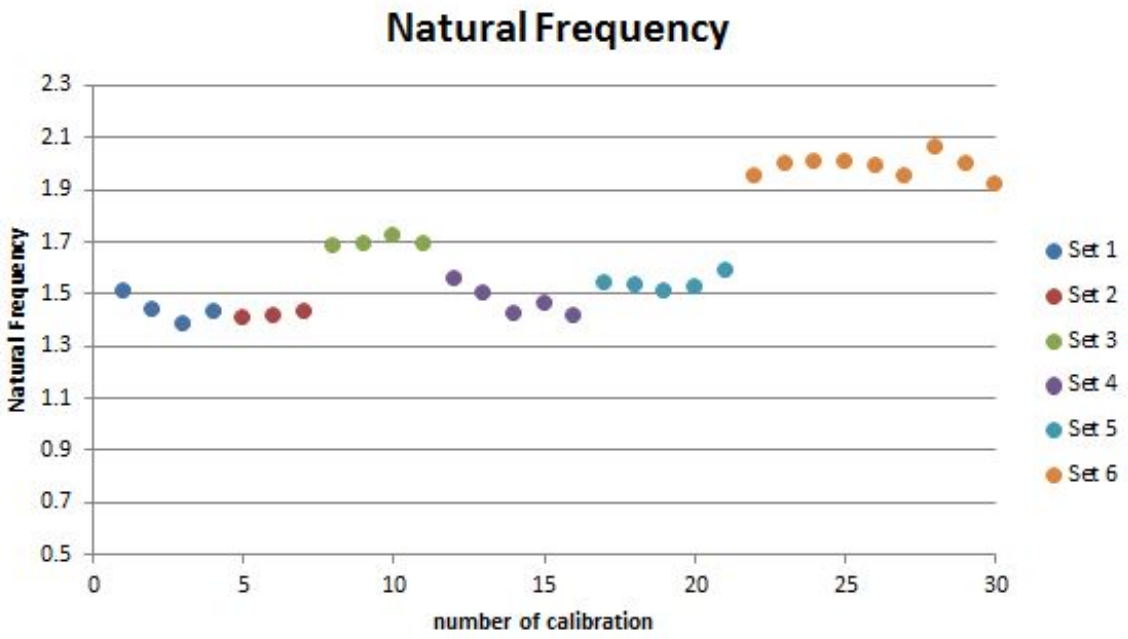

Figure 40. The natural frequencies of the thrust stand.

conversation number was different for each calibration strike. They ranged roughly between 5 to 10 Volts per V/N-S. Figure 41 shows the difference in each calibration.

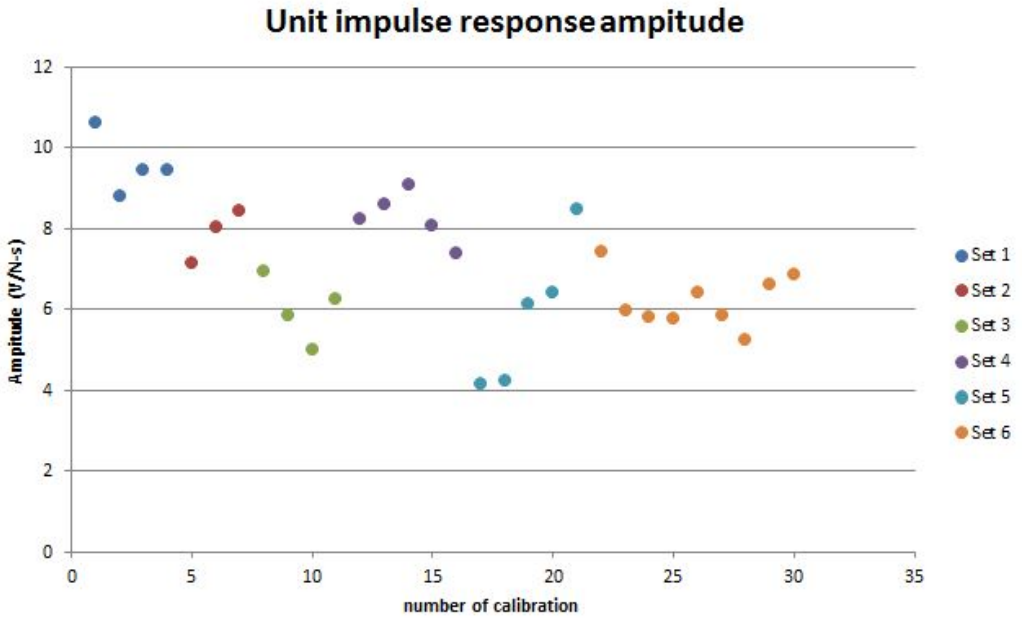

Figure 41. Unit impulse responses magnitude of the thrust stand.

The major inconsistency in calibration is uncertain because the calibration data were too far apart. This was not expected. For nozzle 2 calibrations, the hammer was struck approximately the same location as the small hammer. The distance ratio between the thruster and the hammer was 0.52. In order to eliminate the distance measurement and scaling error, the hammer strikes for the first two calibration sets for nozzle 3 were located at equal distances to the thruster. Therefore, the distance ratio between the thruster and the hammer was minimal. The last two calibration sets for nozzle 3 were applied directly onto the thruster. This was the same location where the thruster fires. It was assumed that the last two calibration sets were the most accurate to the thruster response.

Since a wide range of calibration data exists, taking an average over all the data would lead to inaccuracy. Therefore, the final unit conversion number was calculated using only the average of the last calibration set, where the hammer input was applied directly on the thruster. This method was chosen based on the assumption the thrust stand response is consistent through all tests. The thrust stand had the same stiffness during each test, and all the components, including the counterweights, had remained constant. The only factor different was the location of the wire cable connecting the thrust stand to the thruster and the slightly varying mass of the thruster due to propellant consumption. Since the thruster was the only item taken on and off the thrust stand between each test, the damping from the wires could cause a small deviation in the response. Figure 39 indicates the damping from the last calibration set was in the similar damping range as the other calibration sets.

Due to inconsistencies in calibration, this research has taken this error into account in the upcoming performance criteria calculations. Performance criteria calculation was based on the 6.26 V/N-S conversion number. Using a lower conversion number of 5/N-S will yield a 25% increase in impulse bit, specific impulse, and thrust coefficient.

Using a higher conversion number of 10 V/N-S will yield a 37% decrease in impulse bit, specific impulse, and thrust coefficient.

4.2 Performance Analysis

This research consisted of testing the original nozzle and the three additional nozzles at plenum pressure of 30 psia, 40 psia, and 45 psia at 3 x 10^{-4} torr. Table 4 displays the test conditions for this research. Test 1 through Test 10 were completed while Test 11 and Test 12 were not completed due to malfunction of the thruster. Each test consisted of 9 to 12 firings. The thruster was weighed before and after each

Table 4. Test conditions for the HYDROS^{TM} thruster.

Original Nozzle		**Test 1**	**Test 2**	**Test 3**
$\epsilon = 266$	P1 (psia)	30	40	45
	Pa (torr)	3 x 10^{-4}	3 x 10^{-4}	3 x 10^{-4}
Nozzle 1		**Test 4**	**Test 5**	**Test 6**
$\epsilon = 55$	P1 (psia)	30	40	45
	Pa (torr)	3 x 10^{-4}	3 x 10^{-4}	3 x 10^{-4}
Nozzle 2		**Test 7**	**Test 8**	**Test 9**
$\epsilon = 266$	P1 (psia)	30	40	45
	Pa (torr)	3 x 10^{-4}	3 x 10^{-4}	3 x 10^{-4}
Nozzle 3		**Test 10**	**Test 11**	**Test 12**
$\epsilon = 22$	P1 (psia)	30	40	45
	Pa (torr)	3 x 10^{-4}	3 x 10^{-4}	3 x 10^{-4}

test to determine the mass change. Three assumptions were applied to the tests: first, the moment of inertia of the thrust stand remained constant throughout all test sets due to only a small mass change in propellant; secondly, the manufacturing tolerance in throat area was small and negligible; lastly, it was assumed nozzle contours had no affect on the water electrolysis process or on combustion; therefore, mass-per-fire for each plenum pressure was the same for all nozzle designs.

4.2.1 Impulse Bit.

Figure 42 illustrates the average impulse bit data of the four nozzles at various plenum pressures. The error bars show the standard error of each test set. Error

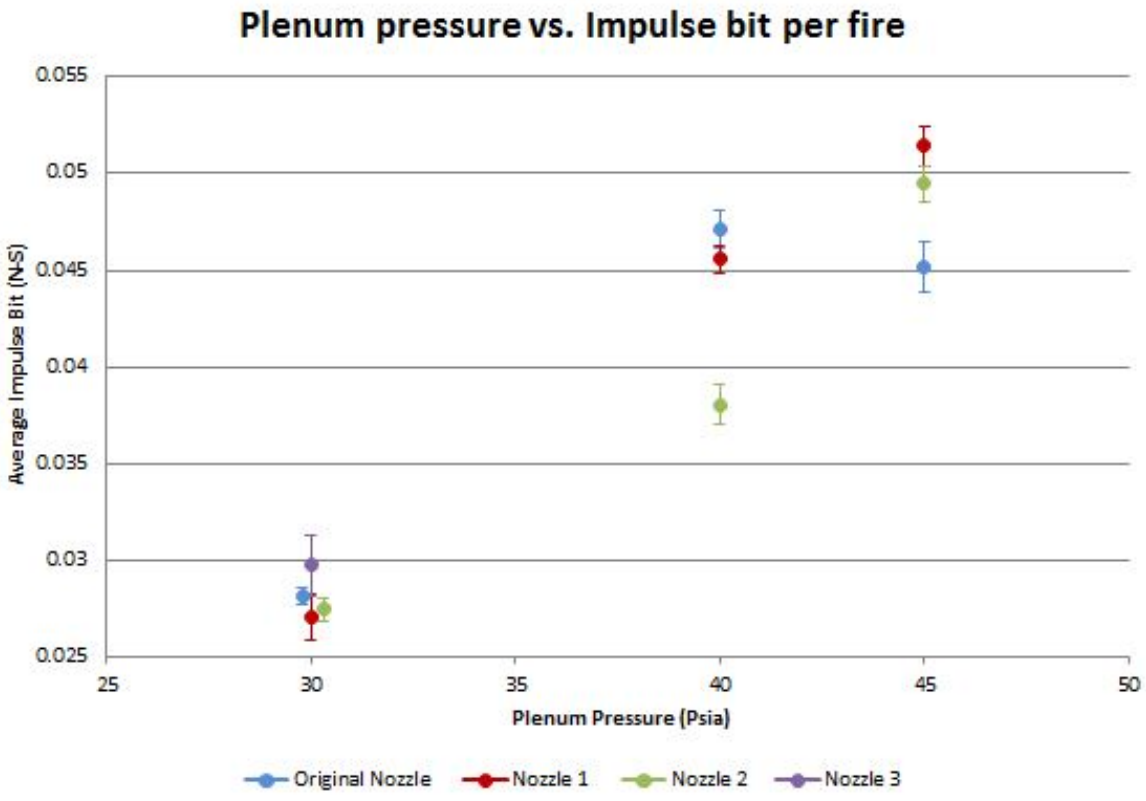

Figure 42. Impulse bit data of the four nozzles.

method was analyzed in Chapter 3. The equation for I_{bit} is shown in Eq. (74),

$$I_{bit} = \frac{displacement}{6.26} \tag{74}$$

where 6.26 is the calibration conversion number in V/N-S. All the raw impulse bit data are located in Appendix A.

Figure 42 indicates as pressure increases, the impulse bit also increases. This is expected because pressure is related to Reynolds number. An increase in Reynolds number would increase the thrust coefficient. Since thrust is directly related to chamber pressure and thrust coefficient, then chamber pressure also has a direct impact on impulse bit. The higher pressure correlates to an increase in the mass expended. As mass flow went up, the thrust coefficient also went up. Spisz *et al.*'s research had also shown as Reynolds number increases, performance also increases [26].

The original nozzle, indicated in blue, did not follow this behavior. There is an impulse bit drop between 40 and 45 psia. This drop was not expected. The original nozzle data were inconclusive due to the separation of the nozzle flow. The images of this separation are showed in the exhaust plume attachments section. In order to provide a better understanding of the original nozzle, more data points at 40 and 45 psia are required.

Viscous effect varies depending on the Reynolds number range. For this research, there is no accurate way to measure the Reynolds number and mass flow rate for each pressure. Therefore, estimations were made using the ideal conditions from CEA. The chamber pressures were unknown, because chamber pressure could decrease due to pressure drop in the injector, or increase due to periods of combustion which are closer to constant volume rather than constant pressure. Due to this reason, the Reynolds number and mass flow rate calculations were based on the plenum pressure. Although the Reynolds number changed as the nozzle expanded and mass flow rate

decreased, the estimations were made at the throat. These Reynolds numbers were used to compare with Spisz *et al.*'s research, since their data were correlated in terms of throat Reynolds number as well. Table 5 shows the CEA estimated Reynolds number and mass flow rate for each pressure at the throat. Chamber pressure changes during the pulse, it drops as the mass is expended. The average pulse duration was

Table 5. The estimated throat conditions.

Pressure (psia)	$\dot{m}$ (kg/s)	**Re**
30	1.21 x 10^{-4}	1243
40	1.61 x 10^{-4}	1636
45	1.81 x 10^{-4}	1831

approximately in the range between 0.2 to 1 second. Using this range with the mass per fire measured from experiment, the actual mean mass flow was on the order of 10^{-5}; this means the actual Reynolds numbers were expected to have a lower value than the CEA Reynolds numbers. In addition, CEA calculations were based on steady state operation. Due to the pulsed nature of the thruster, the Reynolds numbers were lower than calculated, however, the exact range is unknown.

By comparing nozzle 1 and nozzle 2, nozzle 1 with a 55 expansion ratio has a higher impulse bit than nozzle 2 with a 266 expansion ratio at 40 psia. The results at 40 psia corresponded with the Spisz *et al.*'s low Reynolds number research. Their research indicated for low Reynolds numbers (below 10,000), the benefit of having a larger expansion ratio might not exceed the increase in viscous effects, due to the added surface area [26]. By observing Figure 42, this conclusion only held true at 40 psia and not at the lower (30 psia) and higher (45 psia) pressure.

At 30 psia plenum pressure, the data points for the nozzles were very close together. As shown in Table 5, from 45 psia to 30 psia, Reynolds number drops from

around 1800 to 1200 and possibly lower due to the pulse condition. Due to viscous effects dominating the flow at low Reynolds numbers, the data showed nozzle contour and expansion ratio have little influence on performance compared to the 40 and 45 Psia data points. Since data for nozzle 3 at 40 and 45 psia were not captured, it is difficult to conclude the behavior at those pressures. However, nozzle 3 performance at 30 psia was higher, and this could suggest a similar performance range to nozzle 1.

At 45 psia, nozzle 1 performance is slightly higher than nozzle 2, however, the same argument might not hold true at 45 psia due to the small overlap in error. There is a maximum impulse bit value this system could obtain. At 45 psia, the system is getting closer to this limit, thus, the nozzle contour has less effects on performance. The smaller expansion ratio has a closer performance with the higher expansion ratio at 45 psia compared to 40 psia. Another reason was because as Reynolds number increases, viscous effects also decreases. At 45 psia, the negative effects of having additional surface area for the nozzle 2 might began to decrease.

In conclusion, impulse bit increases with increasing plenum pressure because Reynolds numbers increases with pressure and there is an increase in gross mass with pressures. Original nozzle behavior was inconclusive due to early flow separation. More data would be required to draw further conclusions. Performance between nozzle 1 and nozzle 2 at the lower and higher pressures indicated this thruster could obtain a minimum and maximum impulse bit regardless of the expansion ratio of the nozzle. At 30 psia, the nozzle was dominated by viscous boundary layers. At 40 psia, nozzle 1 with the smaller expansion ratio and less surface area had a better performance than nozzle 2 due to less viscous effects. At 45 psia, different nozzles performance were closer together because the system was reaching its maximum value on the performance curve. Thrust coefficient goes up dramatically for the lower area

ratios, but it only rises up slightly as area ratios increase. Impulse bit is more dependent on chamber pressures than other factors, such as expansion ratios.

4.2.2 Specific Impulse.

Specific impulse, I_{sp}, is a way to measure the efficiency of the system. It is the impulse delivered per unit of propellant. It is derived from the impulse bit shown in Eq. (75),

$$I_{sp} = \frac{\sum I_{bit}}{\Delta m g_o} \tag{75}$$

where Δm is the change of mass in each test set. The specific impulse value could directly applied to a spacecraft to calculate delta V, which is important for space missions to determine the possible maneuvers. The raw data for specific impulse and thrust coefficient are located in Appendix B.

Figure 43 displays the specific impulse data of the four nozzles for this research. Specific impulse performance at 30 psia was similar to the impulse bit data. Nozzle 3 has a slightly higher average impulse bit compared to the rest of the nozzles. However, when looking at efficiency, nozzle 3 has performance similar to the other nozzles at 30 psia. The same trend was indicated in this specific impulse plot, where viscous effects dominate at the low Reynolds number. Nozzle contour and expansion ratio have a minor performance influence at 30 psia.

At 40 psia, nozzle 1 was expected to have a higher I_{sp} performance compared to nozzle 2 based on the impulse bit data. However, this behavior did not appear in the I_{sp} data due to a large error in measurement. If the I_{sp} error bars were as small as the impulse bit error bars, then the same trend would appear. Between 40 and 45 psia, there was also a slight drop in performance for nozzle 1, but this is insignificant because it was also within the measurmement errors. The data between 40 and 45 psia were not expected to be far apart because the difference in performance between

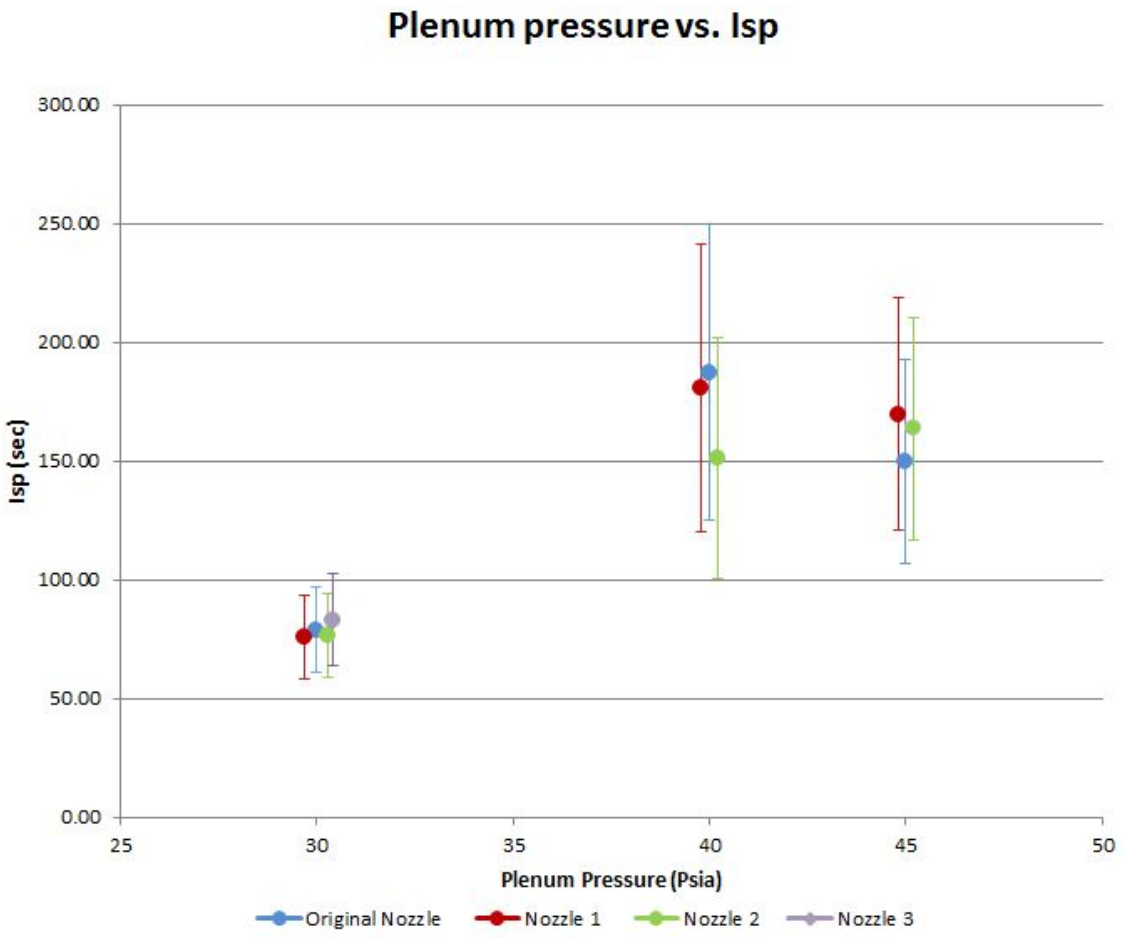

Figure 43. Specific impulse data for all four nozzles in various plenum pressures.

the various pressures are based on chemistry and geometry. Geometry was constant for each nozzle and chemistry is only changing slightly. At 30 psia, there was less heat release, which yielded a lower temperature and less complete combustion; but between 40 and 45 psia, chemistry was much closer.

As mentioned in the test set-up, mass was measured before and after each test set. The weight scale used was only capable of measuring up to 10^{-4} kg, and the mass of the thruster was also changing by 10^{-4} kg. This measurement error was included in the error bar. One of the initial assumptions for this experiment was the mass per fire at a given pressure was the same regardless of the nozzle contour, because nozzle

design should not affect the water electrolysis and combustion process. However, test data indicated differently for each nozzle design due to the mass measurement error. Therefore, in order to minimize this error, an average mass per fire for each plenum pressure was applied to all nozzle data. The average mass for each pressure was calculated using Eq. (76),

$$\text{Average mass per fire} = \frac{\sum_{i=1}^{4} \Delta m_i}{\sum_{i=1}^{4} n_i} \tag{76}$$

where 4 represents the sum of all four nozzle sets and n is the number of fire. The overall change of mass for I_{sp} calculation for each test set was calculated using Eq. (77),

$$\Delta m = \bar{m} n \tag{77}$$

where $\bar{m}$ is the average mass per fire.

Table 6. The average mass per fire for various plenum pressures.

Pressure (Psia)	Average mass per fire (kg)
30	3.65 x 10^{-5}
40	2.57 x 10^{-5}
45	3.09 x 10^{-5}

The average mass per fire for each pressure is shown in Table 6. As pressure increases, the mass required to fire should also increase. However, Table 6 does not indicate the same result due to the measurement error mentioned above. In order to obtain more accurate mass per fire data, more data points are required. In addition, the 30 psia tests were first performed after receiving the thruster back from nozzle

replacement. The first tests might consume more propellant when first run in vacuum. The mass data for this research is included in Appendix C.

In order to obtain a better understanding of what the mass per fire for the various pressures were, mass estimations were calculated using the ideal gas law. The ideal gas law is shown in Eq. (78),

$$m = \frac{PVM}{RT} \tag{78}$$

where m is mass, M is the molar mass of the gas, P is the pressure of the gas, V is the gas volume, R is the universal gas constant, and T is the temperature of the gas, which was assumed to be room temperature at 300 K. The mass values from ideal gas law are the expected values and the mass per fire was expected to vary linearly with plenum pressures. The equation was calculated separately at 30, 40, and 45 psia, for gaseous hydrogen and oxygen. Hydrogen and oxygen volume were based on the gas tanks volume, provided by TUI, which are 12.9 cm^3 and 6.6 cm^3, respectively. Figure 44 shows the updated mass per fire along with the experimental data. Figure 44 indicates at 40 and 45 psia, the average mass per fire measured were very close compared to the ideal gas law calculation. On the other hand, the measured average value at 30 psia was too high.

Figure 45 shows the expected I_{sp} trend with the mass corrections. The projected nozzle 3 data for 40 and 45 psia are also plotted to show a complete data set. Nozzle 3 was suggested to have the same or higher I_{sp} as nozzle 1, based on its behavior at 30 Psia. With the new mass distribution, the trend between 40 to 45 psia was improved. Even though, this trend is not as linear as expected, the drop of performance between 40 and 45 psia appeared with the original data, shown in Figure 43, was dissolved. In addition, the measured I_{sp} values at 30 psia jumped from the 75 second range to 140 second range by using the ideal gas law mass. This was a better representation on I_{sp} because performance at 30 psia should not have a 50% drop compared to 40

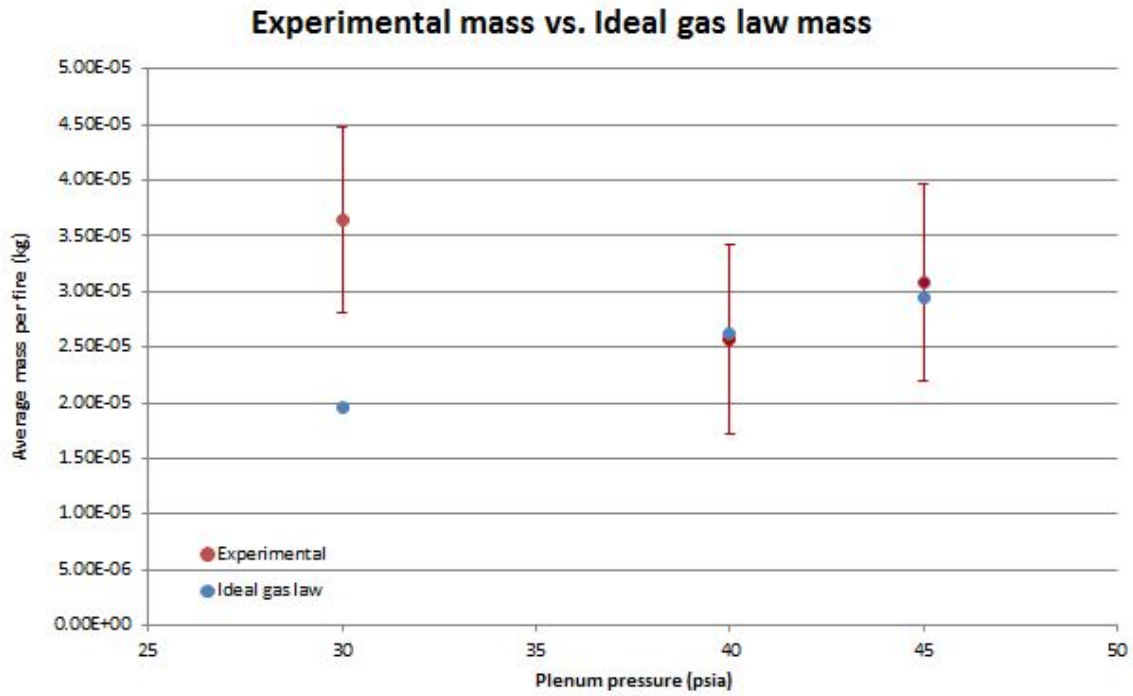

Figure 44. The comparison between the experimental average mass values and the ideal gas law mass values.

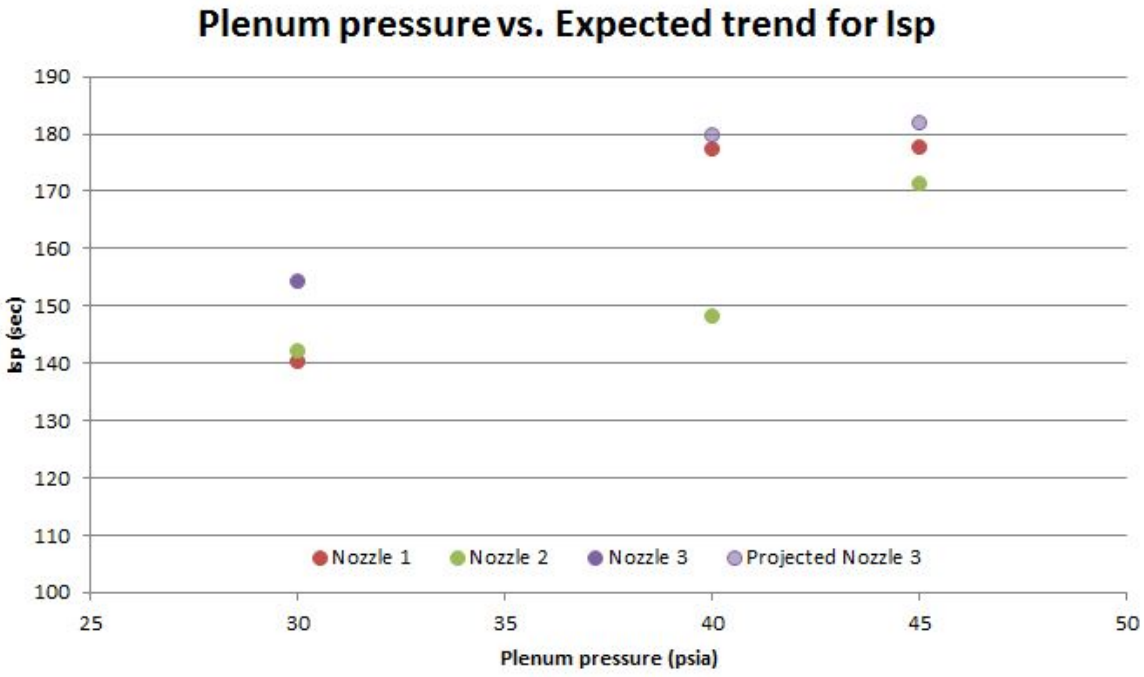

Figure 45. New Isp data with updated mass values.

psia, as shown in the measured values before mass corrections.

4.2.2.1 Specific Impulse Comparison.

In order to understand the performance of this thruster, it is important to compare the specific impulse to an expected range. Chapter 3 introduced the CEA calculated data. This was not the expected specific impulse because it was for an ideal, steady state, equilibrium combustion case. However, the CEA data was used as the base line case. In addition to the ideal case, viscous effects must be taken into account.

Spisz *et al.*'s research provided results on thrust coefficient loss due to viscous effects. This loss relationship could also applied to specific impulse because specific impulse is proportional to thrust coefficient shown in Eq. (79)[28].

$$C_F = \frac{I_{sp} g_o}{c^*} = \frac{F}{P_c A_t} \tag{79}$$

Since g_o is a constant and c^* is changing very slightly based on Figure 46. Figure 46 shows for chamber pressure between 30 to 45 psia, c^* in CEA is only changed by 0.5%. The second column of Table 7 indicates the ideal CEA data. The third column is the I_{sp} after accounting for the viscous effects based on Spisz *et al.*'s data. The viscous effect is approximately a 10-20% drop from ideal. Potentially, a greater losses in viscous effects can exist because the Reynolds numbers used were the ideal case. The actual Reynnolds numbers could have been significantly lower, increasing the losses.

There were greater viscous losses for a higher expansion ratio due to the increased surface area and also for decreasing Reynolds number. The solid lines in Figure 47 indicate the loss percentage in specific impulse based on Spisz *et al.*, and the dashed lines indicate the data from this experiment with the mass adjustment from ideal gas law. This figure showed the data from this experiment correlated with the viscous

Table 7. I_{sp} **(sec) data comparison between the measured values and the expected values.**

30 Psia	**Ideal data from CEA**	**Drop due to viscous effects (10-20%)**	**Drop due to pulse condition (30-40%)**	**Experimental measured values**	**Updated values with estimated mass**
$\epsilon = 22$	382	339	203	83	154
$\epsilon = 55$	396	336	202	76	140
$\epsilon = 266$	412	309	185	77	142
40 Psia	**Ideal data from CEA**	**Drop due to viscous effects (10-20%)**	**Drop due to pulse condition (30-40%)**	**Experimental measured values**	**Updated values with estimated mass**
$\epsilon = 22$	384	347	208		
$\epsilon = 55$	398	347	208	181	177
$\epsilon = 266$	414	324	194	151	148
45 Psia	**Ideal data from CEA**	**Drop due to viscous effects (10-20%)**	**Drop due to pulse condition (30-40%)**	**Experimental measured values**	**Updated values with estimated mass**
$\epsilon = 22$	385	351	211		
$\epsilon = 55$	399	352	211	170	178
$\epsilon = 266$	415	335	201	163	171

effects trend in Spisz *et al.*'s research. This figure also showed there was almost twice the viscous losses in the experimental data compared to Spisz *et al.* Part of the difference included pulse operation and measurement errors.

The fourth column of Table 7 is the estimated I_{sp} drop from steady state to pulse operation. Based on the historical monopropellant thruster data, there was an approximately 30 to 40% I_{sp} drop from operating in steady state to pulse operation [31]. Since the HYDROS^{TM} thruster is a pulsed thruster, following this pattern, a 30

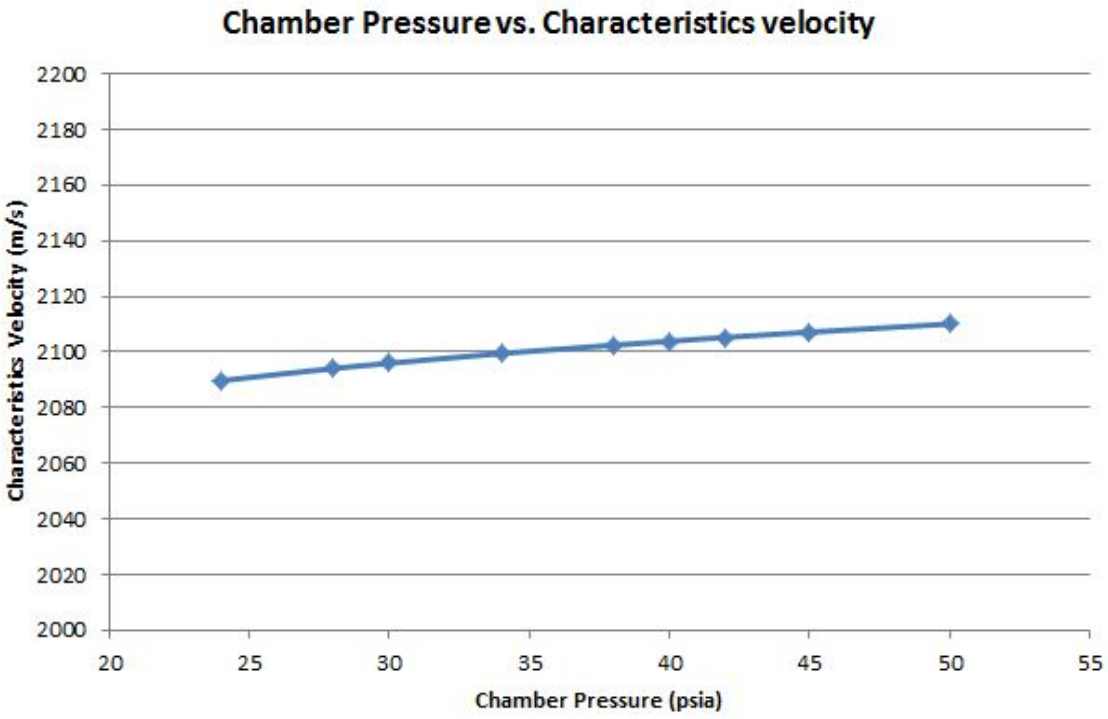

Figure 46. Characteristics velocity values in CEA.

to 40% drop in I_{sp} was expected as well and potentially more. Potential performance losses might exist due to the chamber pressure rising and then falling as the tank empties. Therefore, the I_{sp} number in Column 4 is the expected I_{sp} range, after taking viscous effects and pulse operation into account. Column 5 illustrates the measured I_{sp} values from this research. The measured values were lower than the expected values. The differences could be attributed to incomplete combustion leading to reduced c^*, error from mass measurement, and error from thrust stand calibration. The last column shows the I_{sp} value using the adjusted ideal gas law's mass for comparison. At 30 psia, there is a gain in I_{sp} due to the decrease in mass expended. This is a better representation of what happened because performance between the various pressures is expected to be within a close range from each other, similar to the ideal CEA data. The CEA data from column 2 showed a small change in I_{sp} between each pressure.

The percentage difference between the expected I_{sp} and the measured I_{sp} is shown

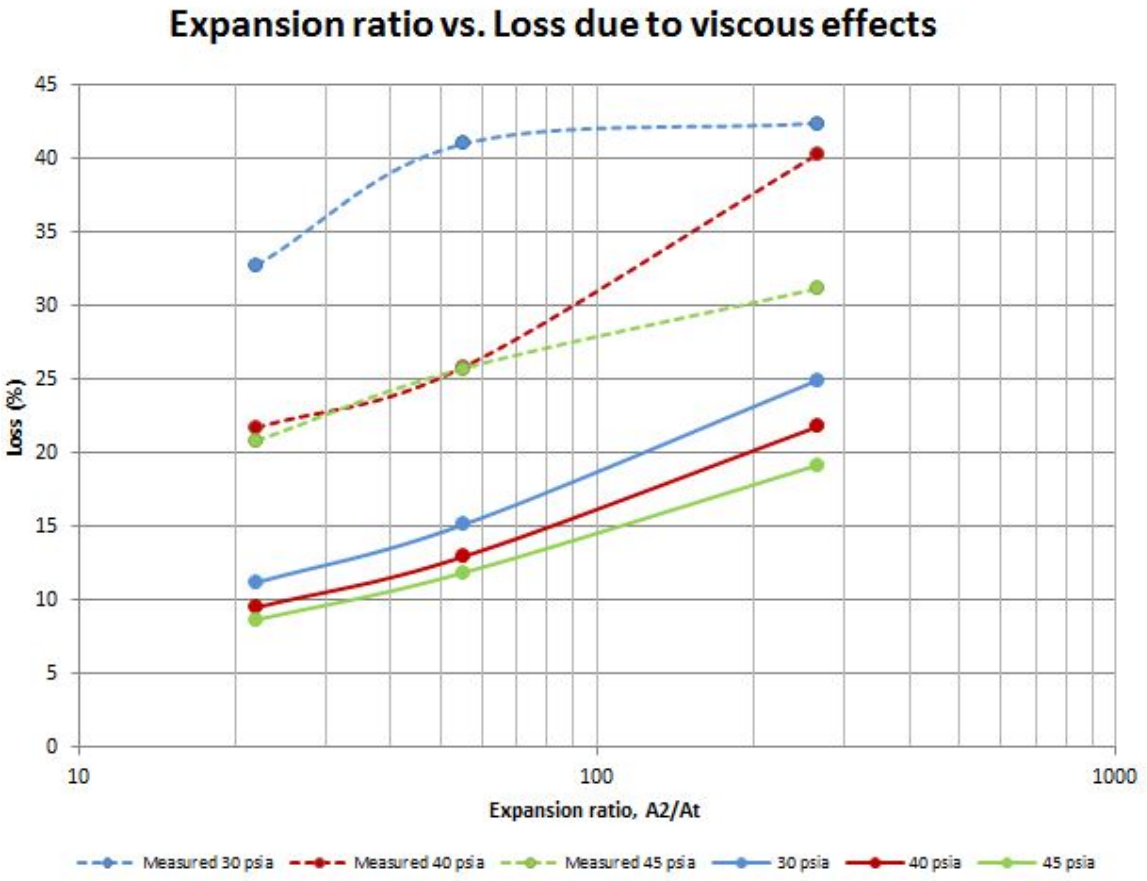

Figure 47. Loss percentage in specific impulse and thrust coefficient based on Spisz *et al.*

in Figure 48. The expected values in Figure 48 had taken both viscous effects and pulse condition into account. The percentage drop between the experimental values and the expected values, as well as the percentage drop between the new estimated values using the ideal gas law mass and the expected values, were both showed in Figure 48. Before the mass adjustment, there was an approximately 60% drop in performance at 30 psia. This loss percentage got reduced down to about 25% with the new mass. The loss percentage for both cases were similar at 40 and 45 psia, as well as at the different expansion ratios. They were all between 15-25%. The purpose of Figure 48 is to show what the difference is between the expected values from previous research, which included viscous effects losses from a steady-state operation

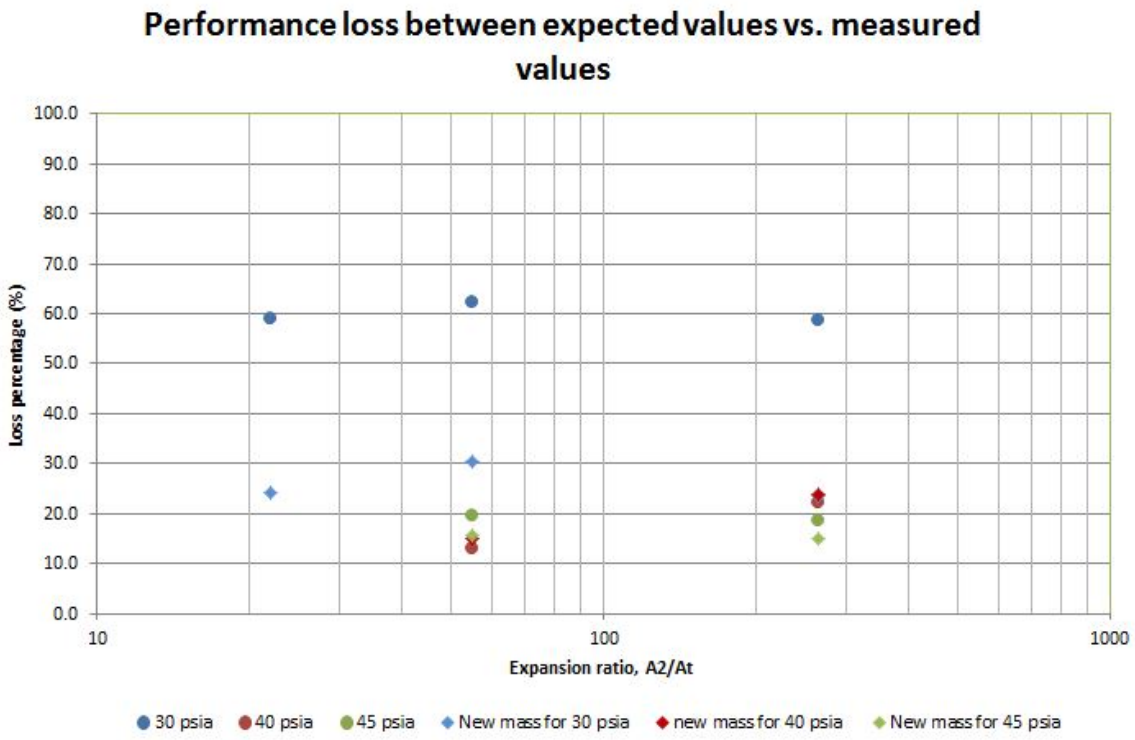

Figure 48. Loss percentage in performance between the expected values and the measured values.

studies and pulse condition losses from larger scale thrusters, to the measured values for a small scale pulsed chemical thruster.

Another important relationship to look at is the overall losses starting from the ideal CEA values all the way down to the measured values. The percentage of the overall losses is shown in Figure 49. The dotted lines in Figure 49 were the ideal losses, which only included the 10-20% drop from viscous effects and 40% drop from pulse operation. The lines showed there were greater losses with increasing expansion ratio and increasing pressure. The loss differences between various pressures were minimal, only a few percentage drop from each one another. At 30 psia, loss percentage dropped from about 80% down to about 65% with the new mass adjustment. The data at 40 and 45 psia followed similar results as the ideal losses. Looking at performance losses, there were higher overall losses and viscous losses with the increase in expansion ratio.

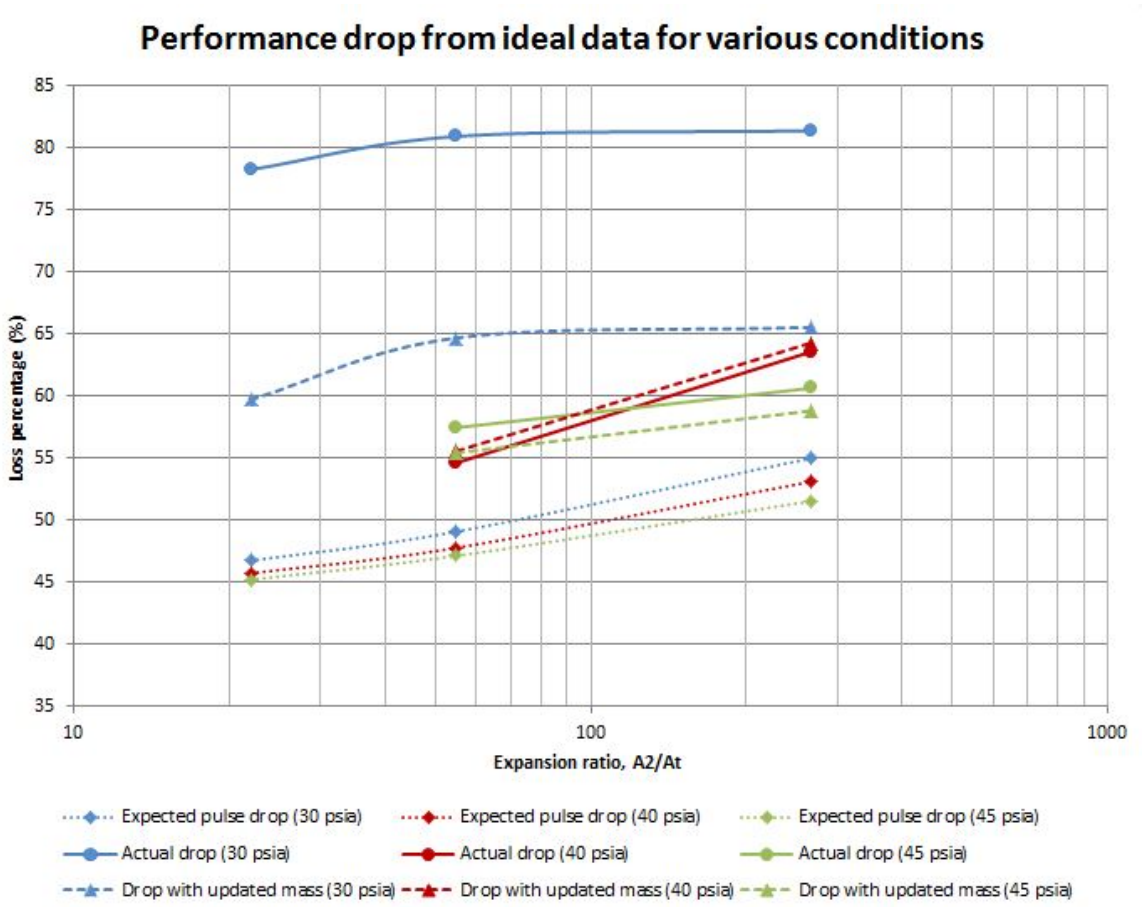

Figure 49. Overall loss percentage in performance between the ideal values and the measured values.

In conclusion, following the I_{bit} results, at 30 psia, viscous effects dominate and the nozzle contour and expansion ratio had insignificant influence in performance. For each nozzle, data between 40 and 45 psia was expected to have similar performance. At 40 psia, nozzle 1 should have a higher performance compared to nozzle 2, however, due to mass measurement error, nozzle 1 did not show an improvement compared to nozzle 2. There was not much increase in losses at the higher pressure. Overall, there was about a 15-20% additional losses apart from the viscous effects based on Spisz *et al.* and the 40% drop from pulse condition. The additional losses might come from additional viscous losses due to a lower Reynolds number than estimated, as well as measurement error and calibration error.

4.2.3 Thrust Coefficient.

Thrust coefficient, C_F, is another way to look at the efficiency of the system. Since the thrust of this system is unknown, the thrust coefficient data were calculated using specific impulse showed in Eq. (79). Figure 50 displayed the thrust coefficient result

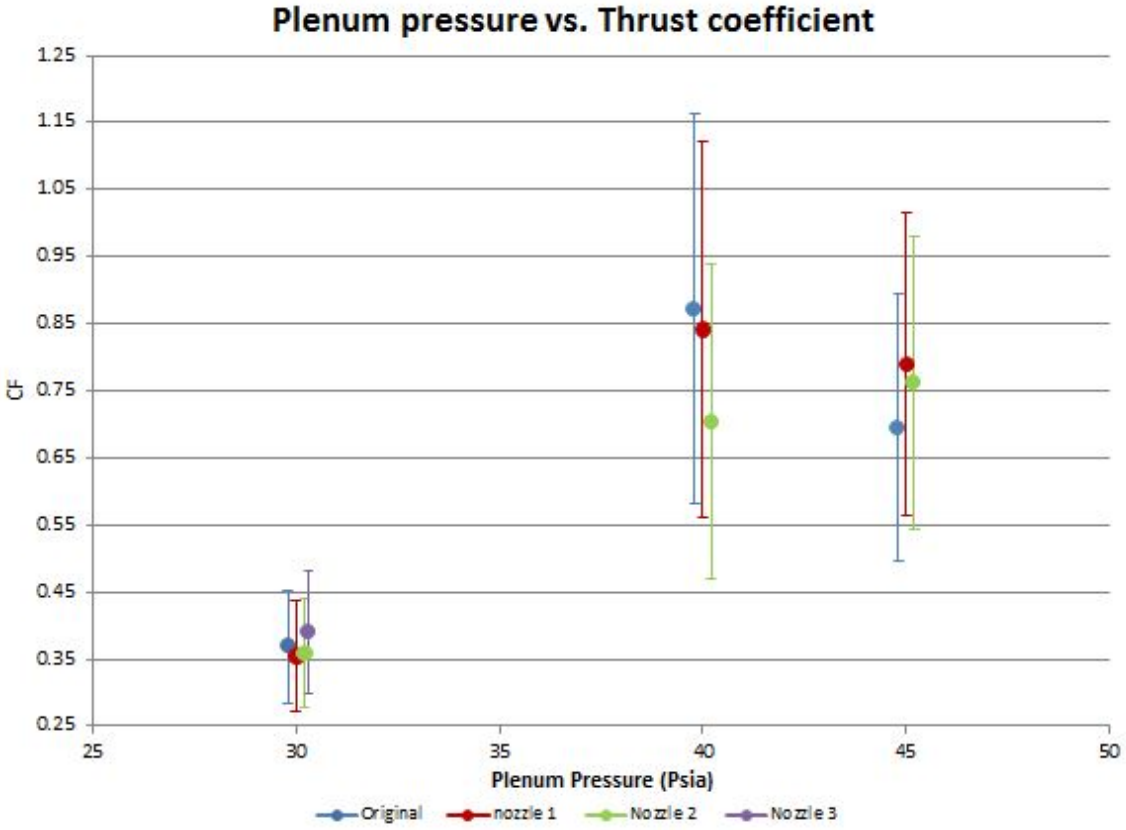

Figure 50. The thrust coefficient data of the four nozzles at various plenum pressure.

of the four nozzles at various plenum pressures. The data trend between thrust coefficient and specific impulse are similar because they are related to one another. The two are not directly proportional due to the small change in c^*. At 30 psia, all four nozzles have similar performance, because viscous effects dominate in low Reynolds number flows. Between 40 and 45 psia, nozzle 1, with a smaller expansion ratio ($\epsilon = 55$), has a slightly higher performance in C_F than nozzle 2 ($\epsilon = 266$) without taking error into account. However, taking into account of the error bars, the two

nozzles were indicated to have a similar performance. Data at 40 psia also displayed similar trends to 45 psia.

As previously explained, performance between the various pressures should not have a significant difference. However, comparing the data between 30 psia and 40 psia in Figure 50, it showed an approximately 50% drop in thrust coefficent. This was mainly caused by the high average mass per fire at 30 psia. Using the ideal gas law mass calculated earlier, Figure 51 illustrates the expected thrust coefficient trend after the adjustments were made in mass per fire. The projected nozzle 3 data at 40

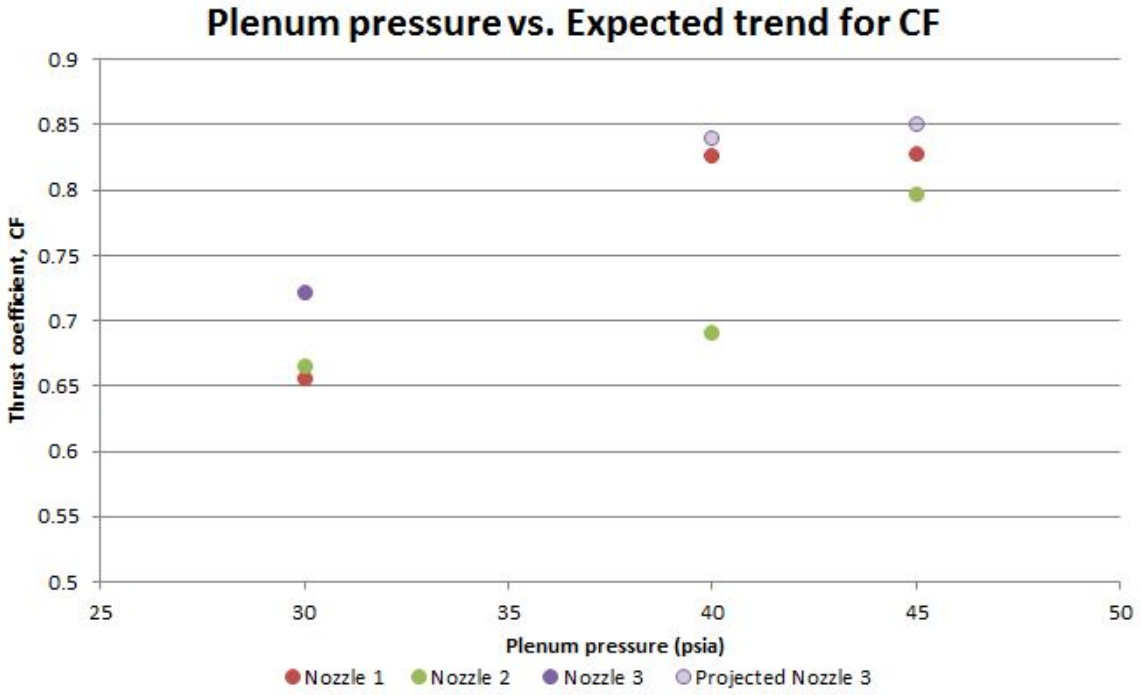

Figure 51. The updated thrust coefficient data with mass adjustment.

and 45 psia were also plotted for completeness. With this estimated mass, there was only a 20% drop in performance from 40 to 30 psia. The data for all three pressures were much closer in range with the mass correction.

4.2.3.1 Thrust Coefficient Results Comparison.

Table 8 compares the expected thrust coefficient values with the measured values. The table is separated based on chamber pressure, which is directly proportional

Table 8. Thrust coefficent comparison between measured and expected thrust coefficient.

30 Psia	Ideal data from CEA	Drop due to viscous effects (10-20%)	Drop due to pulse condition (30-40%)	Experimental measured values	Updated values with estimated mass
22	1.79	1.59	0.95	0.39	0.72
55	1.85	1.57	0.94	0.35	0.66
266	1.92	1.44	0.87	0.36	0.67
40 Psia	**Ideal data from CEA**	**Drop due to viscous effects (10-20%)**	**Drop due to pulse condition (30-40%)**	**Experimental measured values**	**Updated values with estimated mass**
22	1.79	1.62	0.97		
55	1.86	1.62	0.97	0.84	0.83
266	1.93	1.51	0.90	0.70	0.69
45 Psia	**Ideal data from CEA**	**Drop due to viscous effects (10-20%)**	**Drop due to pulse condition (30-40%)**	**Experimental measured values**	**Updated values with estimated mass**
22	1.79	1.63	0.98		
55	1.86	1.64	0.98	0.79	0.83
266	1.93	1.56	0.94	0.76	0.80

to the estimated Reynolds number, and expansion ratio. The second column shows the ideal thrust coefficient values from CEA. CEA is the best case scenario, which ignores conditions such as incomplete combustion, pulse operation, and viscous effects. Using Spisz *et al.*'s loss due to viscous effects data, Column 3 shows the 10-20% drop

in thrust coefficient performance. There is a greater loss for the higher expansion ratio nozzles, as well as at lower pressure. Column 4 indicates the expected thrust coefficient after the 30 to 40% drop from steady state to pulse operation, largely due to a decrese in average pressure when compared to steady thrust profiles. Column 5 is the measured values. Compared to Column 4, Column 5 is lower, because there are additional losses due to incomplete combustion, mass measurement error, and thrust stand calibration error. There is a larger difference in 30 psia, because for the CEA ideal case, chamber pressure variation has low impact on the calculated C_F in vacuum as shown in Column 2. However, in the measured values, there was a close to 50% jump in performance between 30 and 40 psia due to mass measurement error. With the estimated mass from ideal gas law showed in column 6, the data between the different pressures were within 2-3% of each other, similar to the relationship in CEA data. The C_F values in Column 5 and Column 6 were the worse case values because the thrust coefficient calculations were based on an ideal c^* value. This c^* value would only decrease. And thrust coefficient increases with decreasing c^* for a fixed specific impulse value.

The viscous losses percentage and the overall losses percentage data between the expected and the measured values were the same as the data showed in Figure 48 and Figure 49, since I_{sp} and C_F are proportional with only a slight change in c^*.

Figure 52 compares the trend between Spisz *et al.* data and experimental data from this research. Spisz *et al.*'s data indicated the thrust coefficient data for steady state operation in terms of expansion ratio and Reynolds number. This data was for gamma = 1.4 expansion and for this research, gamma was closer to 1.3. The experimental thrust coefficient data in Figure 52 included the mass adjustment from ideal gas law and the projected nozzle 3 performance at 40 and 45 psia.

The two sets of data both showed a performance decrease with an increase in

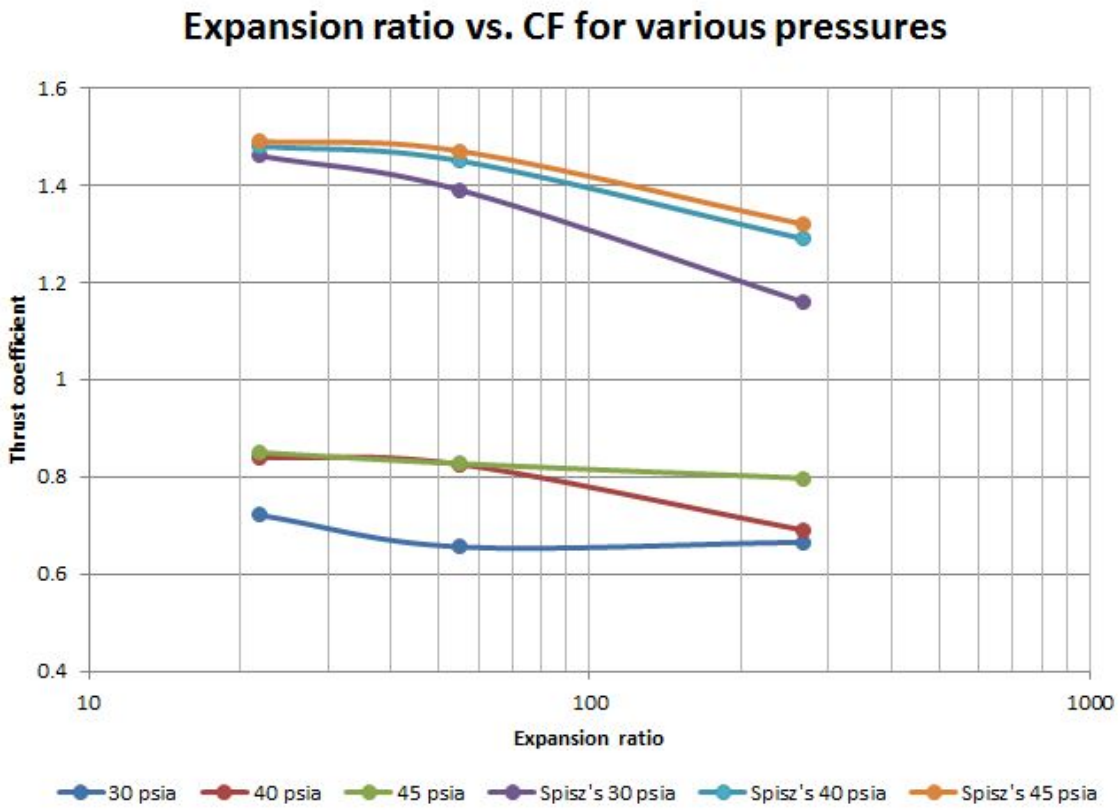

Figure 52. Thrust coefficient trend comparison with Spisz *et al.* research data.

expansion ratio and decrease in Reynolds number. However, the slopes of the curve were decreasing more sharply than for Spisz *et al.* data. The difference might come from the pulse condition of this thruster. Figure 52 showed at 30 psia, expansion ratio has less influence in performance and at 45 psia, the performance of the thruster was getting closer to the maximum values on the performance curve. Therefore, a decrease in expansion ratio did not provide a major improvement in performance compared to 40 psia because the performance curve was leveling off at the higher pressure. In addition, the data from Spisz *et al.* were based on different Reynolds numbers. The Reynolds numbers were chosen for comparison based on CEA calculations. The experimental data could have a lower and decreasing Reynolds number due to the decreasing mass flow caused by pulse operation. And Spisz *et al.*'s research Reynolds numbers were constant due to steady state operation. Therefore, at 30 psia, viscous

effects for experimental data were larger and expansion ratio became less significant compared to Spisz *et al* 30 psia data.

4.3 Exhaust Plume Attachments

Nozzle exit flow attachment is critical for system performance. Flow separation in the nozzle can reduce nozzle efficiency, thus decreasing system performance. In the summer of 2014, high speed images of the original factory nozzle exhaust were captured. These images are shown in Figure 53 [14]. The high speed images indicated there was flow separation with this bell nozzle. The exhaust flow is not attached to the nozzle wall. The efficiency of the system is decreased due to this separation, and new nozzle design is needed to improve system performance.

Nozzle 1 high speed images are showed in Figure 54. Nozzle 2 high speed images are shown in Figure 55, and nozzle 3 images are shown in Figure 56. The exhaust plume between the original nozzle and the new nozzles did not change much, but the new nozzles were shaped to better match the exhaust. Using the images, exhaust angles were calculated to quantify improvements. These were estimated angles because the measurements were only based on the images captured. The exhaust plume angles were roughly between 14 to 18-degree.

Based on the new nozzle images and the calculated angles, the exhaust plume aligned closer to the 15-degree nozzle contour compared to the 37-degree bell nozzle. Flow separation at the exit plane was difficult to measured. For the original nozzle, there was about a 5.6 mm separation distance. However, due to the similar angle between new nozzle contour and the exhaust plume, there were only minimal separation distance for the conical nozzles. These findings indicated changing the nozzle design to a 15-degree conical nozzle can help improve the flow separation problem, as well as help improve the nozzle efficiency. The fire duration for this thruster is unmeasurable

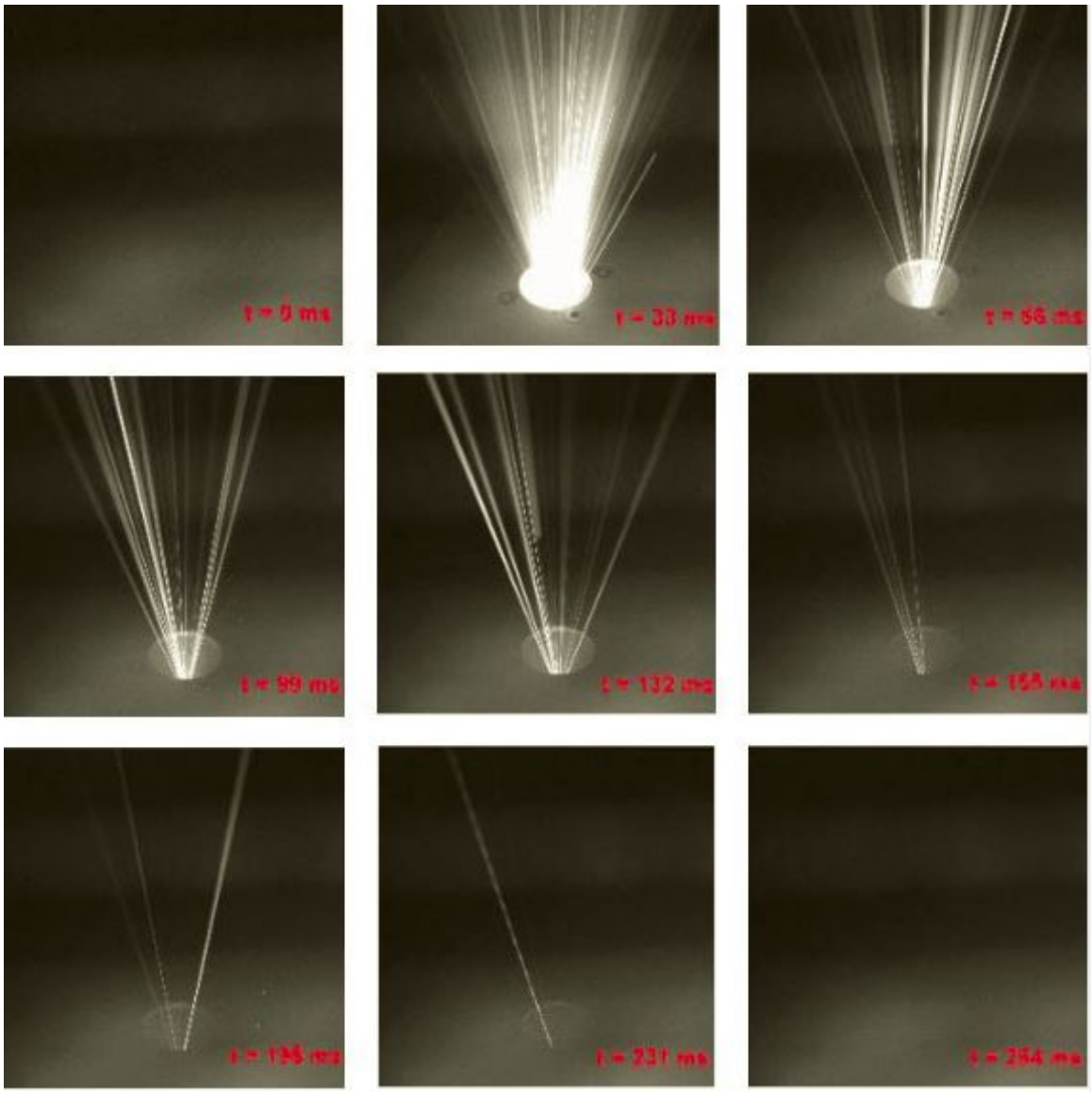

Figure 53. High speed images of factory nozzle: Exposure time of 264 ms (30 fps) [14].

by the means at hand. However, by observing the exposure time of the high speed images, the images showed an inconsistency in fire duration pattern. Based on the images, it can concluded the new nozzles helped to improve systems efficiency. This efficiency might not represented well in the I_{sp} and C_F data due to the large error in measurement.

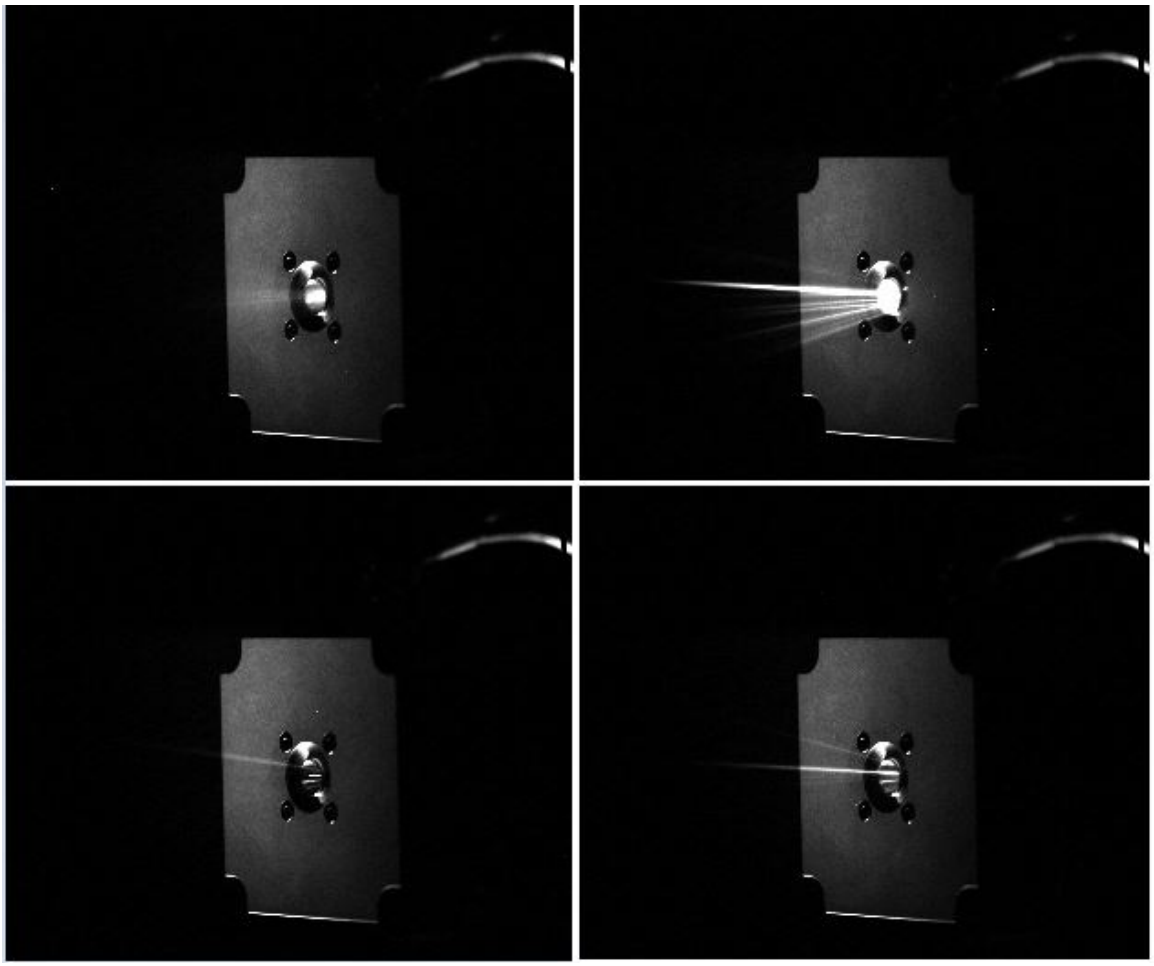

Figure 54. High speed images of Nozzle 1: Exposure time of 32 ms (125 fps).

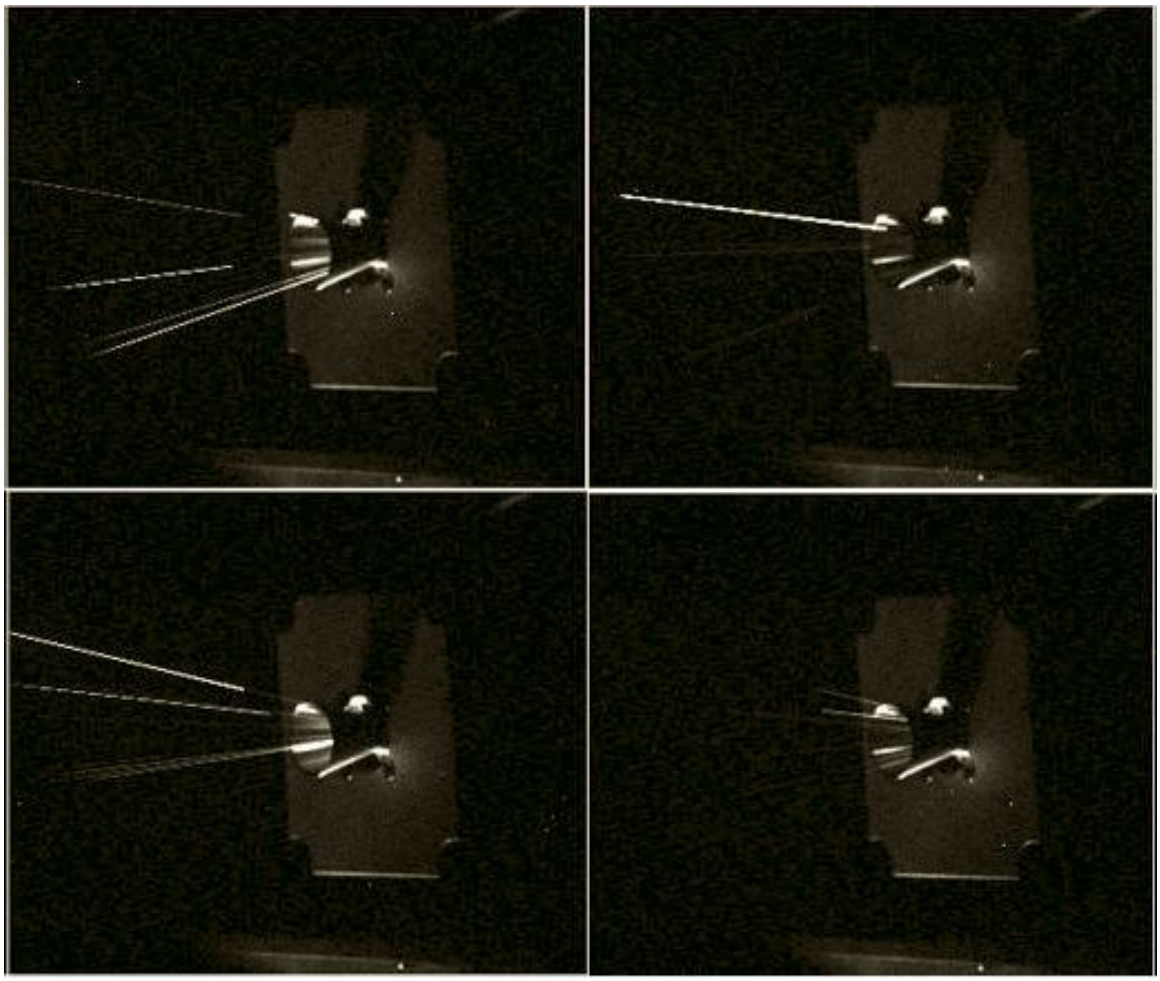

Figure 55. High speed images of Nozzle 2: Exposure time of 32 ms (125 fps).

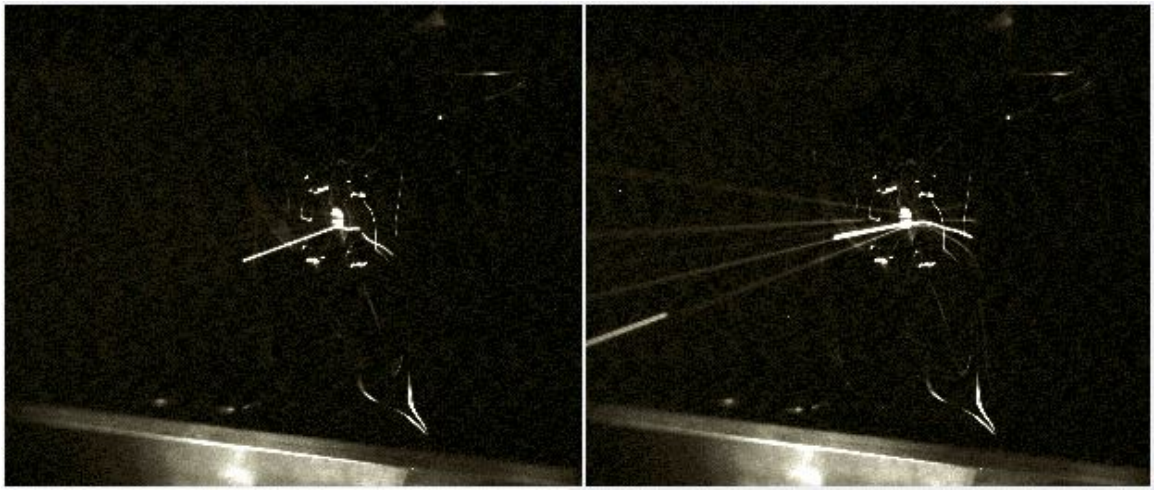

Figure 56. High speed images of Nozzle 3: Exposure time of 4 ms (500 fps).

V. Conclusions and Future Work

In chapter 1, a list of research objectives was established. These objectives served as the guidelines throughout this research. The goal for this research is to understand how different nozzle contours affect performance and efficiency in small pulsed chemical thrusters. Each objective leads the research closer to the research goal. This concluding chapter will review those objectives and evaluate if the research goal was met. In addition, this chapter will also summarize the result for this research, and recommendations for future work.

5.1 Research Objectives Review

The five research objectives are as follows:

1. Design nozzles using a nominal two-dimensional conical geometry to improve the specific impulse of the thruster and verify results by using the experimental impulse bit data to calculate specific impulse.

2. For each nozzle design, experimentally measure performance criteria such as impulse bits, thrust coefficient as a function of the plenum pressure envelope at 30, 40, and 45 psia, in vacuum using a torsional balance thrust stand.

3. Determine nozzle performance at various plenum pressures and expansion ratios by comparing thrust coefficient.

4. Examine viscous effects on nozzles by comparing experimental data with ideal CEA data and previous research data.

5. Determine nozzle efficiency improvement by comparing the exhaust flow attachment points relative to the nozzle using images from a high-speed camera.

A total of 10 test sets were conducted at 3 x 10^{-4} Torr. Each test set consisted of 9 to 12 firings. The test sets included firing the original nozzle, nozzle 1, and nozzle 2 at 30, 40, and 45 psia plenum pressure and nozzle 3 at 30 psia plenum pressure. Due to thruster malfunctions, testing for nozzle 3 was not conducted at 40 and 45 psia plenum pressure. The original nozzle is a bell nozzle with a 266 expansion ratio and a short length that does not follow the nominal two dimensional MOC. Nozzle 1, 2, and 3 are 15-degree conical nozzles with a 55, 266, and 22 expansion ratio, respectively.

Objective 1 was partially satisfied. The three additional nozzles were designed as 15 degrees conical nozzles based on previous research indicating that bell nozzles were contraindicated at low Reynolds numbers, and were successfully manufactured at the AFIT machine shop. This objective was only partially satisfied due to mass measurement error and unreliable data sets for the original nozzle, therefore, a conclusion toward the new designs performance is not certain. Even though there was strange behavior in the original nozzle due to flow separation, impulse bit data showed an improvement in impulse bit performance using the new nozzle designs at the 45 psia plenum pressure. Because data from the original nozzle is not reliable, a conclusion of whether impulse bit performance has been improved at 30 and 40 psia cannot be made. However, overall, the maximum nozzle 1 and 2 impulse bits are higher than the maximum original nozzle impulse bit. For specific impulse, there is a larger error bar due to the mass per fire uncertainty. The original nozzle and nozzle 1 both had similar performances in specific impulse.

Objective 2 was also partially satisfied because hardware malfunctions prevented measurement of performance with nozzle 3 at 40 and 45 psia plenum pressure. The rest of the experiments were successfully measured using a torsional balance thrust stand.

Objective 3 was satisfied. Experimental data for thrust coefficient were calculated

and shown in terms of expansion ratio and plenum pressure. The results showed low plenum pressure performance for different expansion ratios were similar because viscous effects dominate. At 40 psia, the results showed a higher performance with the smaller expansion ratio compared to the higher expansion ratio because the increase in area ratio was not enough to overcome the additional viscous effects caused by the increased surface area. At 45 psia, expansion ratio had less affects in performance as well because the system was reaching toward the maximum value on the performance curve. The relationship between expansion ratio and performance began to level off at the high pressure.

Objective 4 was also satisfied. Data was compared and analyzed in chapter 4. Specific impulse and thrust coefficient data were compared to the expected data. The expected data started off with the ideal CEA data. Then, 10 to 20% drop due to viscous effects based on Spisz *et al.* data [26] and 30 to 40% drop from steady state to pulse operation based on historical data were deducted from the ideal CEA data. The percentage loss between the experimental value and the expected value showed there was a greater loss at the lower pressure. For the higher pressure, loss percentage were similar between 40 and 45 psia. In addition, different expansion ratios also had a similar loss between the expected and measured value. Between the ideal data and the measured data, results showed an increase in loss percentage with increasing expansion ratio. At 40 and 45 psia, losses were also similar at each expansion ratio.

Objective 5 was satisfied. High speed images of each nozzle were successfully captured. High speed images of the three nozzle designs have shown an improvement in exhaust plume flow attachment compared to the original nozzle high speed images based on the exhaust plume angles. The exhaust angles were around 14-18-degree, which is closer to the 15-degree conical nozzle contour. The exit flow was more aligned with the new nozzle contour. This showed redesigning the nozzle using a 15-degree

conical nozzle can improve the flow separation problems and also improve nozzle efficiency.

5.2 Recommendation and Future work

The HYDROS^{TM} thruster is a 1U chemical pulsed thruster. This thruster operates in low Reynolds number and low mass flow rate conditions. It also has incomplete combustion, and non-steady state flow. Previous research conducted on low thrust and low Reynolds number thrusters were for steady state operation. With this research, knowledge in behavior and performance for a chemical pulse thruster was gained through comparing with the research from Spisz *et al.*

The original nozzle is not recommended for this thruster because experimental data and high speed images suggested this nozzle has early flow separation. It is not recommended to use a system because flow separation reduces nozzle efficiency. Nozzle 2 with a high expansion ratio of 266 and a length that extended out of the 1U configuration is also not recommended. The experimental result showed no benefit with the added length. Nozzle 1 and Nozzle 3 showed the best performance behavior out of the four nozzles. With similar behavior, nozzle 3 would be recommended over nozzle 1 because with the smaller expansion ratio, using nozzle 3 would reduce the weight and size of the 1U thruster. Reduced size and mass is beneficial for a volume and mass constrained CubeSat. By switching from a 55 expansion ratio to a 22 expansion ratio nozzle, the reduced length could increase the fuel tank by 64%.

5.2.1 Torsional Balance Thrust Stand.

The torsional balance thrust stand was designed and built for the HYDROS^{TM} thruster by Tethers Unlimited, Inc. Thrust stand selection for this thruster was difficult due to the short pulse condition. The thrust stand must be able to capture

the natural frequency of the response, as well as treat the thruster response as an impulse. The thrust stand for this research was a new design and it requires further improvements. This research was not able to find a consistent calibration for this thrust stand. Further investigation is required to determine why the thrust stand behavior is inconsistent. A new calibration method might be necessary. In addition, it was difficult to see if the swinging arm was absolutely parallel to the linear displacement sensor. An electronically controlled level adjuster and LDS adjuster should be added to the thrust stand to allow adjustments during vacuum testing.

5.2.2 The water electrolysis thruster.

The nozzle designs did not significantly improve the thrust coefficient or the specific impulse of the thruster as mentioned above in objective 1. A better weight scale is needed to reduce mass measurement error. Using the new nozzle design is recommended because it reduces flow separation. However, it did not change the range of specific impulse. Due to the pulsed nature of this thruster, this system might not follow a traditional method of nozzle design. A set of rules in nozzle design might not exist for a low thrust, low Reynolds number, and incomplete combustion pulsed chemical thruster. Recommendations would be to continue testing with different nozzle designs to find one that could improve the specific impulse and thrust coefficient of the system. In order to make a significant improvement in performance for this system, only changing the nozzle is not enough. There exists a limit on how much the nozzle could improve the system. Apart from nozzle designs, it is possible to redesign the thruster chamber length to accommodate the residence time and chemical time to improve combustion efficiency. This could help with the incomplete combustion problem. Lastly, the size of the H_2 and O_2 tank could also be increased to produce a longer pulse. However, due to CubeSats sizing constraints, trade offs are required in

order to improve system performance. Increasing pulse time and increasing system performance might require the thruster to extend out of its 1U configuration.

Appendix A. Impulse Bit Data

This appendix displayed the raw impulse bit data in voltage displacement prior using the calibration conversion number. These data are the amplitude of the thrust stand impulse response. Table 14 is for the original nozzle separated by different plenum pressures. Table 10 is for nozzle 1, Table 11 is for nozzle 2, and Table 12 is for nozzle 3.

Table 9. Original Nozzle Raw Data (V)

	30 Psia	40 Psia	45 Psia
1	0.161	0.386	0.287
2	0.179	0.330	0.368
3	0.164	0.336	0.342
4	0.178	0.262	0.266
5	0.183	0.287	0.257
6	0.176	0.286	0.271
7	0.169	0.285	0.266
8	0.190	0.304	0.276
9	0.166	0.284	0.269
10	0.190	0.288	0.277
11	0.178	0.293	0.271
12	0.178	0.292	0.262
13			0.284
14			0.273
15			0.272

Table 10. Nozzle 1 Raw Data (V)

	30 Psia	40 Psia	45 Psia
1	0.237	0.316	0.379
2	0.143	0.297	0.340
3	0.165	0.268	0.296
4	0.144	0.288	0.321
5	0.161	0.281	0.309
6	0.175	0.317	0.321
7	0.158	0.274	0.311
8	0.153	0.269	0.297
9	0.161	0.272	0.307
10	0.185	0.267	0.327
11	0.166	0.288	0.326
12	0.183	0.293	0.328

Table 11. Nozzle 2 Raw Data (V)

	30 Psia	40 Psia	45 Psia
1	0.181	0.241	0.327
2	0.167	0.246	0.294
3	0.168	0.242	0.319
4	0.157	0.213	0.280
5	0.195	0.268	0.346
6	0.163	0.229	0.308
7	0.172	0.228	0.341
8	0.162		0.295
9	0.178		0.277
10			0.310
11			0.316
12			0.312
13			0.299

Table 12. Nozzle 3 Raw Data (V)

	30 Psia
1	0.183
2	0.216
3	0.179
4	0.154
5	0.255
6	0.261
7	0.169
8	0.159
9	0.168
10	0.168
11	0.165
12	0.162
13	0.180

Appendix B. Specific Impulse and Thrust Coefficient Data

Table 14 displayed the I_{sp} and C_F data. Column 2 and Column 4 are the higher and lower I_{sp} values from error propagation. Column 5 and Column 7 are the higher and lower C_F values from error propagation.

Table 13. I_{sp} data for the four nozzles.

Pressure (psia)	(-)	I_{sp}(sec)	(+)	(-)	C_F	(+)
Original Nozzle						
30	60.66	78.69	96.72	0.28	0.37	0.45
40	124.55	186.99	249.43	0.58	0.87	1.16
45	106.36	149.19	192.02	0.49	0.69	0.89
Nozzle 1						
30	58.08	75.68	93.28	0.27	0.35	0.44
40	120.39	180.76	241.13	0.56	0.84	1.12
45	121.16	169.88	218.59	0.56	0.79	1.02
Nozzle 2						
30	59.13	76.77	94.40	0.28	0.36	0.44
40	100.46	150.95	201.43	0.47	0.70	0.94
45	116.63	163.42	210.21	0.54	0.76	0.98
Nozzle 3						
30	63.68	83.19	102.71	0.30	0.39	0.48

Appendix C. Mass Per Fire Data

Table 14 displayed the mass data per each test set and the average mass per each pressure.

Table 14. Mass data for each test set.

30 psia	number of firing	Mass(kg)	error (kg)
Original	12	0.0006	0.0001
Nozzle 1	12	0.00045	0.0001
Nozzle 2	11	0.0003	0.0001
Nozzle 3	13	0.0004	0.0001
Total	48	0.00175	0.0004
Average Mass per pressure case		3.645E-5	8.33E-6
40 psia	number of firing	Mass(kg)	error (kg)
Original	13	0.00035	0.0001
Nozzle 1	15	0.00035	0.0001
Nozzle 2	7	0.0002	0.0001
Total	35	0.0009	0.0003
Average Mass per pressure case		2.57E-5	8.57E-6
45 psia	number of firing	Mass(kg)	error (kg)
Original	15	0.00055	0.0001
Nozzle 1	12	0.00035	0.0001
Nozzle 2	7	0.00015	0.0001
Total	34	0.00105	0.0003
Average Mass per pressure case		3.095E-5	8.82E-6

Bibliography

1. Bruno, C. "Chemical Microthrusters: Effects of Scaling on Combustion". *37th AIAA Joint Propulsion Conference*. 8-11 July, 2001, Salt Lake CIty, Utah, 2001.

2. Collins, David, Carl Kukkonen, and Samuel Venneri. "Miniature, Low-Cost, Highly Autonomous Spacecraft A Focus for the New Millennium". *IAF Paper 95-U.2.06*, (Oslo, Norway).

3. Glassman, Irvin and Richard A. Yetter. *Combustion*. Elsevier Inc., 4th edition, 2008.

4. Grisnik, Stanley P and Tamara A Smith. "Experimental Study of Low Reynolds Number Nozzles". *19th AIAA/DGLR/JSASS International Electric Propulsion Conference*, (AIAA-87-0992), 1987.

5. Hopkins, D. F. and D. E. Hill. "Effect of Small Radius of Curvature on Transonic Flow in Axisymmetric Nozzles". *AIAA Journal*, 4(8):1337–1343, 1966. ISSN 0001-1452.

6. Huang, David and Dieter Huzel. *Modern Engineering for Design of Liquid-Propellant Rocket Engines*. AIAA, vol 147 edition, 1992.

7. Humble, Ronald W., Gary N. Henry, and Wiley J. Larson. *Space Propulsion Analysis and Design*. The McGraw-Hill Companies Inc, vol 147 edition, 1995.

8. Jones, Ross. "Small Spacecraft Activities at JPL". *Jet Propulsion Laboratory, California Institute of Technology*, 1991.

9. Ketsdever, Andrew D. "Systems Considerations and Design Options for Microspacecraft Propulsion Systems". *Technology*, (June), 1999.

10. Koizumi, H., K. Komurasaki, and Y. Arakawa. "Development of thrust stand for low impulse measurement from microthrusters". *Review of Scientific Instruments*, (Vol 75, No. 10), October, 2004.

11. Kuluva, N. M. and G. A. Hosack. "Supersonic nozzle discharge coefficients at low Reynolds numbers". *AIAA Journal*, 9(9):1876–1879, 1971. ISSN 0001-1452.

12. Lee, Simon, Amy Hutputanasin, Armen Toorian, Wenschel Lan, and Riki Munakata. *Cubesat design specification*. Technical report, California Polytechnic State University.

13. Lewis, Bernard and Guenther Von Elbe. "Combustion, Flames and Explosions of Gases". chapter 2. Academic Press, Inc., 3rd edition, 1987.

14. Liu, Kan, Colin Bunker, John Alredge, Dylan Stelzer, Andrew Wang, David Liu, and Carl Hartsfield. "HYDROS Thruster Component Testing in Atmospheric and Simulated Space Environment", 2014.

15. Liu, Y., D. Liu, and C. Hartsfield. "Performance Testing of Various Nozzle Designs for Water Electrolysis Thruster". *AIAA AIAA Science and Technology Forum and Exposition*, January, 2016.

16. McElroy, James F., Fred Mitlitsky, Andrew H. Weisberg, Preston H. Carter II, Blake Myers, and Brain D. Reed. "Electrolysis propulsion for spacecraft applications". *33rd AIAA/ASME/SAE/ASEE Joint Propulsion Conference and Exhibit*, AIAA–1997–2948.

17. Mueller, Juergen. "Thruster Options for Microspacecraft: A Review and Evaluation of State-of-the-Art and emerging technologies". *Micropropulsion for Small Spacecraft*, 187:45–137.

18. Murch, C.K., J Broadwell, A.H Silver, and T.J. Marcisz. "Low-thrust nozzle performance". *AIAA 6th Aerospace Sciences Meeting*. 1968.

19. NASA. *Cosmic Journeys, Structure &Evolution of the Universe Roadmap 2003-2023*. Technical report.

20. Ostlund, J. and B. Muhammad-Klingmann. "Supersonic Flow Separation with Application to Rocket Engine Nozzles". *Applied Mechanics Reviews*, 58(3):143, 2005. ISSN 00036900.

21. Pancotti, Anthony P., Matthew Gilpin, and Martin S. Hilario. "Comparision of electrostatic fins with piezoelectric impact hammer techniques to extend impulse calibration range of a torsional thrust stand". *Review of Scientific Instruments 83*, (035109), 2012.

22. Polk, Anthony, James E.and Pancotti, Thomas Haag, Scott King, Mitchell Walker, Joseph Blakely, and John Ziemer. "Recommended Practices in Thrust Measurements". *33rd International Electric Propulsion Conference*, (IEPC-2013-440), 2013.

23. Rao, G.V R. "Exhaust Nozzle Contour for Optimum Thrust". *Journal of Jet Propulsion*, 28(6):377–382, 1958.

24. Rosenberg, S. and L. Schoenman. "A New Generation of High Performance Engines For Spacecraft Propulsion". *AIAA 27th Joint Propulsion Conference*, (AIAA 91-2039).

25. Rothe, D. E. "Electron-beam studies of viscous flow in supersonic nozzles". *AIAA 3rd Fluid and Plasma Dynamics Conference*, AIAA 70-81, 1971. ISSN 0001-1452.

26. Spisz, Ernie W., Paul F Brinich, and John R. Jack. "Thrust Coefficients of Low-Thrust Nozzles". *NASA Technical Note D-3056*, 1965.

27. Stechman, R.C. and J.G. Campbell. *Water Electrolysis Satellite Propulsion System.* Technical Report AFRPL-TR-72-132, Marquardt Company.

28. Sutton, George P. and Oscar Bibkarz. *Rocket Propulsion Elements.* John Wiley &Sons, Inc, Hoboken, New Jersey, 8th edition, 2010.

29. Trigg, L.J. "A Generation of Hydrazine Loaders". *AIAA/SAE 11th Propulsion Conference*, (AIAA 75-1326):1–2.

30. Turns, Stephen R. *An Introduce to Combustion Concepts and Applications.* 2010.

31. Wertz, James R. and Wiley J. Larson. *Space Mission Analysis and Design.* Microcosm Press, Hawthorne, CA, 3rd edition, 2010.

32. Whalen, Margaret V. "Low Reynolds Number Nozzle Flow Study". (July 1987).

33. Wichmann, Horst, Mark Firzsimmons, and Kaiser Marquardt. "Miniature High Performance Delta V Engine". *AIAA 29th Joint Propulsion Conference and Exhibit*, (AIAA 93-2582).

34. Wrobel, Jonathan S., Robert P. Hoyt, Jeffery T. Slostad, Nathan D. Storrs, Jesse I. Cushing, Todd J. Moser, Jory L. St.Luise, and Gregory J. Jimmerson. "PowerCube - Enhanced power, propulsion, and pointing to enable agile, high -performance cubesat missions". *AIAA SPACE Conference and Exposition 2012*, (September):1–11, 2012.

35. Zeledon, Rodrigo A. and Mason A. Peck. "Electrolysis propulsion for cubesat-scale spacecraft". *AIAA SPACE Conference and Exposition 2011.*

36. Zeledon, Rodrigo A. and Mason A. Peck. "Performance Testing of a CubeSat-scale Electrolysis Propulsion System". *AIAA Guidance, Navigation, and Control Conference.*

REPORT DOCUMENTATION PAGE

Form Approved
OMB No. 0704–0188

1. REPORT DATE *(DD–MM–YYYY)*	2. REPORT TYPE	3. DATES COVERED *(From — To)*
24–03–2016	Master's Thesis	Sept 2014 — Mar 2016

4. TITLE AND SUBTITLE

Performance Testing of Various Nozzle Design for Water Electrolysis Thruster

5a. CONTRACT NUMBER

5b. GRANT NUMBER

5c. PROGRAM ELEMENT NUMBER

6. AUTHOR(S)

Yuen Jing Monica Liu, 2d Lt

5d. PROJECT NUMBER

5e. TASK NUMBER

5f. WORK UNIT NUMBER

7. PERFORMING ORGANIZATION NAME(S) AND ADDRESS(ES)

Air Force Institute of Technology
Graduate School of Engineering and Management (AFIT/EN)
2950 Hobson Way
WPAFB OH 45433-7765

8. PERFORMING ORGANIZATION REPORT NUMBER

AFIT-ENY-MS-16-M-225

9. SPONSORING / MONITORING AGENCY NAME(S) AND ADDRESS(ES)

N/A

10. SPONSOR/MONITOR'S ACRONYM(S)

AFRL/RV

11. SPONSOR/MONITOR'S REPORT NUMBER(S)

12. DISTRIBUTION / AVAILABILITY STATEMENT

DISTRIBUTION STATEMENT A:
APPROVED FOR PUBLIC RELEASE; DISTRIBUTION UNLIMITED.

13. SUPPLEMENTARY NOTES

14. ABSTRACT

The purpose of this research is to develop new nozzles for the HYDROS^{TM} thruster, a pulsed chemical thruster, to improve the current flight performance. This research consists of a base line test of the factory nozzle, as well as testing of three 15-degree conical nozzles with different expansion ratios. Experiments were conducted at plenum pressures 30, 40, and 45 psia to ensure the thruster is throttleable. Impulse bit data was collected through measuring the impulse response of each firing using a torsional balance thrust stand. Analysis of the thruster performance included calculations of impulse bit, specific impulse, thrust coefficient, and exhaust plume attachment. Experimental data showed that the smaller expansion ratio nozzles have a higher performance than the larger expansion ratio nozzles. This agrees with previous research from NASA that the benefit from the increase in area ratio does not overcome the increased viscous losses due to the increase in surface area for small throat areas.

15. SUBJECT TERMS

Micro-space propulsion, CubeSats propulsion, Nozzle Designs

16. SECURITY CLASSIFICATION OF:			17. LIMITATION OF ABSTRACT	18. NUMBER OF PAGES	19a. NAME OF RESPONSIBLE PERSON
a. REPORT	b. ABSTRACT	c. THIS PAGE			Dr. C. Hartsfield, AFIT/ENY
U	U	U	UU	131	19b. TELEPHONE NUMBER *(include area code)* (937) 255-3636, x4667; carl.hartsfield@afit.edu